CHEMISTRY, DETECTION, AND CONTROL OF METALS DURING SILICON PROCESSING

Trace Q. Hurd, B.S.

Dissertation Prepared for the Degree of

DOCTOR OF PHILOSOPHY

UNIVERSITY OF NORTH TEXAS

May 2005

APPROVED:

Oliver M. R. Chyan, Major Professor
Martin Schwartz, Committee Member
Michael Richmond, Committee Member
Teresa Golden, Committee Member
Allen Bowling, Committee Member
Ruthanne D. Thomas, Chair of the Department of Chemistry
Sandra L. Terrell, Dean of the Robert B. Toulouse School of Graduate Studies

Hurd, Trace Q. *Chemistry, Detection, and Control of Metals during Silicon Processing.* Doctor of Philosophy (Analytical Chemistry), May 2005, 174 pp., 22 tables, 63 figures, references, 153 titles.

This dissertation focuses on the chemistry, detection, and control of metals and metal contaminants during manufacturing of integrated circuits (ICs) on silicon wafers. Chapter 1 begins with an overview of IC manufacturing, including discussion of the common aqueous cleaning solutions, metallization processes, and analytical techniques that will be investigated in subsequent chapters. Chapter 2 covers initial investigations into the chemistry of the SC2 clean - a mixture of HCl, H_2O_2, and DI water - especially on the behavior of H_2O_2 in this solution and the impact of HCl concentration on metal removal from particle addition to silicon oxide surfaces. Chapter 3 includes a more generalized investigation of the chemistry of metal ions in solution and how they react with the silicon oxide surfaces they are brought into contact with, concluding with illumination of the fundamental chemical principles that govern their behavior. Chapter 4 shows how metal contaminants behave on silicon wafers when subjected to the high temperature ($\geq$ 800 °C) thermal cycles that are encountered in IC manufacturing. It demonstrates that knowledge of some fundamental thermodynamic properties of the metals allow accurate prediction of what will happen to a metal during these processes. Chapter 5 covers a very different but related aspect of metal contamination control, which is the effectiveness of metal diffusion barriers (e.g. Ru) in holding a metal of interest, (e.g. Cu), where it is wanted while preventing it from migrating to places where it is not wanted on the silicon wafer. Chapter 6 concludes with an overview of the general chemical principles that have been found to govern the behavior of metals during IC manufacturing processes.

ACKNOWLEDGEMENTS

A work such as this, while humble in the general context of scientific endeavor, is a significant undertaking in the context of personal achievement and does not come about without the help of others. Thanks are due to Dr. Oliver Chyan for his friendship, patient support, and guidance of this work. The contributions of my beautiful wife Tracy cannot be overstated. Her unwavering support has been absolutely essential as was her patience in reviewing and editing this manuscript for style and grammar. I thank my parents for first encouraging me to think critically and then giving me the space in which to do so. Where these gifts have led me could not have been predicted, but it is definitely far removed from the woods of Alabama.

There are many who have provided significant technical input to this project. Antonio Rotondaro's knowledge of semiconductor physics and personal friendship and encouragement have been invaluable; obrigadao, rapaz. Paul Mertens helped start me on this course and then persistently, if irritatingly, pushed me to continuously apply the scientific method. Lindsey Hall and Tom Talasek proved a Ph.D. could be done while working full time and left me no option but to do so. Allen Bowling never lost faith that this could be completed successfully and has provided irreplaceable support at all the right times.

Finally, the list of contributors, both personal and technical is lengthy and includes the following: Karine Kenis, Marcel Lux, Ingrid Cornilissen, Harald Schmidt, Chris Elsmore, Marc Heyns, Marc Meuris, and Ann Opdebeeck at IMEC; Bud Schmidt, Jackie Kemp, Charlotte Appel, Jennifer O'Brien, Marcelo Salazar, and Doug Mercer at TI.

TABLE OF CONTENTS

LIST OF TABLES

LIST OF ILLUSTRATIONS

LIST OF ABBREVIATIONS AND DEFINITIONS

BARC – Bottom anti-reflective coating. A thin organic film placed under photoresist to eliminate reflection that inteferes with patterning.

BHF – Buffered hydrofluoric acid. A mixture of HF and NH4F normally in a 1:100 ratio.

CMP – Chemical mechanical polishing. A process using particle laden slurries (silica, alumina, or ceria) and rough pads whereby wafers are polished to extreme flatness.

Cz/CZ– Silicon wafer manufactured using the Czochralski method for creating monocrystalline silicon; named after the inventor. A small, perfect crystal is dipped into the surface of a spinning bath of molten silion and as it is slowly pulled from the melt, an ingot of monocrystalline silicon is formed.

CZn – N-type CZ.

CZp – P-type CZ.

DHCl – Dilute HCl. A mixture of HCl and deionized (DI) water.

dHF – Dilute hydrofluoric acid. A mixture of HF and DI water.

DLTS – Deep level transient spectroscopy. Quantitative method for measuring energy states of impurities in silicon crystals.

DRC – Dynamic reaction cell. Specialized chamber on an ICP-MS that removes interfering ions and permits low level detection of K, Ca, and Fe.

ECD – Electrochemical deposition. Method for electroplating metals like Cu onto silicon substrates.

Fab – Wafer fabrication area. The factory where integrated circuits are manufactured.

FZ – Silion crystal generated by the float zone method of silicon crystal formation. An imperfect silion ingot is pulled through a zone of high temperature which simultaneously forms

monocrystalline silicon and allow impurities like oxygen to escape. FZ silicon is some of the most perfect manufactured but is more expensive.

FZn – N-type FZ.

FZp – P-type FZ.

GFAA – Graphite furnace atomic absorption. Sensitive method for analyzing low concentrations of metals in liquids.

GOI – Gate oxide integrity. Measure of how reliable a gate oxide will be, usually via Vbd or Qbd techniques.

HRTEM – High resolution transmission electron micrsoscope.

IC – Integrated Circuit

ICP-MS – Inductively coupled plasma mass spectroscopy. Sensitive method for analyzing low concentrations of metals in liquids.

I/O – Input/Output. The transistors that are connected to world outside of the IC.

DRAM – Dynamic random access memory. A type of IC that provides the memory for PCs.

LSE – Latex sphere equivalent. Size units that wafer surface particle detectors report results in.

L – Minority carrier diffusion length. Sensitive measure of bulk silicon quality determined by average length minority carriers can travel before recombining.

MCLT – Minority carrier lifetime. Sensitive measure of bulk silicon quality determined by average length of time it takes minority carriers to recombine.

MOS – Metal oxide semiconductor. Type of IC that uses a silicon oxide capacitor sandwiched between two conducting films (typically highly doped polysilicon and moncrystalline silicon) as the switch to turn transistors on and off.

NMOS – MOS that is n-type doped.

N-Type – Doped with Group V atoms, e.g P to increase conductivity by addition of electrons to the silicon crystal.

OCP – Open circuit potential. Potential at which there is no current in a circuit.

P-Type – Doped with Group III atoms, e.g. B to increase conductivity by addition of empty orbitals (holes) to the silicon crystal.

PMOS – MOS that is p-type doped.

PVD – Physical vapor deposition. Method for depositing thin films using either thermal evaporation or physical sputtering of a metal source onto a substrate.

μPCD – Microwave photoconductance decay. Method used do measure MCLT.

Q_{bd} – Measure of GOI. Quantity of charge that can pass through a gate oxide before it breaks down.

SC – Semiconductor

SC1 – Standard Clean 1. Mixture of NH_4OH, H_2O_2, and H_2O used to clean particles from wafers.

SC2 – Standard Clean 2. Mixture of HCl, H_2O_2, and H_2O used to clean metals from wafers.

SEM – Scanning electron microscope.

SIMS – Secondary ion mass spectroscopy. Sputtering technique to measure surface an bulk metal contamination concentrations.

SPM – Sulfuric peroxide mixture. Also known as piranha, a mixture of H_2SO_4 and H_2O_2 that is used at high temperature to remove organics and metals from wafers.

SPV – Surface photovoltage. Method used to measure L.

TEM – Transmission electron microscope.

ToF-SIMS – Time of flight secondary ion mass spectroscopy. Extremely surface sensitive SIMS technique.

TXRF – Total reflectance x-ray fluorescence. Sensitive technique for measuring metals on silicon wafer surfaces via the fluorescence generated by exposure to glancing angle X-rays.

ULSI – Ultra large scale integration. Term used to describe integrated circuit technology using devices with features smaller than one micron in width.

VPD-DC – Vapor Phase Decompostion Droplet Collection. Method for pre-concetrating metals on a wafer surface so that they can be measured with greater sensitivity by TXRF, ICP-MS, or GFAA.

VPD-DC-GFAA – See VPD-DC and GFAA.

VPD-DC-ICP-MS – See VPD-DC and ICP-MS.

VPD-DC-TXRF – See VPD-DC and TXRF.

V_{bd} – Voltage breakdown. Measure of GOI based on ramping voltage across a gate oxide and recording voltage at which it breaks down.

LIST OF SYMBOLS

1. <100> crystal orientation
2. A doping density dependent coefficient
3. β_x (M^{-x}) overall stability constant (x > 1)
4. σ_f (s^{-1}) surface recombination velocity of an illuminated surface
5. D (m^2s^{-1}) diffusivity
6. D_n (m^2s^{-1}) electron diffusion coefficient
7. E_{kin} (eV) kinetic energy
8. E (eV) E_{kin}
9. ΔE (eV) energy difference
10. f_i cumulative distribution value for the ith point in a Weibull distribution
11. Fe_{bulk} (m^{-3}) concentration of Fe in bulk Si
12. Fe_i interstitial Fe
13. Φ (s^{-1}) incident photon flux
14. Φ_{eff} (s^{-1}) effective incident photo flux
15. I (M) ionic strength
16. K_x (M^{-x}) stepwise stability constant (x > 0)
17. K_{hy} (M^y) stepwise hydrolysis stability constant (y > 0)
18. K_{sy} (M^{y-1}) stepwise surface stability constant (y > 0)
19. L (m) diffusion length
20. L^2_{aft} square of L after FeB pair dissociation
21. L^2_{bef} square of L before FeB pair dissociation
22. M (mol/l) molarity

23. m (kg) mass

24. Δm (kg) mass difference

25. n (mol) amount of H_2O_2

26. n_g (mol) amount of O_2

27. ν_{th} (ms^{-1}) thermal velocity of carriers

28. N_t (m^{-3}) concentration of recombination centers

29. p (T) pressure

30. p_g (T) overpressure of O_2

31. Δp_g (T) fixed overpressure of O_2

32. R surface reflectivity

33. r_n (s^{-1}) normalized decomposition rate

34. r ($\mu\Omega cm$) bulk resistivity

35. σ_h (m^{-2}) hole capture cross section

36. σ_e (m^{-2}) electron capture cross section

37. t (s) time

38. Δt (s) change in time

39. T (K) temperature

40. $\tau_{\mu PCD}$ (s^{-1}) MCLT measured by tmPCD

41. τ_{SPV} (s^{-1}) MCLT measured by SPV

42. Δt_p (s) ToF-SIMS primary ion pulse width

43. Δt_d (S) Tof-SIMS detector time resolution

44. τ (s) lifetime

45. τ_{eff} (s) measured MCLT

46. τ_{bulk} (s) lifetime of minority carriers in bulk silicon

47. τ_{surf} (s) lifetime of minority carriers at silicon surface

48. $\tau_{bulk,h}$ lifetime of holes in bulk silicon

49. $\tau_{bulk,e}$ lifetime of electrons in bulk silicon

50. t_0 starting time

51. θ ($atcm^{-2}s^{-1}$) evaporation rate

52. t_{impact} (s) time of impact of an ion into the detector (ToF-SIMS)

53. V (v) voltage

54. ΔV (V) surface photovoltage

55. V_g (m^{-3}) fixed gas volume

CHAPTER 1

INTRODUCTION

The semiconductor (SC) industry is today a global industry that generates more than $200 billion annually. It manufactures the lowest entropy products ever created by humankind. State of the art integrated circuits (ICs) have features on them that are less than 50 nm in width with new devices being readied for manufacturing in the next two years that will shrink the minimum feature size to 30 nm or less.[1] With new state of the art factories (wafer fabrication facilities, or "fabs") costing upwards of $3 billion to build, it is necessary for production yields to be very high in order to justify the huge financial investment required. In order to achieve these yields, the manufacturing process must maintain and control cleanliness on the silicon substrates (wafers) that the ICs are built upon down to atomic levels. Contaminants that must be tightly controlled include metals, particulate matter (whether organic or inorganic), and organic molecules. In order to manage contaminants cost effectively, it is important that the chemical principles controlling these contaminants be understood so that processes can be rationally designed to deal with them.

This dissertation focuses on the chemistry, detection, and control of metals and metal contaminants during manufacturing of ICs on silicon wafers. Chapter 1 begins with an overview of IC manufacturing, including discussion of the common aqueous cleaning solutions, metallization processes, and analytical techniques investigated in subsequent chapters. Chapter 2 covers initial investigations into the chemistry of the SC2 clean - a mixture of HCl, H_2O_2, and DI water - especially on the behavior of H_2O_2 in this solution and the impact of HCl concentration on metal removal from particle addition to silicon oxide surfaces. Chapter 3 includes a more generalized investigation of the chemistry of metal ions in solution and how they react with

silicon oxide surfaces they are brought into contact with, concluding with illumination of the fundamental chemical principles that govern their behavior. Chapter 4 then shows how metal contaminants behave on silicon wafers when subjected to the high temperature (≥800 °C) thermal cycles that are encountered in IC manufacturing and demonstrates that knowledge of some fundamental thermodynamic properties of the metals allow accurate prediction of what will happen to a metal during these processes. Chapter 5 will then cover a very different but related aspect of metal contamination control, which is the effectiveness of metal diffusion barriers like Ru in holding a metal of interest like Cu where it is wanted while preventing it from migrating to places where it is not wanted on the silicon wafer. Chapter 6 will conclude with an overview of the general chemical principles that have been found to govern the behavior of metals during wafer cleaning and thermal annealing processes.

1.1 The Manufacturing Process

1.1.1 Front End of Line (FEOL)

The FEOL is defined for the purposes of this thesis as the portion of the manufacturing process carried out prior to metal being intentionally put on the wafer and during which the transistors are defined and created. In this part of the fabrication flow, all metal contamination is considered undesirable, primarily due to two deleterious effects: 1) degradation of gate oxide quality leading to early device failure[2-6] and 2) increased electrical leakage in the silicon substrate.[7-12] Figure 1.1 shows a schematic cross section of a transistor built on silicon substrate while Figure 1.2 shows a cross sectional transmission electron microscope (TEM) image of an actual transistor showing the scale of the device.

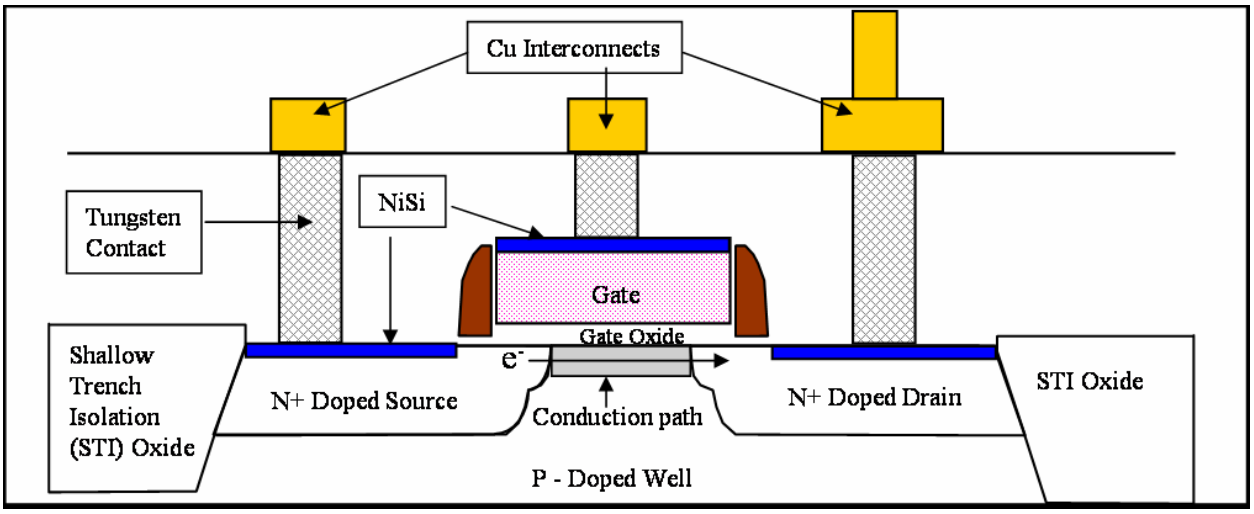

Figure 1.1: Schematic of an NMOS transistor cross section.

1.1.1.1 Silicon Doping

In order to modulate the electrical properties of silicon during FEOL IC device manufacturing, electron rich or electron poor dopant atoms are incorporated into the silicon crystal to create localized areas of higher electrical conductivity. When Group III atoms like B (a positive or p-type dopant) are used to substitute for Group IV Si atoms in the crystal lattice, they create areas where the lattice is missing an electron, resulting in a “hole”. These “holes” provide a lower energy pathway for electrical current to pass through the Si by inserting an additional energy level just above (0.03eV - 0.06eV) the valence band. Electrons can use this energy level to move from one part of the crystal to another without having to jump all the way up to the conduction band of the Si (1.1eV above the valence band). In p-type silicon, holes are considered to be the majority charge carrier and electrons are the minority charge carriers. This designation is given solely based on their relative concentrations in the silicon lattice. Alternatively, when Group V atoms like P (a negative or n-type dopant) are used to substitute for Group IV Si atoms in the crystal lattice, they create areas where the lattice has an “extra” electron. These extra

electrons provide a lower energy pathway for electrical current to pass through the Si by inserting electrons at an energy level just below (0.03eV – 0.06eV) the conduction band. These electrons can more easily move into the conduction band and move from one part of the crystal to another. In the case of n-type silicon, electrons are the majority carrier and holes are the minority carriers. This more easily illustrated by referencing Figure 1.1 which shows a cross section of a typical NMOS transistor. Two highly n-doped areas, designated as source and drain in reference to where electrons will flow from and to respectively, are separated by a less conductive, lightly p-doped region. When the gate is placed under a negative bias, the gate oxide

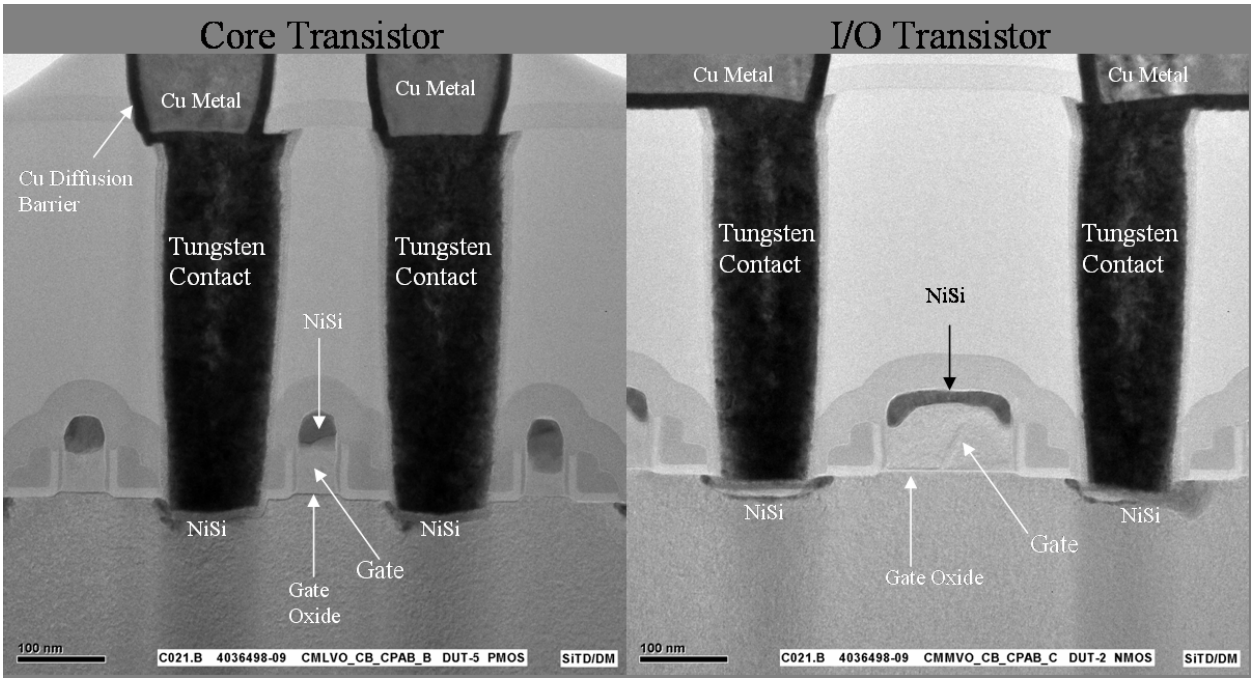

Figure 1.2: Cross sectional TEM image of the 65nm high performance technology node core and input/output (I/O) transistors. Core is much smaller and operates at ~1/3 the voltage of the I/O transistor. Contact to gate is not seen as it is away from the viewer in the z direction. Note that thin line under the gate is the gate oxide!

is capacitively charged by movement of positively charged holes to the region under the gate oxide. When enough holes have been gathered to this region, a conductive path is created, resulting in electron flow from the source to the drain. When this occurs, the transistor is said to have been turned "on". When the bias on the gate is removed, electron flow stops and the transistor is said to have been turned "off".

Charge movement in crystal silicon can be discussed in terms of the movement of either electrons (negative charge carriers) or holes (positive charge carriers). In fact, when any charge movement occurs in Si (or any semiconductor for that matter) movement of electrons and holes must occur simultaneously, in opposite directions, for global charge neutrality to be maintained. It is customary to speak of majority and minority charge carriers when discussing charge separation and movement in bulk silicon. In a region that is p-type doped, the majority carriers will be holes and minority carriers will be electrons, while in n-type doped regions, the majority carriers will be electrons and the minority carriers will be holes. These distinctions will be of importance when discussing both bulk Si analytical techniques later in this chapter as well as results obtained in Chapter 4.

1.1.1.2 Gate Oxide Function and Impact of Alkali, Alkaline Earth, and Transition Metals

The gate oxide is one of the most contamination sensitive structures that is created in device manufacturing. In state of the art devices, the thickness of this oxide can be anywhere from 10 nm to 1 nm. The purpose of this oxide is to act as a capacitor which turns the transistor on and off. When a voltage is applied to the oxide via the conductive gate above it, capacitive charging creates a charge rich layer in the silicon crystal directly below the gate. Depending on the dopant type in the Si under the gate oxide and the polarity of the electrical bias placed on the gate, either electrons or holes will gather in the silicon underneath the oxide. This creates a

conductive region which connects the source (region of higher electrical bias) to the drain (region of lower electrical bias) resulting in current flow from source to drain.[13] When considering that devices operate in the GHz range, it is easily seen that the gate oxide must be of extremely high quality to survive being electrically biased billions of times per second for up to 10 years at temperatures of 150 °C or more (minimum reliability target for semiconductor devices).

Degradation of gate oxide quality and function is most sensitively impacted by alkali and alkaline earth metals (particularly Na and Ca due to their ubiquity). Very low levels of these, on the order of 1 x 10^{11} at/cm^2 can cause early failure of gate oxides when put under electrical bias.[2-6] When a gate oxide is put under electrical bias, Na rapidly ionizes and becomes a mobile ion which can feely move from one side of the gate oxide to the other. This has the effect of neutralizing a portion of the charge placed on the gate and changing its performance characteristics. Alkaline earth metals, e.g. Ca, incorporate into the gate oxide during growth and become part of the oxide structure. When the gate is put under bias, these metals act as point defects which can provide conducting paths for electrical current to flow across the capacitor, resulting in early break down of the oxide and failure of the transistor to function.[14-16]

Transition metals (especially Cr and heavier in the 3d series) are of concern due to their high mobility in silicon during high temperature (> 800 °C) processing and the ability of some (Fe, Cu) to insert additional energy levels in the middle of the Si bandgap. This creates lower energy paths for charge carriers to move between the conduction and valence bands, effectively acting as an uncontrolled dopant in the silicon, resulting in very short lifetimes for minority carriers in the silicon substrate. Charge leakage pathways are thus formed in the silicon substrate, making it difficult to maintain charge separations long enough for transistors, and especially

storage capacitors (as used in dynamic random access memory, DRAM), to function as required. At high enough bulk metal concentrations they can cause transistor shorting by allowing the free flow of electrons from source to drain regions even when the gate is not biased. They can also form metal silicide regions that are thicker than the gate oxide that grows around them, causing immediate shorting between gate and substrate.[16] While the same arguments apply to 4d and 5d transition metals, the relative abundance of the 3d metals in a manufacturing environment make them especially troublesome. Major exceptions to this occur in the specific instances where a particular technology requires using 4d and 5d metals in the manufacturing process itself, e.g. Pt, Ir, Pb and Zr for ferroelectric memories, Ba, Sr, Ti and Ta for Ta_2O_5 and $BaSrTiO_3$ capacitors in DRAM, Ru as a barrier metal for Cu, and Zr & Hf for alternative gate oxide materials. [17-20]

1.1.1.3 Wet Cleaning Solutions for Metal Contamination Control

In order to control metal contamination during FEOL manufacturing, various aqueous chemical blends are used to selectively remove metals from the silicon and silicon oxide surface of the wafer prior to entering high temperature processes that would cause the metals to diffuse in and damage the electrical properties of the crystal lattice. The most important of these are are:

1. SC1 (Standard Clean 1)– A mixture of 29% NH_4OH, 30% H_2O_2, and DI water. Mixes can be anywhere from 1:1:5 (the classic RCA blend) to 1:1:100.[21] NH_4OH and H_2O_2 ratios can vary as well, with 1:1 being the most widely used but with other ratios being investigated by various researchers.[22] SC1 may be used at temperatures ranging from room temperature to as much as 80 °C. Due to its alkaline nature (pH 9-11) with resultant impact on particle zeta potentials, wafer surface charge, and slow etchrate of Si and SiO_2, this mixture is generally used to remove particles and only weakly removes most metals.

2. SC2 (Stanard Clean 2) – A mixture of 37% HCl, 30% H_2O_2, and DI water. Mixes can be anywhere from 1:1:5 (the classic RCA blend) or even more dilute.[21,23] While HCl and H_2O_2 ratios are generally kept 1:1, they can vary even more widely than the NH_4OH ratio does in SC1. Given its acidic nature (pH 0-4) this solution is primarily used to remove metals while having poorer particle performance than SC1. As with SC1, it can be used at temperatures ranging from room temperature to 80 °C.
3. SPM (sulfuric peroxide mixture) or piranha (common name) – A mixture of 30% H_2O_2 with 96% H_2SO_4 in ratios from 1:4 to 1:8. Upon mixing, the solution exotherms to upwards of 110 °C and may be externally heated to up to 130 °C. This mixture is used primarily to strip organics (e.g. photoresist or etch generated polymers) but is also very effective at removing most metals due to its extremely high oxidation potential and low pH. As with SC2, it generally leaves higher than desired levels of particles on wafers which must be removed by subsequent cleans.
4. HF/BHF (hydrofluoric acid/buffered hydrofluoric acid) – This is used for removing undesired oxide films from silicon wafers. It also can be used to create extremely clean silicon surfaces. HF is normally used in a 1:100 dilution of 49% HF, dilutions of up to 1:500 are in use today as geometries shrink and oxide films decrease in thickness to <3 nm. BHF, a mixture of 40% NH_4F and 49% HF, (commonly in a 100:1 ratio) is widely used for fine oxide etching in the presence of resist. The higher pH and buffering provided by the NH_4F makes the resulting solution much more chemically compatible with photoresist.

1.1.2 Back End of Line (BEOL)

For the back end of line, defined for the purposes of this thesis as the part of the manufacturing flow where metal films are deposited and patterned on the wafer, it might seem odd to worry about metal contamination when various metals (Ti, W, Ta, Cu, Al) are being put on the wafer intentionally. For this portion of the fabrication flow, the primary concern is making sure that metals are left only where they are desired and are removed from where they are not.

When using Cu as the metal to route electrical signals from the transistors in the Si to the outside world of a cell phone or PC, the most common manufacturing approach is known as dual damascene integration (Figure 1.3). In this approach, the intermetal dielectric insulating layers are patterned and the vias that will connect one metal level with another are etched. The wafers are then cleaned, the vias are filled with a BARC (bottom anti-reflective coating), the wafers are repatterned and the trenches are etched. Filling vias with BARC serves two purposes: 1) it removes topography from the wafer surface (i.e. planarizes it) making the subsequent patterning step much better controlled, and 2) because it etches at a rate identical to the dielectric, it improves the cross sectional profile of the trench formed by the etch process. After another round of cleaning, the vias and trenches are then coated with a thin (10-20 nm thick) diffusion barrier (typically Ta or TaN today) followed by a thin (80-120 nm thick) seed layer of Cu. Next, Cu is bulk deposited using electrochemical deposition (ECD, electroplating) overfilling the vias and trenches and leaving a thick (300-500 nm) continuous layer of Cu on the wafer. This layer is then polished back to the top of the dielectric using chemical mechanical polishing (CMP) which employs a rough pad and a slurry of either silica or alumina particles in water to remove the unwanted Cu and diffusion barrier.[24] This process sequence is shown schematically in Figure

1.3, while a cross sectional scanning electron microscope (SEM) image of a nine metal level Cu integration finished product is shown in Figure 1.4

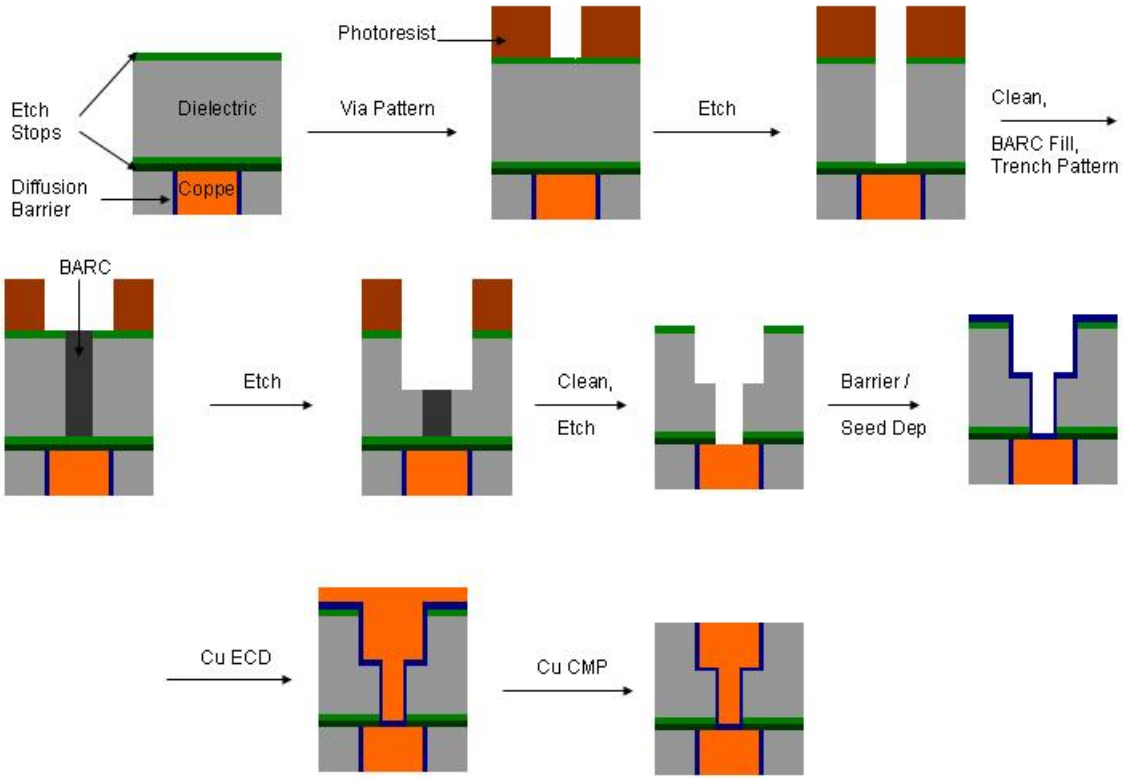

Figure 1.3: Dual damascene integration of Cu circuitry on semiconductor devices.

The final part of this dissertation explores Ru as a new Cu diffusion barrier onto which Cu can be electroplated directly, without the need for the Cu seed layer that is necessary for Ta/TaN diffusion barriers. This allows a much thinner total barrier/seed combination as no Cu seed barrier is needed, thereby enabling the ever smaller geometries demanded by the IC industry roadmap can be achieved.

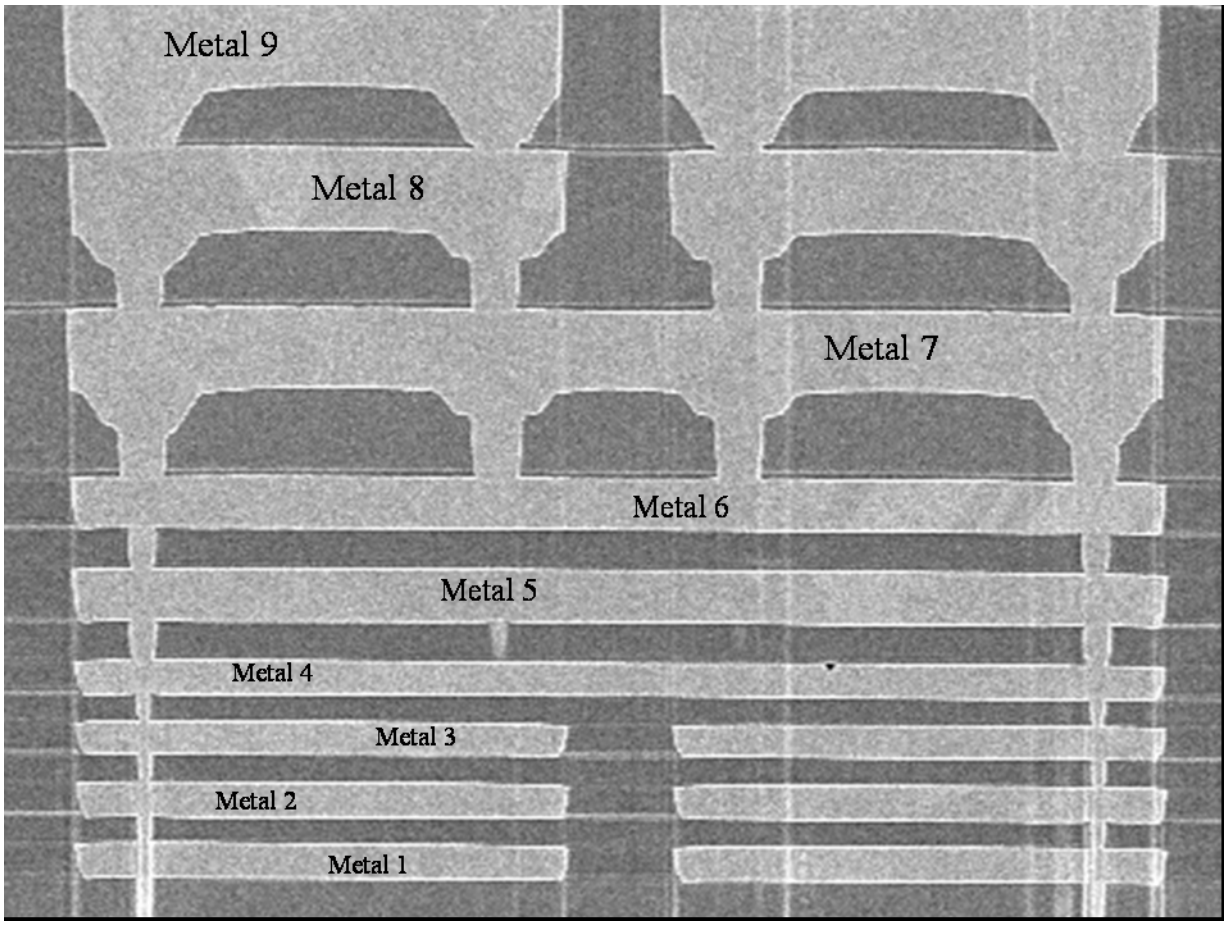

Figure 1.4: Cross section SEM of 90 nm nine evel dual damascene Cu integration. Note that the widths of the vertical vias connecting Metal 1 to Metal 4 are 90nm across. Several dozen of the transitors shown in Figure 1.2 would fit across the width of this SEM!

1.2 Surface Analysis Techniques

1.2.1 Total Reflection X-Ray Fluorescence (TXRF)

TXRF is perhaps the most routinely used surface metal analytical technique in semiconductor manufacturing. A schematic of the equipment can be seen in Figure 1.5. An x-ray

beam generated by a rotating anode is sent through a crystal monochromator and directed at a polished Si surface at an incident angle below the critical angle, 0.12 degrees. The incident beam reflects from the surface and is absorbed by a beam stop which is remote from the wafer. The incident beam excites all atoms in the irradiated area to a maximum depth of 5 to 10 nm, causing these atoms to fluoresce and emit light with characteristic energies in all directions.[25-28]

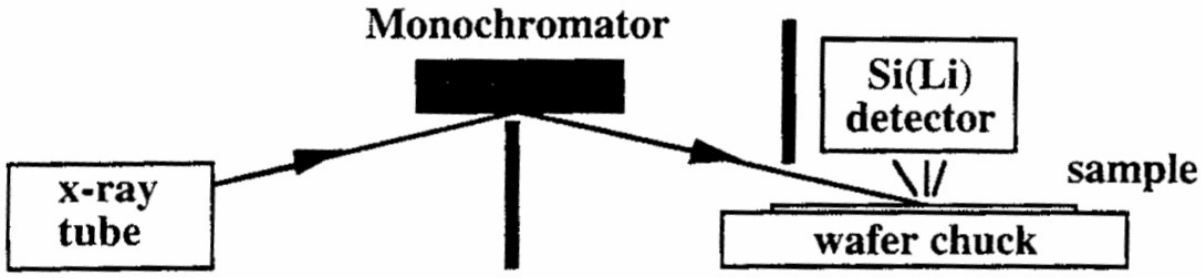

Figure 1.5: Total reflection x-ray fluorescence spectrometer instrument diagram.

An x-ray detector (generally a liquid N_2 cooled, Si(Li) solid state detector) with a window opening of ~1cm^2 is placed normal to the surface at a distance of ~500 microns and collects the fluoresced light. As the excitation x-ray beam is completely reflected, the background due to scattering is almost totally eliminated, resulting in very high sensitivity to trace amounts of contaminants on the Si surface. Integration of the collected signal is done over a user defined time period to give the desired signal to noise ratio. Usually time periods of 250 or 1000 seconds are used to achieve detection limits in the low 10^9 at/cm^2 to low 10^{10} at/cm^2 range, depending on the fluorescence intensity of a metal and its capture cross section for the exciting frequency used. X-ray lines typically used are the W L_β line for detecting elements between K and Zn, Mo K_α for detecting elements heavier than Zn, and Ag L_α for detecting elements lighter than K. Figures 1.6 and 1.7 show sample spectra created using the W L_β and Mo K_α lines for

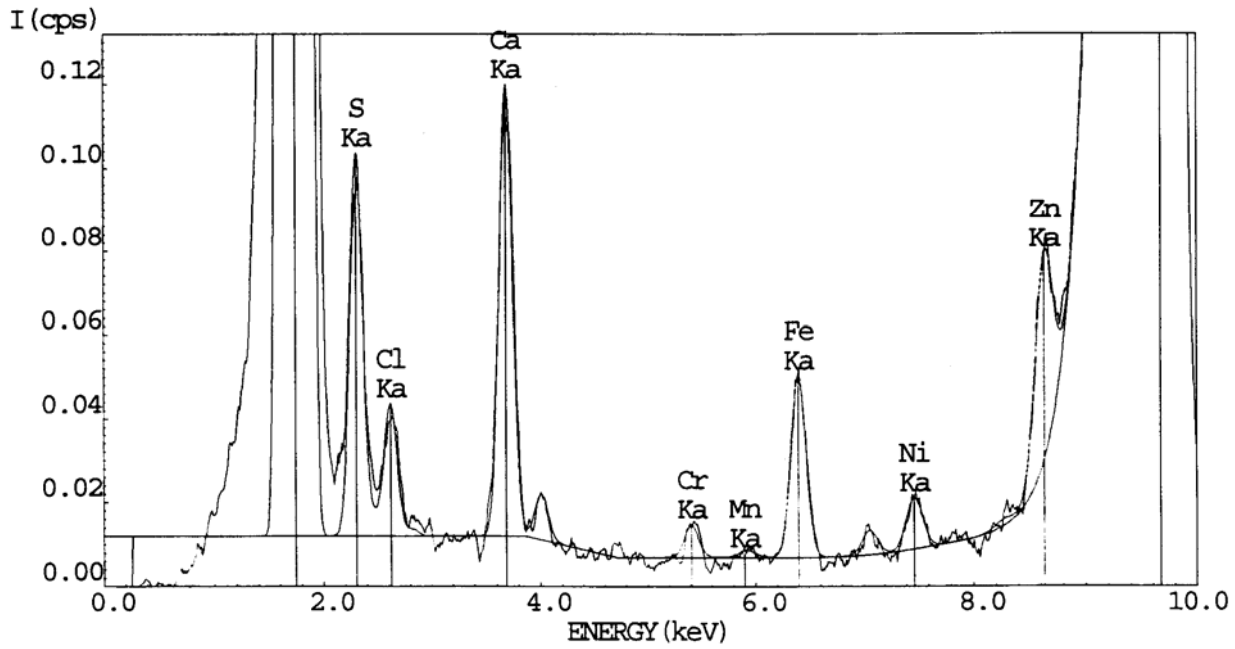

Figure 1.6: Sample TXRF spectrum with peak assignments using a W Lβ line for excitation.

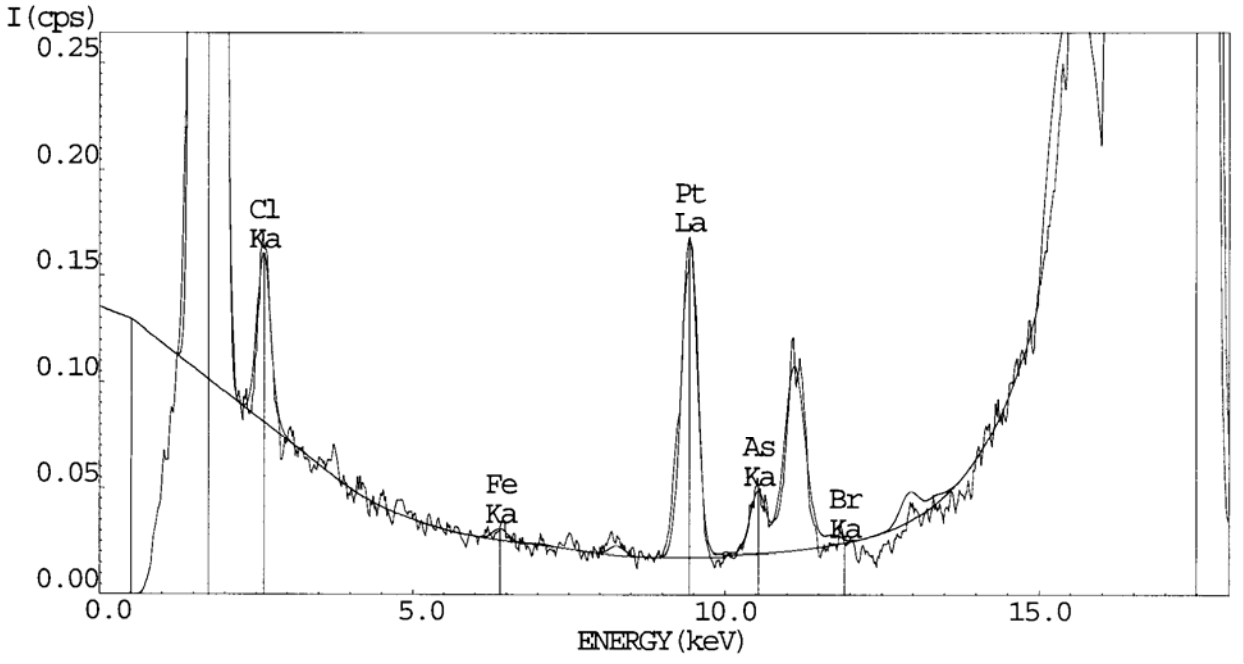

Figure 1.7: Sample TXRF spectrum with peak assignments using a Mo Kα line for excitation.

sample excitation. Detection limit improves as a function of the square root of the collection time, so it rapidly becomes time prohibitive to attempt to push detection limits by simply increasing detector time. To better accomplish this, a physical pre-concentration method, known as vapor phase decomposition – droplet collection is utilized.[29] This technique will be discussed in more detail in Section 1.2.3.

Limitations of the TXRF technique are that it requires a highly polished surface to avoid x-ray scattering which means it cannot be used on wafers with any type of structure on them or with any significant amount of roughness. Another limitation is that it has a sample area of ~1cm^2 which is determined primarily by the detector window. For a 200mm diameter silicon wafer, this means that each TXRF analysis provides information on only ~0.3% of the wafer's surface area so multiple measurements at different locations must be made to get a fair sampling of total contaminant levels and/or their spatial distribution. It also cannot measure closer than 10 mm to the edge of a wafer as excess scattering of x-rays at the edge of the wafer will rapidly push the background levels up to a point that the desired sensitivity is lost. Measurement time of 30-60 minutes per wafer, while acceptable for research purposes, can be quite long in the context of IC manufacturing.

TXRF analyses were performed using either an Atomika XSA8010 or a Technos 6010. The Atomika was used with fixed W anode operating at 50 kV, 40 mA, and an incident angle on the wafer of 0.5 mrad. The Technos was used with either a rotating W or Mo anode, depending on metal of interest, both operating at 40 kV, 40 mA, and an incident angle of 0.5 mrad. In both cases a Si(Li) scintillation counter set normal to the surface was used for detection of fluoresced x-rays.

1.2.2 Time of Flight Secondary Ion Mass Spectroscopy (ToF-SIMS)

Time of flight secondary ion mass spectroscopy (ToF-SIMS) is a powerful surface analytical technique that offers sub-monolayer sampling depth, submicron lateral resolution (~0.2 μm when using a liquid metal ion source), virtually unlimited mass range, high mass resolution, and extreme sensitivity to both atomic and molecular species. The SIMS technique is analogous to sandblasting on a molecular scale. A beam of primary ions is directed at a sample

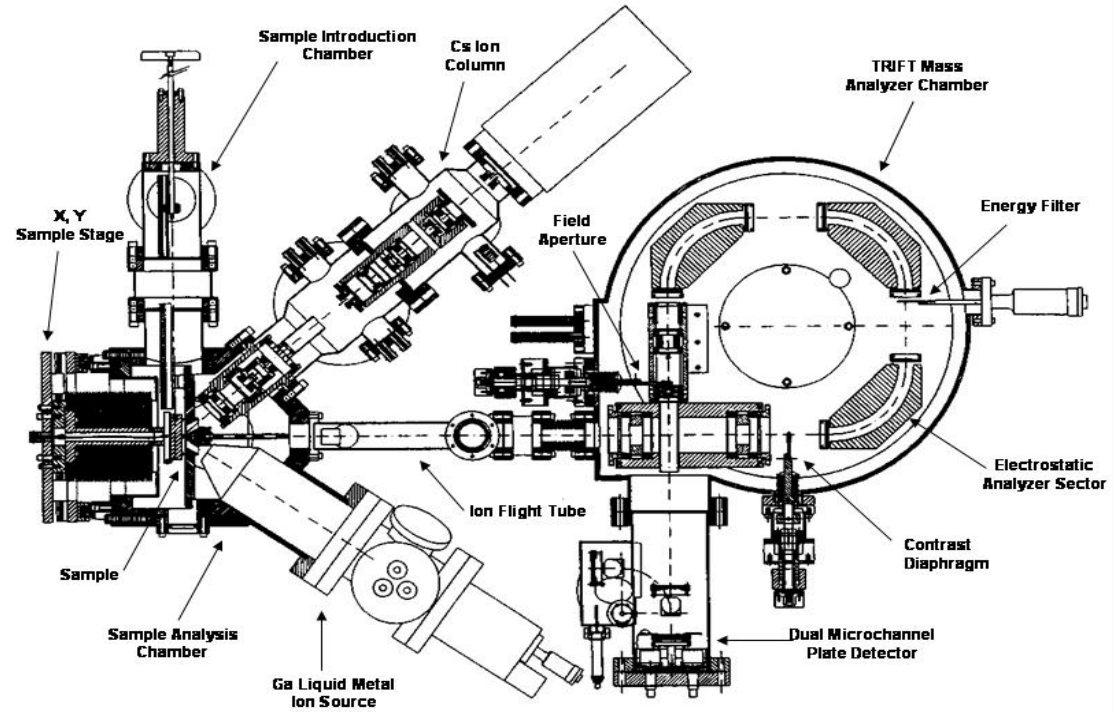

Figure 1.8: Diagram of ToF-SIMS instrument including TRIFT^{TM} mass analyzer.

surface, which is held at a bias that is generally <5 keV, causing atoms and molecules on the surface to be sputtered away from it. These secondary ions are captured by collection fields and accelerated into a mass spectrometer where they are separated by their mass/charge ratio and detected.

The ion beam will usually be composed of one of the following ions: Cs^+, O_2^+, O^-, Ar^+, or Ga^+. The choice of primary ion is made depending on several factors, including sample matrix, chemical nature of the impurity one is looking for, and spatial resolution required (i.e. beam size). The energy of the primary ion beam can be anywhere from 1-30 keV with 10-20 keV being common. The primary ion dose is generally $<5 \times 10^{12}$ ions/cm^2 for ToF-SIMS for reasons that will be explained later. At these energies and doses, the surface can be sputtered away at rates of <0.5 nm/sec to 5 nm/sec or higher.

Secondary ions that are electrostatically accelerated towards a detector by a voltage, V_0, will have a finite kinetic energy, E_{kin}, which will be directly related to their mass, i.e. $E_{kin} = eV_0 = mv^2/2$. Therefore, lighter ions will have a higher velocity and will arrive at the detector first. If the position and velocity of the ion is known at both $t = 0$, and $t = t_{impact}$ (when the ion hits the detector), it is possible to determine the mass/charge ratio of the ion.

Assuming that the surface density of a monolayer is 5×10^{14} cm^{-2} (1 nmol) then the total number of molecules present in 1 μm^2 (on the order of ion beam dimensions) will be 5×10^6 (12 amol). Compound this with the fact that ionization probabilities for surface constituents are less than 10^{-4}, it becomes clear that to be surface sensitive, a detector is required that will detect practically all ions that are generated (i.e. have a high transmission rate). This requirement is met only by time of flight detectors.

In time of flight detectors, all masses are detected more or less simultaneously ($\Delta t < 1$ nsec). This means that the detector has a high transmission rate and therefore much less sample needs to be consumed in order to get a measurable signal. This addresses the issue of only having a vanishingly small number of analyte species available for detection. It also means that the detector has a virtually unlimited mass range, from hydrogen up to molecular ions with masses in

the thousands of daltons which is very useful when the composition of the surface is not known at all.

Defining when t = 0 is achieved by pulsing the primary ion beam; pulsewidths of less than 700 ps are common. The collection optics and detector are all synchronized with the primary ion pulse so that the mass of the ions can be related to their flight time. The mass resolution (m/Δm) attainable by a time of fight detector is given by:

$$\frac{m}{\Delta m} = \frac{E}{\Delta E} + \frac{t}{2(\Delta t_p + \Delta t_d)} \qquad 1.1$$

where m = mass, E = E_{kin}, t = flight time, Δt_p = primary ion pulse duration, and Δt_d = detector time resolution.[30] Given that Δt_p is on the order of 700 ps, and Δt_d is on the order of 70 ps, with a detector drift region of ~1.5 m, giving a t = ~40 μs, the theoretical maximum resolution for a time of flight detector should be on the order of 10^5. Of course, all ions do not begin their flight from the surface with the same kinetic energy and position and so this theoretical maximum has not been achieved in practice. Differences come about due to a variety of reasons including non-uniform surface geometry, varying escape trajectories from the surface, and the duration of the pulsewidth itself.

The problem of spread in the ions' kinetic energies is dealt with by using analyzers which focus the energies of the ions electrostatically. One of the most common means of doing this are TRIFT™ triple hemispherical electrostatic analyzers, and reflectrons, both of which force higher energy ions to travel along a longer flight path, thereby compressing the energy difference between the ions, tightening the spatial (temporal) width of the ion packet.[31,32] A TRIFT™ is shown in Figure 1.8. In the TRIFT™, the secondary ions are forced to travel along a circular path, which deflects them 270 degrees away from their original path. During deflection, ions with higher energy will travel closer to the outside of the curve, traversing a greater distance and

allowing slower ions to catch up. With proper tuning, mass resolutions of 6000 at 28 daltons are routine, with resolutions up to 35000 in specific instances being reported in the literature.[32]

The high transmission rate of the time of flight detector allows the analyst to use a much smaller primary ion dose, typically <5 x 10^{12} ions/cm^2. It also allows the technique to have extremely low detection limits, generally in the range of 10^6 to 10^8 at/cm^2 for elements of interest to IC manufacturing.[33]

In summary, the combination of SIMS with time of flight detection produces an analytical technique with the following characteristics of interest to this investigation: extremely low detection limits, almost no sample preparation, sub-monolayer sensitivity, extremely accurate mass determination, very high lateral and depth resolution, and ultra low sample consumption. The only quality needed from the sample is that it be compatible with the UHV conditions (10^{-9} to 10^{-10} torr) required for the analysis. The major drawback to the technique is sample size, which at 40 um X 40 um is generally not adequate for getting statistically valid samples from a 200 mm wafer. However for analyzing rough surfaces or even wafer edges, it is ideal.[31]

In this study, a PHI TRIFT II™ ToF-SIMS instrument was used, utilizing a $^{69}Ga^+$ beam. Sample bias was at 3.0 kV, either positive or negative depending on secondary ion of interest polarity with extraction lens set to ground potential. Dual micro channel plates were used for pulse counting of ions.

1.2.3 Vapor Phase Decomposition – Droplet Collection (VPD-DC)

VPD-DC is a physical pre-concentration technique with two parts. The first part, vapor phase decomposition (VPD), is accomplished by placing a wafer into a closed chamber containing a small, open container of 49% HF. HF vapor evolves from the solution, condenses

on the wafer surface and dissolves all oxide layers present on the wafer, stopping on the silicon interface. The end result is a hydrophobic silicon surface suitable for the second part of the technique, droplet collection (DC), wherein a 50-500 μL droplet of chemical solution is placed on the wafer using a micropipette and then scanned around the entire wafer surface. This results in collection of all metals on the surface into the droplet of chemical.[29,34] Collection is normally done with a dilute HF and H_2O_2 mix (typically 0.49% HF and 1% H_2O_2) to maintain a hydrophobic surface and to improve the collection efficiency of the metals, especially for ones with a redox potential higher than that of Si (e.g. Cu). Scanning of the droplet may be done by hand (provided the analyst has sufficient manual dexterity) or by machine (multiple automated systems are available on the market). This technique achieves two goals which are very useful for research: 1) a lower detection limit and 2) a global, average value of metal contamination on a wafer, eliminating the need to measure numerous spots with TXRF or ToF-SIMS to get statistically valid results.

Once the metals are collected, they can be analyzed via several techniques including TXRF, ICP-MS (inductively coupled plasma mass spectroscopy), or GFAA (graphite furnace atomic absorption). To analyze using TXRF, the droplet is dried on the wafer to eliminate the liquid matrix. The residue is then measured using normal TXRF analysis procedures. A sensitivity increase results that is proportional to: the area of the wafer (i.e πr^2 = 176x for a 150mm wafer, 314x for a 200 mm wafer, and 707x for a 300 mm wafer) multiplied by the collection efficiency of the droplet solution (80% for most metals and 20% for Cu in this work). This sensitivity increase due to preconcentration of the metals allows for shorter analysis time and detection limits in the 1×10^7 to 1×10^8 at/cm^2 range, depending on a given instrument's detector sensitivity.

Alternatively, the droplet can be removed from the hydrophobic wafer using a clean micropipette and then analyzed using either ICP-MS or GFAA, depending on: metal of interest, detection limit required, and equipment availability. This allows detection limits on the order of 10^8 at/cm^2 to be achieved.

1.2.4 Light Scattering for Surface Defectivity (Censor ANS-100)

Laser light scattering has become the de facto method for measuring surface defects on Si wafers. This technique is based on scanning a laser across a polished wafer surface and measuring the intensity of the light that is scattered by imperfections on the surface. The laser wavelength (488 and 514 nm in this case), energy (25 mW), collection angles (5-18 degrees), refractive index delta between defect and surface, and wafer surface roughness all contribute to the lower limit of detection.

As shown in Figure 1.9, the Censor ANS-100 used in this study operates by radially scanning a laser perpendicular to the surface of a rotating wafer and analyzing the scattered light that is collected by the optics. Calibration is achieved by putting latex sphere particles of known size on a wafer surface and evaluating the signal generated. When this is done across a range of latex particle sizes, a response curve is generated that allows the instrument to output the quantity of particles detected, normalized to the corresponding latex sphere equivalent (LSE) of scattered light intensity. The Censor ANS-100 used here had a lower level of detection (LLD) of 0.10 micron LSE.

1.2.5 Voltage Breakdown (V_{bd}) and Charge to Breakdown (Q_{bd}) of Gate Oxides

As one of the key device parameters that is of interest to device manufacturers, there are two methods of measuring gate oxide integrity (GOI) that will be used in this dissertation. The first is known as voltage to breakdown (V_{bd}) measurement. In this case, a non-conducting oxide

film is placed under an ever increasing voltage via an electrode of known area until it catastrophically breaks down and begins to pass current without impedance. The voltage at

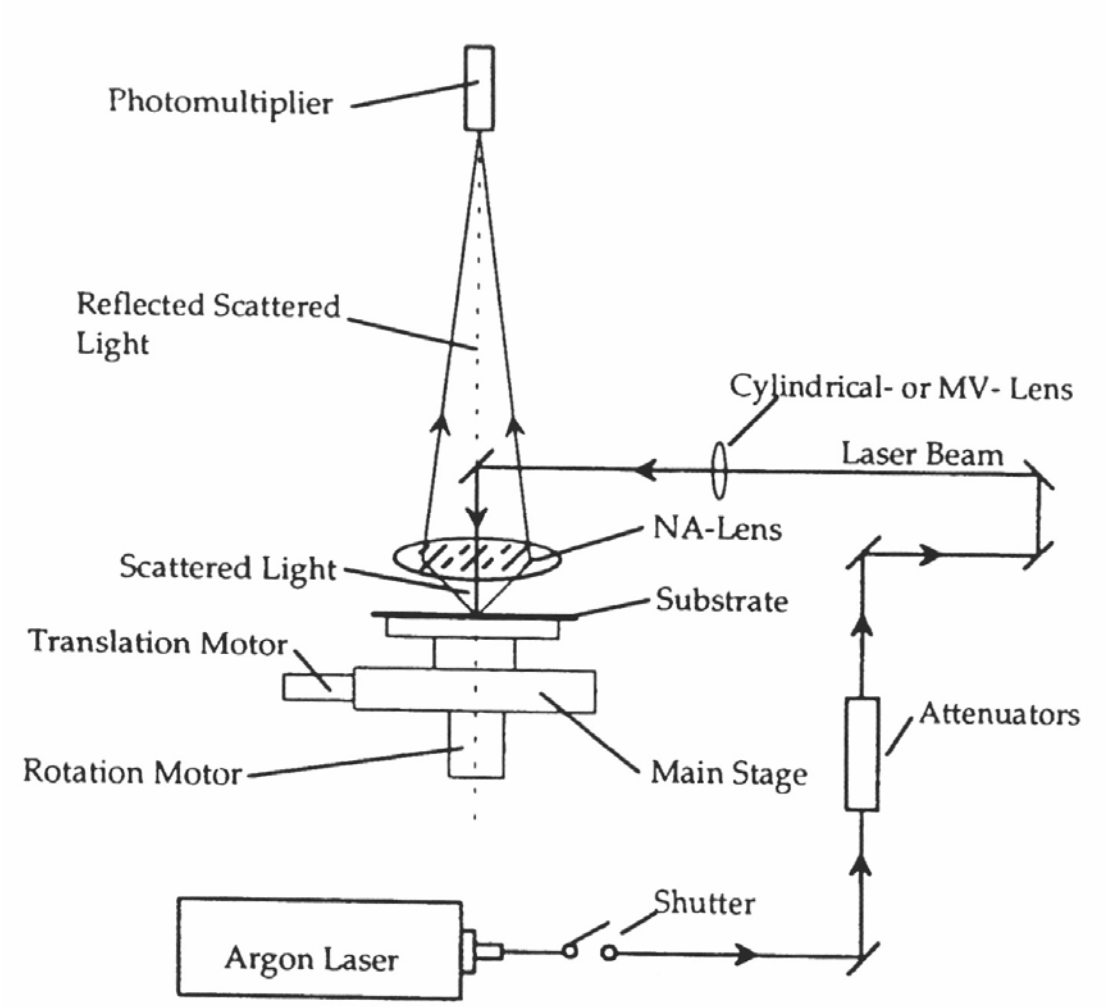

Figure 1.9: Censor ANS-100 instrument schematic.

which this happens is noted and after measurement of many capacitors (hundreds or more) on a wafer, a histogram is generated showing at what voltages, normalized to the oxide thickness as MV/cm, the oxide capacitors broke down. The more defective an oxide, the lower the voltage at which it breaks down. Metal contaminants in an oxide can cause premature breakdown and so

this method is a useful technique for evaluating the impact that metal contaminants will have on a semiconductor device.

The second method of measuring GOI is known as charge to breakdown (Q_{bd}). In this test, the oxide is placed under a constant bias that results in a fixed amount of charge passing across it. The bias is held constant until the oxide breaks down and passes charge freely with voltage drop. The total charge that is passed prior to break down is plotted in a Weibull plot for a population of gates and then checked for normality. The y-axis for the Weibull distribution is a double logarithmic transformation:

$$\ln(-\ln[1-f_i]) \qquad 1.2$$

where f_i is the cumulative distribution value for the i^{th} Q_{bd} point. This is plotted against ln(time).[35,36] Evaluation of the Weibull distribution allows the assignment of various possible failure modes for gate oxide breakdown. In the scope of this work, a much simpler analysis is used wherein lower Q_{bd} values indicate lower oxide quality and higher the concentration of metal in the oxide.

1.3 Bulk Analysis Techniques

1.3.1 Microwave Photoconductance Decay (μPCD)

Minority carrier lifetime (MCLT) in bulk silicon is a metric that is closely correlated to the overall quality of a silicon crystal matrix. One of the most common methods used to quantify it is μPCD. When a silicon wafer is probed by a pulsed laser at infrared wavelengths, the photoelectric effect results in generation of excess minority charge carriers (electrons for p-type silicon and holes for n-type silicon) in the silicon substrate that are promoted from the valence band to the conduction band, causing a transient change in wafer conductivity that returns to equilibrium levels as the carriers recombine in the matrix and return to the valence band. If the

silicon crystal if perfect, the minority carriers will take the maximum time possible to recombine and return to equilibrium. Metal contaminants in the silicon matrix insert energy levels in the middle of the silicon bandgap which make it easier for minority carriers to move from the conduction band back to the valence band, resulting in an overall reduction in the lifetime of the minority carriers. Figure 1.10 shows several metals of importance to this dissertation and the energy levels that they create in the silicon bandgap. These levels are designated by their distance from either the conduction band (E_c) or the valence band (E_v).

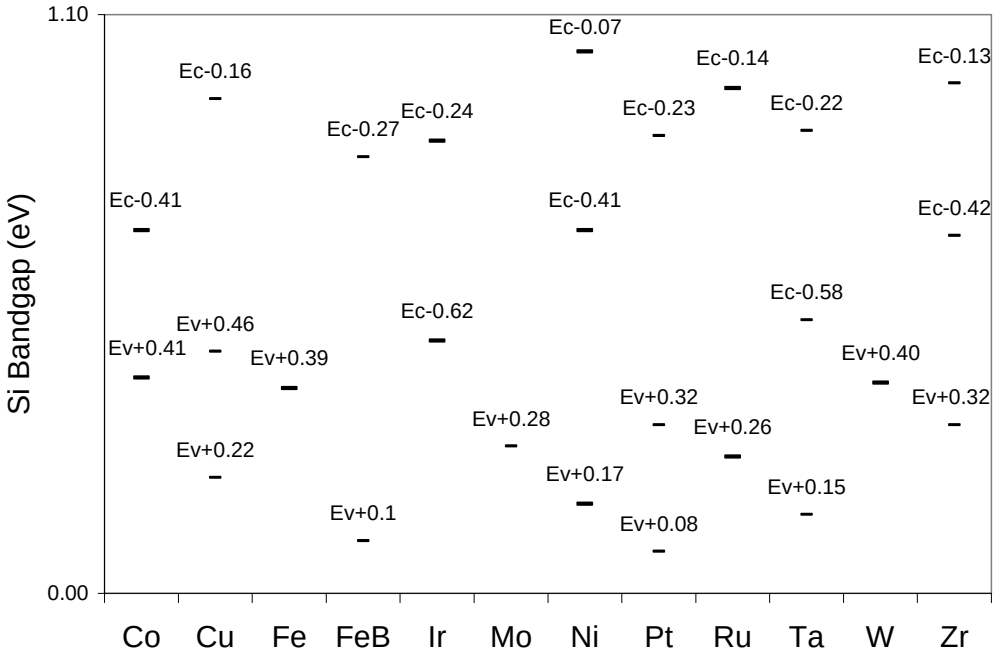

Figure 1.10: Energy levels inserted in to the silicon bandgap by metal impurities.

The lifetime of this change in conductivity is measured by monitoring microwave power reflectance from the surface of the wafer (Figure 1.11). Assuming the decay behavior of the reflectance is dominated by the total population of excess carriers, the slope of the decay with

time can be used to extract the minority carrier lifetime. It is important to note that carrier recombination can occur both in the bulk and at the surface, as described by:

$$\frac{1}{\tau_{eff}} = \frac{1}{\tau_{surf}} + \frac{1}{\tau_{bulk}} \qquad 1.3$$

As τ_{eff} is what is measured and τ_{bulk} is the value of interest in this measurement, it is critical that τ_{surf} be made as large as possible. Under normal conditions, τ_{surf} is very short due to the large number of unreacted silicon orbitals containing an unpaired electron (dangling bonds) projecting

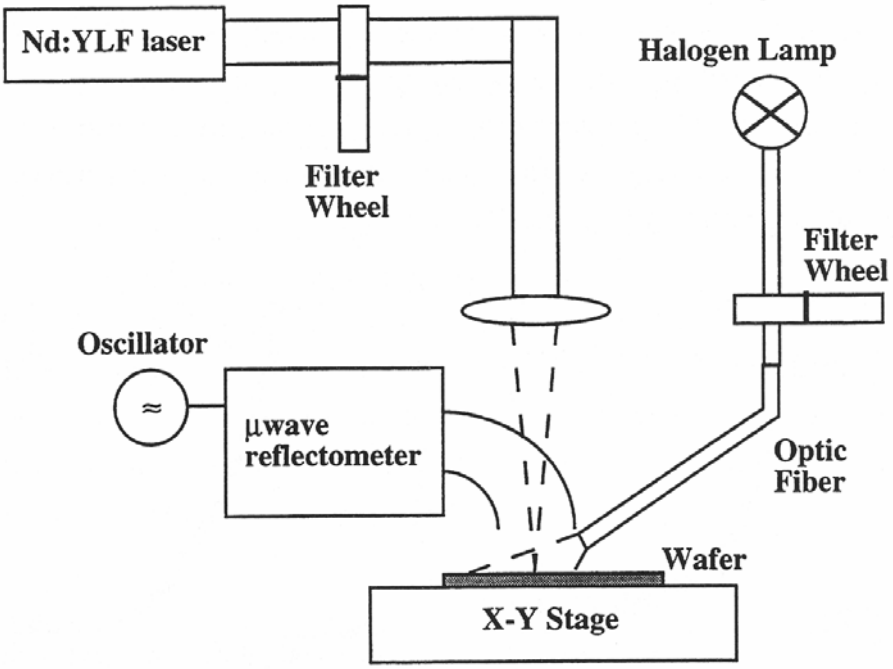

Figure 1.11: Schematic of instrument used to measure minority carrier lifetime via microwave power reflectance. IR wavelength laser generates electron-hole pairs in crystal which induces a transient change in microwave reflectance as carrier pairs recombine.

from the surface of the silicon crystal. Satisfying those dangling bonds is achieved in one of several ways: thermally oxidizing the wafer surface (generating silicon-oxygen bonds), using HF

(generating silicon-hydrogen bonds) or using iodine in methanol solution (generating silicon-iodine bonds).[39]

It is also important to note that the bulk lifetime of minority carriers can be further described by:

$$\tau_{bulk,h} = \frac{1}{\sigma_h v_{th} N_t} \text{ and } \tau_{bulk,e} = \frac{1}{\sigma_e v_{th} N_t} \qquad 1.4, 1.5$$

where σ_h and σ_e are the capture cross sections for holes and electrons, repectively, ν_{th} is the thermal velocity of carriers, and N_t is the concentration of recombination centers in the semiconductor.[38] Since the lifetime of a minority carrier, whether it is an electron or a hole, is partially a function of the capture cross section of the defect center where recombination occurs, whether it is a metal, lattice defect, or oxygen precipitate, the capture cross section and therefore MCLT impact for a given defect can be extremely different for holes and electrons.

μPCD is extremely sensitive to any defects in the bulk silicon matrix. It is not however, not a spectroscopic technique, so care must be taken when using it in research to make sure that conditions are tightly controlled so that the phenomenon of interest does not become convolved with other variables. In this study, MCLT was measured using either a manual Lifetime Mapping System MRM from Phoenicon, operating in time resolved microwave conductivity mode or with an automatic Leo Geiken Micro-τ, MCLT analyzer that allows mapping of entire wafers. A Nd:YLF laser was used to generate the carriers and a halogen lamp was used to generate the microwaves whose reflection quantifies the lifetime of the carriers.

1.3.2 Surface Photovoltage (SPV)

While MCLT measures minority carrier recombination via the decay of a population from a given point in time, SPV (Figure 1.12) measures the decay of a population from a given point in space, allowing extraction of the minority carriers' diffusion length (L). In both cases,

increasing distance, whether in time or space marks a return to equilibrium conditions. In one sense, measuring L is simply an alternative to measuring MCLT as both are related to one another via the equation:

$$L = \sqrt{D\tau_{bulk}} \qquad 1.6$$

This equation is only valid if D is precisely known and if L and τ_{bulk} correspond exclusively to bulk properties.[38] Since this is very difficult to achieve, L and MCLT are generally best related experimentally under controlled circumstances.

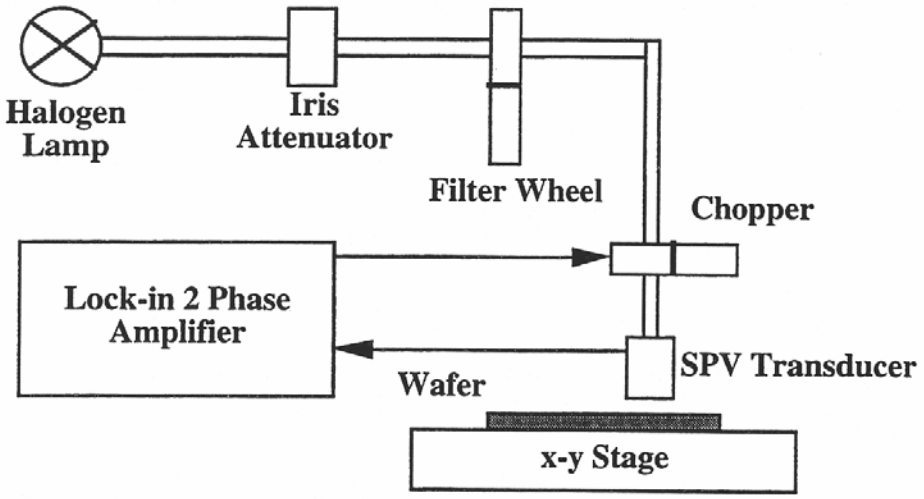

Figure 1.12: Surface photovoltage instrument diagram.

SPV instruments measure L by using bright light illumination of the front surface of the wafer and then measuring the resultant voltage that develops between the illuminated front side of the wafer and the non-illuminated back side. By varying the wavelengths of the illumination via filters, minority carriers can be generated at various depths in the silicon substrate. How many of these are able to migrate to the surface to have an impact on the measure voltage difference is directly correlated to the quality of the silicon matrix. The higher the quality, the

more carriers that survive to reach the surface, while the lower the quality, the fewer that survive. Relating measured photovoltage to illumination penetration depth allows extraction of the average diffusion length, L, of the minority carriers via the equations:

$$\Delta V = \frac{\Phi_{eff}}{A} \frac{\alpha L}{\left(s_f + \frac{D}{L}\right)(1+\alpha L)} \qquad 1.7$$

and

$$\Phi_{eff} = (1-R)\Phi \qquad 1.8$$

where α is the light absorption coefficient in the semiconductor, σ_f is the surface recombination velocity on the illuminated surface, D is the minority carrier diffusivity, A is the coefficient dependent on the substrate doping density, Φ_{eff} is the effective incident photon flux, R is the surface reflectivity and Φ is the incident photon flux. With suitable selection of measurement conditions, it is possible to extract diffusion lengths that are greater than the thickness of the wafer.[39,40]

When used to extract the diffusion length only, SPV is a non-spectroscopic technique like μPCD with the additional advantage that it doesn't require a well passivated surface to make accurate measurements. Additionally however, SPV can be used to quantify Fe in bulk silicon to very low detections limits. At room temperature, Fe atoms in B doped silicon form FeB pairs. This pairing reduces the capture cross section of the Fe for minority carriers. A short thermal treatment of 200-250 °C for 10 minutes is enough to dissociate these pairs. Alternatively, the pairs can be photodissociated using a short, 10 s, light pulse of 20 W/cm^2 energy. This has the beneficial impact of only dissociating the FeB pairs and not other pairs like CrB which could impact the measurement.[41] Once the Fe is separated from the B, it becomes a much more

efficient capture center for minority carriers. By measuring L before and after photodissociation, it is possible to extract the bulk concentration of Fe using the equation:

$$[Fe_{bulk}](at/cm^3) = 1.06 \times 10^{16}\left(\frac{1}{L^2_{aft}} - \frac{1}{L^2_{bef}}\right) \qquad 1.9$$

where the values for L_{bef} and L_{aft} are expressed in microns.[42] The published detection limit of this method for wafers with a thickness of 650 mm is ≈ 4 x 10^9 at/cm^3 of Fe in the bulk.[43] All SPV measurements were performed using a model CMS-IIIA surface photovoltage system manufactured by Semiconductor Diagnostics Inc (Figure 1.11).

1.4 Solution Analysis Techniques

1.4.1 Inductively Coupled Plasma Mass Spectroscopy (ICP-MS)

ICP-MS is very widely used in the semiconductor industry for the analysis of trace levels of metals in chemical solutions. Detection limits on the order of 10 parts per trillion are possible, depending on element and sample matrix.[44] The instrument is able to measure elements across the range of the entire periodic table, provided they can be ionized to cations in measurable quantities. Mass spectroscopy has been a staple technique for chemists for many decades with the quadropole and mass sector analyzers being the most popular. For semiconductor applications, the quadropole mass analyzer is most commonly used (Figure 1.13).

During ICP-MS analysis, a liquid sample is atomized into an Ar plasma that is generated via inductive coupling at a pressure that is slightly above ambient. The sample atoms become ionized during collisions with the Ar ions in the plasma. A percentage of the sample then passes through a sampling cone into a region where pressure drops to the millitorr regime after which a further reduced portion of the sample passes through a skimmer cone into the next chamber of the instrument which is kept at pressures in the 10^{-7} torr range. In this chamber the ions encounter an accelerating voltage which sends them toward the detector. The accelerating

voltage is tuned so that only ions of the desired mass/charge ratio make it to the detector. In this manner a large mass range can be analyzed for a given sample.[45] With the introduction of direct injection nebulizers, sampling rates on the order of 20 µl/min can now be successfully analyzed.

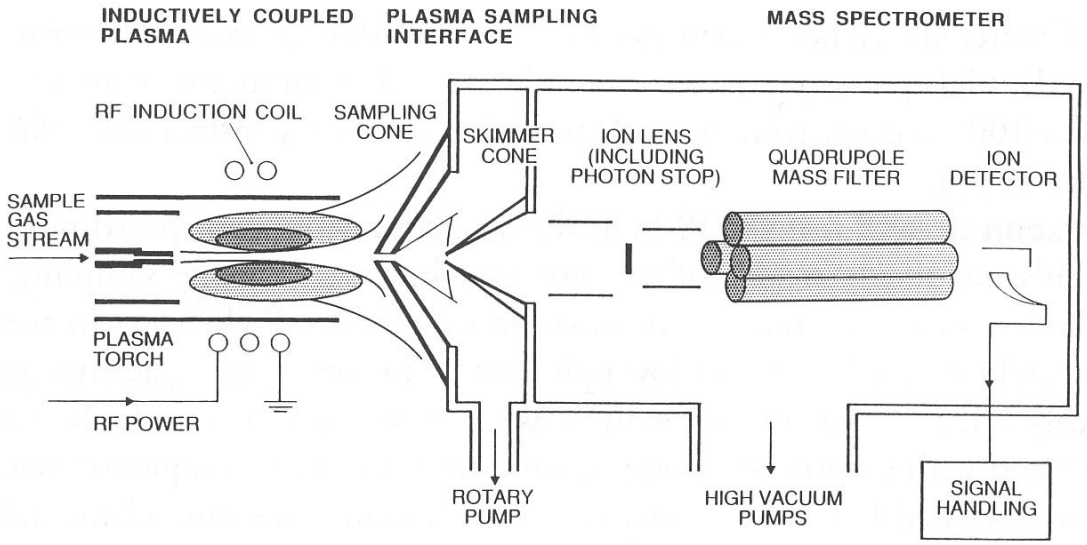

Figure 1.13: Diagram of a inductively coupled mass spectrometer utilizing a quadropole mass spectrometer.

With mass resolution on the order of 200 being achieved, ICP-MS instruments have trouble getting low detection limits for K, Ca and Fe due to interferences (ArH for K, Ar for Ca, and ArO for Fe) from carrier gas ions. Na is troublesome as well simply to due to its ubiquity in the environment. In order to measure these elements to part per trillion detection limits, a different technique is required, unless a dynamic reaction cell™ (DRC™) is utilized which removes the interfering gas ion species.

In this study, the Elan II® from Perkin Elmer was used for ICP-MS analyses, either with or without the DRC™ which utilizes a cross flow of NH_3 gas to eliminate ions whose

mass/charge ratios cause interferences with the metals of interest. Samples were nebulized using a Teflon® nebulizer from ESI instruments and injected via a platinum injection tube into a spray chamber built by Air Liquide analytical laboratories.

1.4.2 Graphite Furnace Atomic Absorption (GFAA)

Atomic absorption spectroscopy is used to quantify concentrations of solute atoms in a solvent matrix. As was discovered in the 18th century, when an element is thermally heated, its atoms begin to give off light of characteristic wavelengths. This atomic emission is due to the relaxation of electrons from excited state atomic orbitals to ground state atomic orbitals with resultant release of light of energy $h\nu$, equal to the quantized energy difference between the excited and ground state orbitals of the atom.[46] This phenomenon has been used for centuries to confirm discoveries of new elements.[47]

Conversely, if an atomic gas is illuminated with light corresponding to the energy of a ground to excited state transition, the atoms will absorb this light and move to an excited state. The amount of light lost to this reaction can be measured and related to the number of atoms present in the beam path. This is the fundamental principle of atomic absorption. Because the energy of electron transitions is quantized, the frequency of light needed to most efficiently cause the transition can only be generated by the atomic emission of the element that is being quantified in the analyte. This is most commonly achieved by using hollow cathode lamps whose cathode is composed of the element of interest. For this reason, atomic absorption spectrometers can only detect one element at a time and require emission source changes to move from one atom to another. Fortunately, samples sizes can be in the range of microliters, allowing a small amount of sample to be divided and measured for multiple atoms.[46]

The graphite furnace atomic absorption spectrometer uses a resistively heated carbon graphite tube to provide the energy needed to evaporate the sample into the path of the exciting light. Temperatures of 1200 °C to 3000 °C can be achieved in this manner. For very high purity samples, such as the chemicals used in the semiconductor industry, the graphite furnace provides a lower background contamination level relative to a flame atomizer and so has become the preferred technique for high purity applications. Detection limits of less than 100 part per trillion (ppt) are possible. Due to the limitation of having to change excitation sources for each metal to be analyzed, GFAA is only used for elements that ICP-MS has trouble with, i.e. Na, K, Ca, and Fe. In this study, GFAA analysis was performed on a Varian GFAA 400 using Zeeman background correcton.

1.4.3 Real Time O_2 Overpressure Analysis of H_2O_2 Decomposition Rate

The decomposition of H_2O_2 can be summarized by the following chemical reaction:

$$H_2O_2(aq) \rightarrow 2H_2O(l) + O_2(g)\uparrow \qquad 1.10$$

There are two common ways in which to monitor the decomposition of H_2O_2 in a solution. The first is to sample the mixture at time intervals and then to titrate the H_2O_2 remaining in each sample using the standard iodometric technique. This method measures the remaining H_2O_2 by the oxidation of I^- to I_2 and has been in use for decades as the standard method for determination of H_2O_2 concentration.[48] It is extremely accurate but is too slow for dynamic monitoring of peroxide concentration.

In the second technique, the amount of O_2 liberated during the decomposition is calculated from the measured change in pressure over time. This is accomplished by placing an initial amount, n_0, of H_2O_2 in a vessel of fixed volume (Figure 1.14). As the H_2O_2 decomposes, O_2 passes out of the reaction vessel, through a DI water filter to remove any unwanted

contaminants (residual HCl in this dissertation) and increases the partial pressure in the fixed gas volume, V_g downstream of the scrubber. When it achieves a fixed over pressure, in this case, 5 millitorr, it is vented to atmosphere, and allowed to re-pressurize as the reaction continues.[49,50] Thus, if we let n = mmol of H_2O_2, n_g = mmol of O_2, and p_g = partial pressure of O_2, then, combining the reaction stoichiometry:

$$-2\Delta n = \Delta n_g \qquad 1.11$$

with the ideal gas law:

$$\Delta p_g V = \Delta n_g RT \qquad 1.12$$

gives the following relationship

$$\Delta n = \frac{-\Delta p_g V_g}{2RT} \qquad 1.13$$

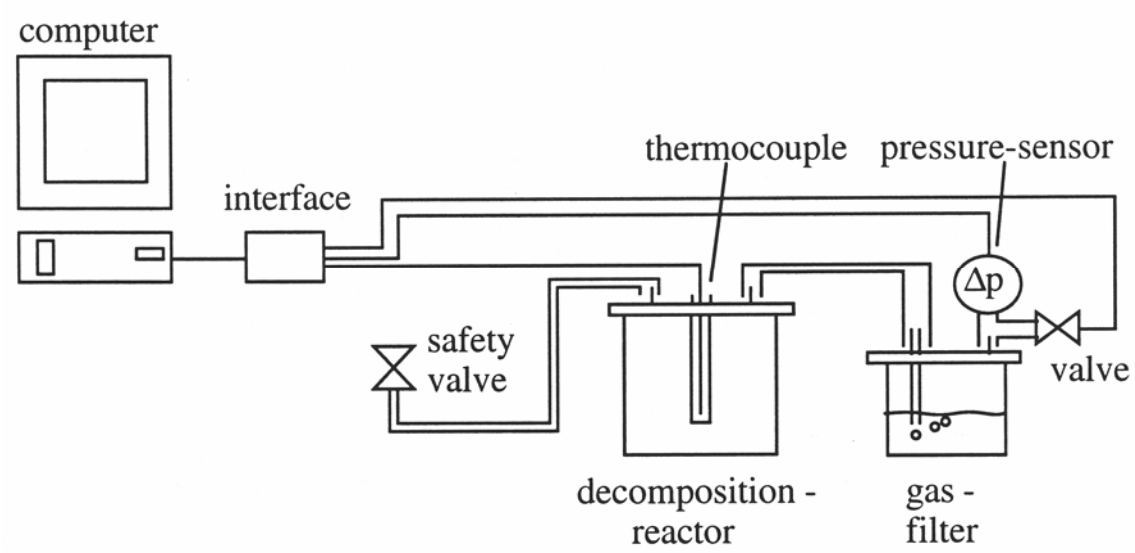

Figure 1.14: Instrument used to measure real time decomposition of H_2O_2.

The advantage of this technique over titration is that a dynamic H_2O_2 concentration can be measured in real time and the decomposition rate can be accurately quantified. In practice, the time, Δt, required to build up a fixed amount of over pressure, Δp_g, is measured. From this, the decomposition rate can be calculated:

$$\frac{\Delta n}{\Delta t} = \frac{-\Delta p_g V_g}{2RT\Delta t} \qquad 1.14$$

Integrating over the time of the measurement yields the residual H_2O_2, n, while dividing the decomposition rate by n_0 gives the normalized decomposition rate:

$$r_n = \frac{-dn/dt}{n_0} \qquad 1.15$$

When graphed versus time, the normalized decomposition rate gives an immediate indicator of how rapidly the reaction is proceeding, as the more negative the slope, the more vigorous the reaction. This is developed further in Chapter 2.

1.5 Summary

Making sense of metal interactions with silicon during semiconductor processing is dependent on the interplay of a great deal of analytical science and technology. It is only in the past 15-20 years that a critical mass of chemical, surface, and solid state techniques with the requisite low detection limits have become available, allowing the investigations that will be presented in this dissertation. Far from demonstrating any inherent skill or capability in the investigator, this is merely another reminder that every generation of scientists is standing on the shoulders of the generations that came before.

1.6 References

(1) *International Technology Roadmap for Semiconductors 2003 Edition*, **2003** http://public.itrs.net/Files/2003ITRS/Home2003.htm, International Sematech (May 1, 2005)

(2) Mertens, P.W.; Meuris, M.; Verhaverbeke, S.; Heyns, M.M. ; Schnegg, A. ; Graf, D. ; Phillipossian, A. *IES 38th Annual Technical Meeting 1992 Proceedings Vol 1*; IES: Mount Prospect, Illinois, 1992; p 475.

(3) Bergholz, G.; Zoth, F.; Gelsdorf, F.; Kolbesen, B *Defects in Silicon II 91-9*; eds. Bullis, W.M.; Gosele, U.; Shimura, F; The Electrochemical Society: Pennington, NJ, 1991; p 21

(4) Zoth, G; Bergholz, W. *J. Appl. Phys.* **1990** *67* 6764.

(5) Kola, R.R.; Rozgonyi, G.A.; Li, J.; Rogers, B; Yan, T. Y.; Bean, K.E.; Lindberg, K. *Appl. Phys. Lett.*, **1989** *55* 2108.

(6) Henley, W.; Jastrzebski, L; Haddad, N. *Proceedings of the 1993 IEEE International Reliability Physics Symposium*, 1993; p 22.

(7) Goetzberger, A.; Shockley, W. *J. Appl. Phys.* **1960** *31* 1821.

(8) Katz, L.E. *J. Electrochem. Soc.* **1974** *121* 969.

(9) Busta, H.H.; Waggener, H.A.; *J. Electrochem. Soc.* **1977** *124* 1424.

(10) Ward, P.J.; *J. Electrochem. Soc.* **1982** *129* 2573.

(11) Miyazaki, M. *Jpn. J. Appl. Phys.* **1991** *30* 295.

(12) Miyazaki, M. *Jpn J. Appl. Phys.* **1995** *34* 409.

(13) Streetman, B. *Solid State Electronic Devices, 4th Ed.* Prentice Hall: Upper Saddle River, NJ, 1995 ; p 300.

(14) Williams, C.K.; Hamaker, R.W.; Ganeson, S.G.; Kuehn, R.T.; Swartzel, K.R.; O'Sullivan, J. *J. Electrochem. Soc.* **1995** *142* 303.

(15) Honda, K.; Nakanishi, T.; Ohsawa, A.; Toyokura, N *J. Appl. Phys.* **1987** *62* 1960

(16) Takiyama, M.; Ohtsuka, S.; Hayashi, S.; Tachimori, M. *Semiconductor Silicon/1994 94-10* eds. Huff, H; Bergholz, W.; Sumino, K. The Electrochemical Society: Pennington, NJ, 1994; p 346.

(17) Yamamichi, S.; Muramatsu, Y.; Lesaicherre, P-Y. ; Ono, H Jpn. *J. Appl. Phys.* **1995** *34* 5188.

(18) Gilbert, S.R.; Ritchey, D.; Tavassoli, M.; Amano, J.; Colombo, L.; Summerfelt, S.R. *J. Electrochem. Soc.* **2001** *148* 195.

(19) Visokay, M.R.; Chambers, J.J.; Rotondaro, A.L.P.R.; Colombo, L. *Appl. Phys. Lett.* **2002** *80* 1.

(20) Chyan, O; Arunagiri, T.; Hurd, T. *Electrochem and Sol. State Lett.* **2004**, 7(8), G154.

(21) Kern, W.; Puotinen, D.A. *RCA Review* **1970**, *31*, 187.

(22) Meuris, M.; Heyns, M.; Verhaverbeke, S.; Mertens, P.; Philipossian, A.; *1991 Microcontamination Conference Proceedings* Canon Communities Inc.: Santa Monica, CA 1991; p 658.

(23) Dhanda, S.; Chiarello, R.P.; Helms, C.R.; Gupta, P. *Electrochemical Society Proceedings 97-35;* The Electrochemical Society: Pennington, NJ, 1997; 113.

(24) Quirk, M.; Serda, J. *Semiconductor Manufacturing Technology* Prentice-Hall Inc.: Upper Saddle River, NJ, 2001; p 537.

(25) Prange, A. *Spectrochemica Acta* **1989** *44B* 437.

(26) Kregsamer, P. *Spectrochemica Acta* **1991** *46B* 1333.

(27) Aiginger, H. *Spectrochemica Acta* **1991** *46B* 1313.

(28) Knoth, J.; Schwenke, H.; Weisbrod, U. *Spectrochemica Acta* **1989** *44B* 477.

(29) Neumann, C.; Eichinger, P. *Spectrochemica Acta* **1991** *46B* 1369.

(30) Wieckhardt, C; Moritz, F.; Grotemeyer, J. *Mass Spectrometry Reviews* **1996** *15* 139.

(31) Douglas, M. *T.I. Technical Journal* **1995** *12(5)* 19.

(32) Benninghoven, A. *Angew. Chem. Int. Engl.* **1994** *33* 1023.

(33) Douglas, M; Chen, P.J. *Surf. Interface Anal.* **1998** *26* 984.

(34) Meuris, M.; Heyns, M.; Kuper, W.; Verhaverbeke, S.; Philipossian, A.; *ULSI Science and Technology 1991*, ed. Andrews, J.M.; Celler, G.K.; Vol 91-11, The Electrochemical Society: Pennington, NJ, 1991.

(35) Wolf, S. Silicon *Processing for the VLSI Era, Vol 3: The Submicron MOSFET* Lattice Press: Sunset Beach, California, 1995; p 438.

(36) Vogel, E.; Misra, V. *Handbook of Silicon Semiconductor Metrology* ed. Diebold, A. Marcel Dekker Inc: New York, NY 2001; p 85.

(37) Stephens, A.W. *J. Appl. Phys.* **1994** *76* 363.

(38) Grove, A. *Physics and Technology of Semiconductor Devices* John Wiley and Sons: New York, NY, 1967.

(39) Lagowski, J.; Kontkiewicz, M.; Jastrzebski, L.; Edelman, P. *Semicond. Sci. Technol.* **1992** *7* 185.

(40) Lagowski, J.; Kontkiewicz, M.; Jastrzebski, L.; Edelman, P. *Appl. Phys. Lett.* **1993** *63* 2902.

(41) Lagowski, J.; Kontkiewicz, M.; Jastrzebski, L.; Edelman, P. *Appl. Phys. Lett.* **1993** *63* 3043.

(42) Zoth, G.; Bergholz, W. J. Appl. Phys. **1990** *67* 6764.

(43) Jastrzebski, L.; Lagowski, J.; Kontkiewicz, M.; Edelman, P. *J. Electrochem. Soc.* **1993** *140* 1152.

(44) Streusand, B. *Encyclopedia of Materials Characterization* eds. Brundle, C.R.; Evans, C.; Wilson, S.; Butterworth Heinman: Boston MA, 1992; p 624.

(45) Skoog, D. *Principles of Instrumental Analysis, 3rd Ed.;* Saunders College Publishing: Philadelphia PA, 1985; p 523.

(46) Skood, D.A.; West, D.M.; Holler, F.J. *Fundamentals of Analytical Chemistry, 7th Ed.;* Saunders College Publishing: Philadelphia, PA, 1996; p 611.

(47) Emsley, J. *Nature's Building Blocks;* Oxford University Press: New York, 2001.

(48) Laitinen, H.A. *Chemical Analysis;* McGraw Hill: NY, 1960; p 411.

(49) Schmidt, H.F; Meuris, M.; Mertens, P.W.; Verhaverbeke, S.; Heyns, M.M.; Kubota, M.; Dillenbeck, K. *IES 39th Annual Technical Meeting Proceedings Vol. 1*; IES: Mount Prospect, Illinois, 1993; p 238.

(50) Schmidt, H.F.; Meuris, M.; Mertens, P.W.; Rotondaro, A.L.P.; Heyns, M.M.; Hurd, T.Q.; Hatcher, Z. *Jpn. J. Appl. Phys.* **1995** *34* 727.

(51) Liu, B.Y.H. *J. Electrochem. Soc* **1993** *140* 1403.

CHAPTER 2

INVESTIGATION OF THE SC2 CLEAN (HCL, H_2O_2, AND H_2O MIXTURE)

2.1 Introduction

The SC2 clean has been used for metal removal from silicon wafers for over thirty years following its introduction as part of the RCA cleaning sequence of SC1-SC2.[1] Typically it is used in the originally proposed volume ratio of 1:1:5 (37%HCl: 30%H_2O_2: H_2O) and at temperatures of 70 °C to 85 °C. Its primary purpose is to remove metals from the wafer surface prior to high temperature processing. The ratio and temperature chosen by a particular wafer fab is traditionally arrived at via empirical testing done in a production setting. While this approach meets the need of creating a robust manufacturing process, it doesn't provide any insight into why and how the SC2 solution works the way it does. This kind of insight is useful for reducing the time it takes to define the most effective and least expensive SC2 based cleaning process for a given device or technology.

Three specific characteristics of the SC2 clean are addressed in this chapter: H_2O_2 decomposition, metal removal, and particle addition. These three characteristics are key as decomposition will impact usage and cost, metal removal is the primary purpose of the SC2 clean, and particle addition is a negative aspect of the SC2 solution that must be minimized as particles on the device surface are a major source of yield loss in manufacturing. Based on what is learned of these three characteristics, an optimized clean is tested in a manufacturing process development facility.

H_2O_2 is known to be a very reactive molecule. It readily decomposes on contact with organics and transition metals and is also sensitive to extremes of temperature and pH. In all cases, the overall decomposition reaction can be summarized as:

$$2H_2O_2 \rightarrow 2H_2O + O_2 \qquad 2.1$$

Of specific interest to wafer cleaning is the reaction of H_2O_2 with transition metals, in particular Fe, as it has been shown to lead to catalytic decomposition of basic SC1 solutions with deleterious impact on gate oxide integrity.[2] The exact mechanism of H_2O_2 decomposition is still a matter of debate, with two different mechanisms currently proposed. Analytically conclusive determination of which mechanism is the correct one has not occurred to date as the measurable differences between the two models are very subtle.[3,4]

The first suggested pathway is via radical formation:[5]

$$Fe^{3+} + H_2O_2 \rightarrow Fe^{2+} + H^+ + HO_2^{\bullet} \qquad 2.2a$$

$$Fe^{2+} + H_2O_2 \rightarrow Fe^{3+} + OH^{\bullet} + OH^- \qquad 2.3a$$

$$OH^{\bullet} + H_2O_2 \rightarrow HO_2^{\bullet} + H_2O \qquad 2.4a$$

$$Fe^{3+} + HO_2^{\bullet} \rightarrow Fe^{2+} + H^+ + O_2 \qquad 2.5a$$

$$Fe^{2+} + OH^{\bullet} \rightarrow Fe^{3+} + OH^- \qquad 2.6a$$

$$Fe^{2+} + HO_2^{\bullet} \rightarrow Fe^{3+} + HO_2^- \qquad 2.7a$$

While the second suggested pathway is via complex formation:[6]

$$Fe_{3+} + H_2O_2 \rightarrow Fe^{2+} + HO_2^- + H^+ \qquad 2.2b$$

$$Fe^{2+} + H_2O_2 \rightarrow Fe^{3+} + HO^{\bullet} + HO^- \qquad 2.3b$$

$$HO^{\bullet} + H_2O_2 \rightarrow H_2O + HO_2^{\bullet} \qquad 2.4b$$

$$HO_2^{\bullet} + Fe^{3+} \rightarrow Fe^{2+} + H^+ + O_2 \qquad 2.5b$$

$$HO_2^{\bullet} + Fe^{2+} \rightarrow Fe^{3+} + HO_2^- \qquad 2.6b$$

$$HO^{\bullet} + Fe^{2+} \rightarrow Fe^{3+} + HO^- \qquad 2.7b$$

In either case, the presence of an excess of H^+ is expected to interfere with steps in the proposed reaction pathways. In the case of the radical path both reactions 2.2a and 2.5a could be expected to be affected by an abundance of H^+ in solution as this would tend to push those reactions in the opposite direction. In the case of the complex formation pathway, Steps 2.2b and 2.2b could be expected to be impacted as the dissociation of H_2O_2 into H^+ and HO_2^- as well as the dissociation of $HO_2^{\cdot}$ into H^+ and O_2 would be greatly reduced in the presence of a strong acid generating an abundance of H^+.

In this study, the behavior of the H_2O_2 in acidic SC2 is determined via real time measurements of its decomposition using a technique previously developed to measure decomposition of H_2O_2 in basic SC1 solutions.[2,7] The impact of HCl concentration, temperature, and metal contamination are measured independently of one another. The lifetime of the H_2O_2 in SC2 solution, when used in the manner that is typical in semiconductor manufacturing, can be very short. Metal catalyzed H_2O_2 decomposition that is observed in SC1 solution is not observed in SC2, consistent with the proposed decomposition mechanisms.

The result of the decomposition testing leads to the question of whether or not H_2O_2 is actually necessary for SC2 to perform its intended function of metal removal. After testing metal removal of HCl solutions with and without the addition of H_2O_2, various dilutions of HCl alone are tested to determine how much is needed to remove metals from silicon and silicon oxide surfaces. Much less HCl is needed than initially expected, opening up the possibility of targeting HCl concentrations that allow manipulation of the surface charge on the silicon oxide wafer surface, resulting in effective metal removal with greatly reduced particle deposition. Finally, the reduction of this work to practice in a wafer fab is described, including measurement of its impact on gate oxide integrity (GOI) relative to a baseline process.

2.2 H_2O_2 Decomposition in SC2

2.2.1 Experimental

An SC2 solution of known concentration was placed into the reaction vessel of the instrument described in Section 1.4.3 and shown again in Figure 2.1. Temperature was controlled by immersing the reaction vessel in a thermostatic heating bath and monitored using a

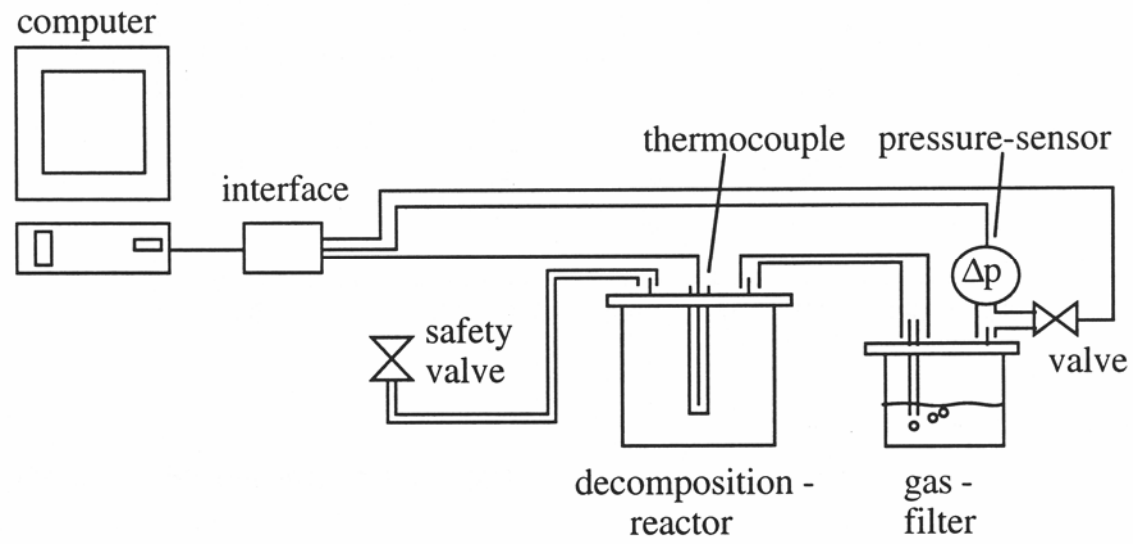

Figure 2.1: Instrument used to measure real time decomposition of H_2O_2.

thermocouple. To most accurately capture the onset of H_2O_2 decomposition, the H_2O and HCl were mixed first and allowed to come to temperature. If metal contamination effects were being studied, a known quantity of NIST standard solution of the desired metal was added to the diluted HCl solution via micropipette and allowed to equilibrate to the desired temperature as well. H_2O_2 was added to the preheated solution immediately prior to the vessel being sealed. In this manner, the effects of temperature, HCl concentration, and metal contamination on the decomposition rate of the H_2O_2 were all studied.

The real time decomposition analyzer, based on an O_2 partial pressure measurement, was calibrated by comparison with the standard iodometric H_2O_2 titration method.[8] This was accomplished during a decomposition test by opening the reaction vessel at predetermined times to remove an aliquot of solution for titration. This comparison was done twice. In the first case, at 80 °C, the aliquot was not thermally quenched but was allowed to gradually cool to room temperature before being titrated. In the second case, at 70 °C, the aliquot was immediately transferred from the reaction vessel to a vessel in an ice bath to rapidly quench the reaction and minimize errors caused by ongoing H_2O_2 decomposition during the time delay between aliquot extraction and titration. The results of both the decomposition analyzer and the titrations could then be plotted on a graph of time versus H_2O_2 concentration.

2.2.2 Results

Figure 2.2 shows the results of a comparison between real time measurements and titrations from periodic samplings using 1:1:5 ($HCl:H_2O_2:H_2O$) SC2 solutions. At 80 °C the titration technique gives much lower concentrations of H_2O_2 due to the fact that the aliquots were not thermally quenched prior to titration. When the aliquot to be titrated was quenched in an ice bath, the agreement between the two techniques is excellent as shown by the samples processed at 70 °C.

The normalized decomposition rates,

$$r_n = \frac{-dn/dt}{n_0} \qquad 2.3$$

(c.f. Section 1.4.3) of 1:1:5 SC2 solutions at 50 °C, 70 °C, and 80 °C are shown in Figure 2.3. The decomposition of H_2O_2 in SC2 is highly dependent on temperature. In Figure 2.4, the normalized decomposition rates shown have been translated into weight percent of H_2O_2 in the

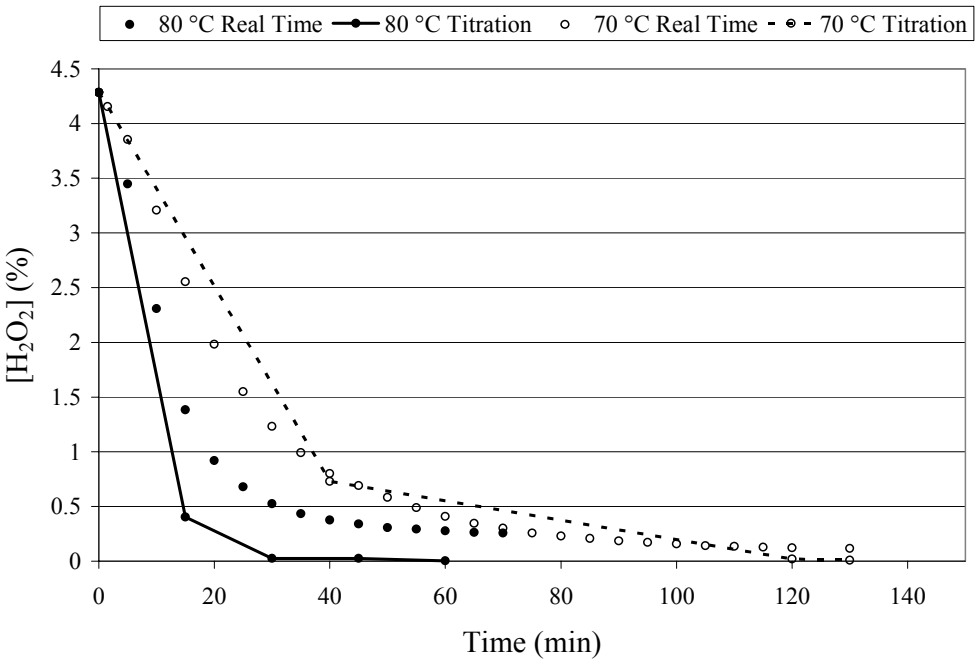

Figure 2.2: Comparison of weight percent H_2O_2 in a 1:1:5 SC2 at 70 °C and 80 °C over time as measured by titration and real time oxygen evolution techniques.

solution. These clearly demonstrate the rapid decline in H_2O_2 that can be expected in an SC2 bath at normal manufacturing conditions (i.e. 70 °C to 85 °C). An Arrhenius plot of the decomposition rates shown in Figures 2.3 and 2.4 is plotted in Figure 2.5, with a resulting activation energy of 106 kJ/mol being determined.

Knowing that metal contamination, even at levels of 1 ppb, is able to catalyze decomposition of H_2O_2 in SC1, tests were run to see the impact this might have on 1:1:5 SC2.[2] Solutions were spiked with an NIST standard solution of $Fe(NO_3)_3$ to levels of 1 and 100 ppb. The results of this are shown in Figure 2.6. Fe^{3+} does not cause a similar increase in decomposition rate, even at levels of 100 ppb. This lack of dependence on Fe^{3+} concentration is

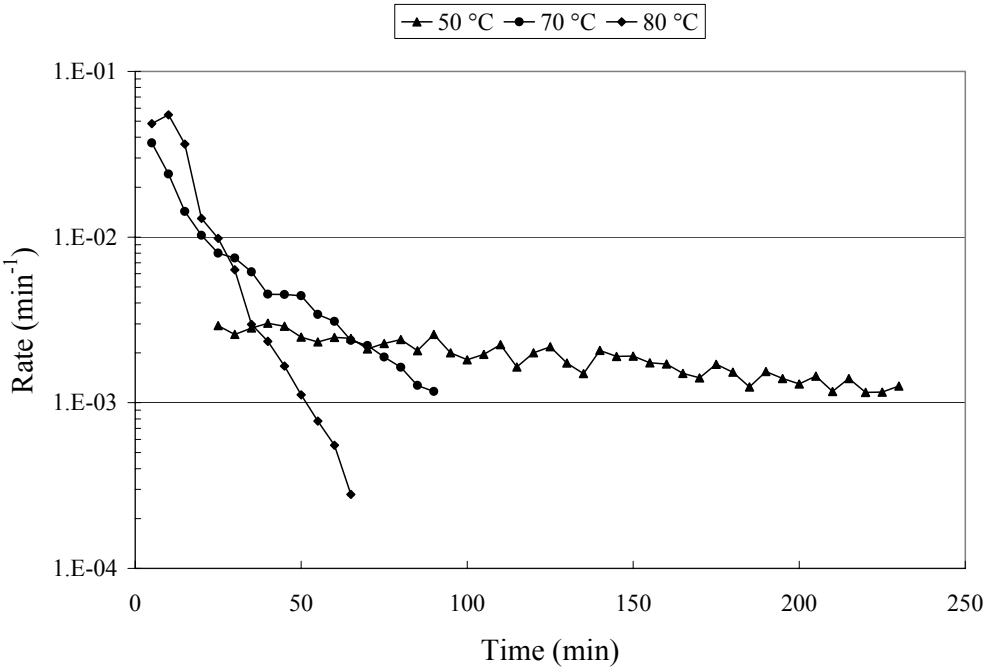

Figure 2.3: Normalized H_2O_2 decomposition rate in 1:1:5 SC2 at different temperatures.

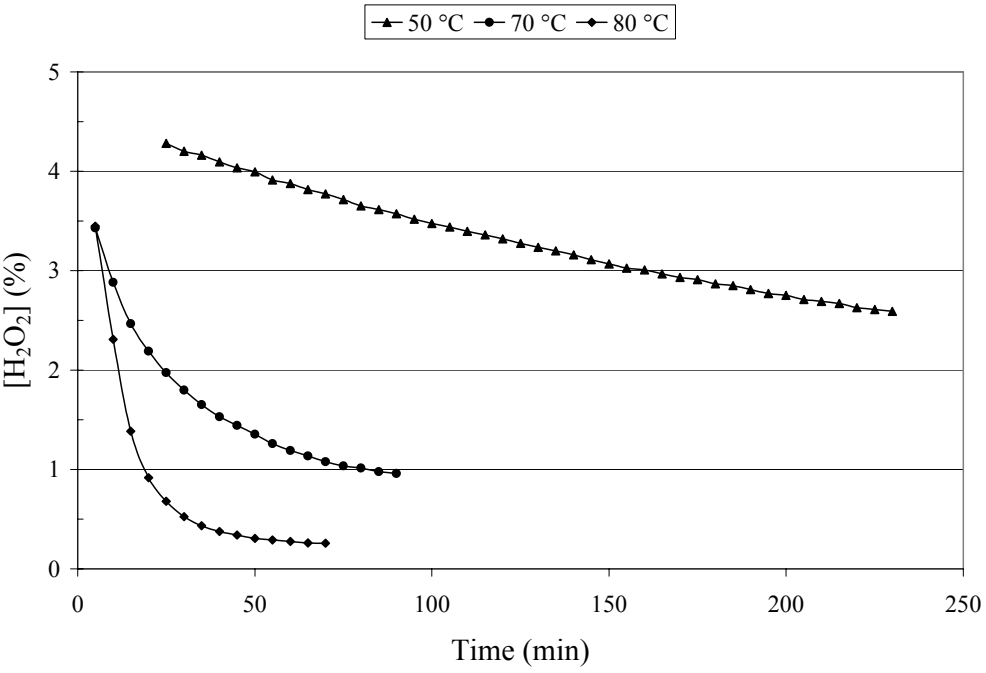

Figure 2.4: Weight percent of H_2O_2 over time in a 1:1:5 SC2 at different temperatures.

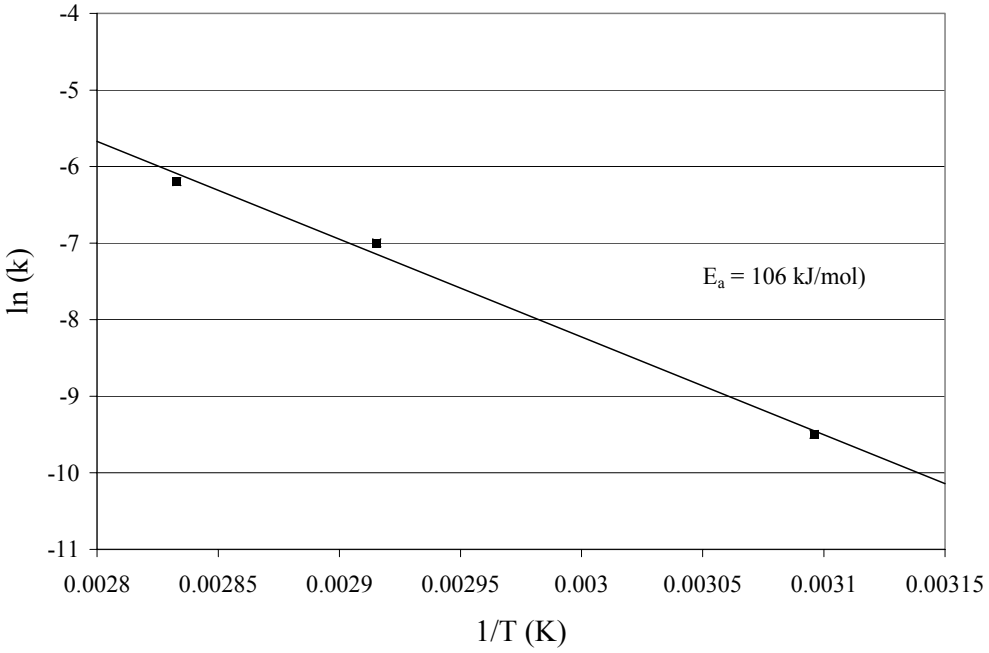

Figure 2.5: Ahrenius plot of data shown in Figures 2.3 and 2.4.

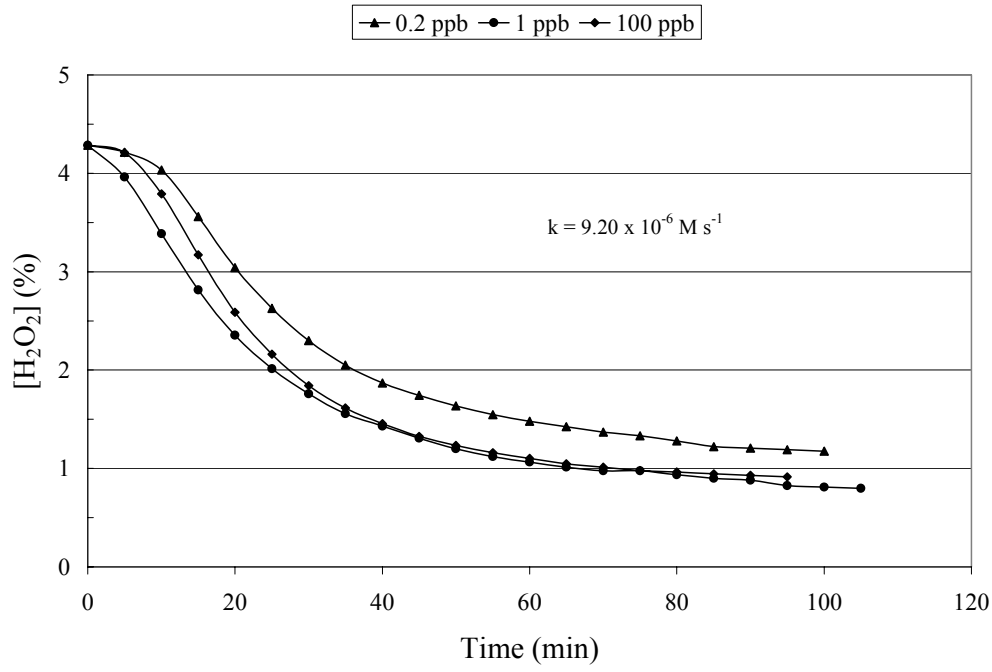

Figure 2.6: Effect of Fe contamination on H_2O_2 loss in a 1:1:5 SC2 at 70 °C. Decomposition rate is unaffected by Fe^{3+} in the mixture.

further demonstrated in Figure 2.7, where the results of a test run using 0.1:1:5.9 SC2 is shown. As noted in the Introduction, the proposed mechanisms for Fe catalyzed decomposition apparently are inhibited in an acidic environment. It is interesting to note that while Fe3+ is not catalyzing decomposition it is apparent that HCl is participating in the decomposition process as the rate constants caculated for one order of magnitude difference in [HCl] (Figures 2.6 and 2.7) are almost precisely two orders of magnitude different, indicating that the reaction is second order in [HCl] and permitting the following rate equation to be proposed:

$$r = k[H_2O_2][HCl]^2 \qquad 2.4$$

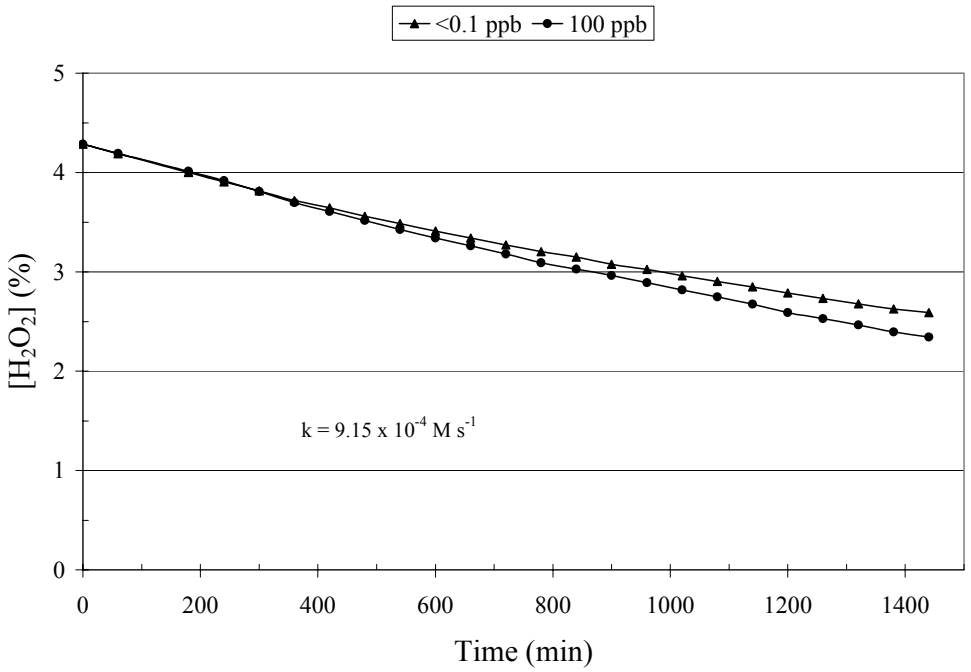

Figure 2.7: Loss of H_2O_2 in an SC2 solution with lower HCl concentration (0.1:1:5.9) at 70 °C and two levels of Fe^{3+} contamination. (Note as well that overall decomposition rate is greatly reduced relative to that shown in Figure 2.6.)

2.2.3 Conclusions

It has been demonstrated that in SC2 solutions, the H_2O_2 decomposition is extremely fast under typical wet bench processing conditions. Without continuous spiking, the H_2O_2 level diminishes to nearly zero in as little as thirty minutes at 80 °C. The rapid decomposition is primarily due to the high acidity and temperature. Fe^{3+} contamination has a negligible impact at the levels encountered in semiconductor grade chemicals and apparently is not able to catalyze H_2O_2 decomposition in acidic mixtures. HCl concentration has a strong impact on the decomposition rate though, and the lifetime of the H_2O_2 in the SC2 mixture can be greatly extended by reducing the HCl concentration. It is therefore interesting to determine what impact, if any, that reducing the HCl concentration will have on metal removal effectiveness.

2.3 Cleaning Efficiency of Dilute HCl

2.3.1 Experimental

To evaluate metal removal using more dilute HCl solutions, CZ, p-type, <100>, 1 to 30 Ω cm, Si wafers were intentionally contaminated with Fe, Zn, and Ca, via two methods: 1) using an SC1 made of lower purity chemicals, and 2) using an SC1 made of high purity chemicals that had been intentionally spiked with elevated quantities of the desired metals.[9,10] Fe, Zn, and Ca were deposited in the range of 10^{11} to 10^{12} at/cm^2.

After contamination, control wafers were set aside so that initial contamination levels could be quantified and compared to the test wafers that received different cleans. The first round of tests was a simple comparison of metal removal between a freshly mixed 1:1:5 SC2 and a 1:6 dilution of HCl in DI water. With the concentration of HCl being the same in both cases, it was possible to determine what impact the H_2O_2 was having on the metal removal effectiveness of the cleaning solution. Both cleans were performed at 70 °C for 10 minutes, after which the

wafers were rinsed in DI water and dried in a spin dryer. Unless otherwise stated, the cleaning was performed in a quartz bath with no recirculation or filtration. In subsequent tests, increasingly dilute solutions of HCl were tested at temperatures from 20 °C (RT) to 70 °C. All wafers were analyzed for metals using the VPD-DC-TXRF technique[11] (c.f. Section 1.2.3) on an Atomika XSA8010 TXRF using a W anode.

To evaluate the particle deposition behavior of static, dilute HCl solutions, 125 mm diameter wafers (with average initial particle levels of 50 particles >0.15 microns, 15 particles >0.2 microns, and 2 particles >0.4 microns per wafer) were processed for ten minutes in various dilutions of HCl at 20 °C (RT) and 70 °C and then spin dried. The solutions were analyzed with a liquid particle counter (Particle Measuring Systems CLS-700) and consistently had 40 - 60 particles per ml >0.5 microns. Particles were measured on the wafers before and after using the Censor ANS-100, (c.f. Section 1.2.4) a laser light scattering based wafer surface particle detector. Follow up tests evaluating the impact of bath dynamics were performed by processing wafers meeting the aforementioned cleanliness levels in a single pass overflow rinse bath that was continuously spiked with HCl to create the predetermined concentrations required.

2.3.2 Results – Metal Removal

Table 2.1 shows the range of initial levels for each of the metals used to intentionally contaminate Si wafers. Results comparing the cleaning ability of 1:1:5 SC2 and 1:6 HCl at 70 °C are shown in Table 2.2. For contamination on a SiO_2 surface, the H_2O_2 is unnecessary for

Metal	**10^{10} at/cm^2**
Fe	44-8 - 357
Zn	36.3 – 83.8
Ca	9.3 – 60.6

Table 2.1: Initial metal surface concentration on wafers used in cleaning experiments.

	Fe	Ca	Zn
Initial	357	9.3	36.3
Post (fresh) SC2	1.4	0.6	0.6
Post 1:6 HCl	1.1	1.2	1.3

Table 2.2: Comparison of SC2 and 1:6 HCl metal removal at 70 °C. All results in 10^{10} at/cm^2.

efficient removal of metals. This is consistent with the decomposition results shown in Section 2.1, since, at high temperature, the SC2 bath consists of well oxygenated 1:6 HCl after about 20 minutes.

The metal removal efficiencies of various dilutions of HCl at 20 °C and at 70 °C are shown in Figures 2.8a and 2.8b. At 20 °C, there is a noticeable loss in metal removal as the concentration of HCl is decreased, most notably for Fe. At 70 °C, metal removal efficiency remains high at all HCl concentrations tested. The high variation and low overall removal seen for Ca is believed to be the result of lower initial levels on the wafers.

Further investigation of dilute HCl metal removal capability was limited to Fe. Fe was chosen as the focus as its removal was more temperature dependent that either Zn or Ca (Figures 2.8a and 2.8b). Fe also has a lower detection limit by TXRF than Ca does and is not so readily picked up from cleanroom air with proper handling. Tests were performed to better understand the interplay of temperature, bath dynamics, HCl molarity and immersion time, as control parameters for optimizing metal removal.

The exact influence of solution temperature is demonstrated in Figure 2.9 which shows the Fe removal achieved with a 0.12 mM HCl solution at 20 °C, 50 °C, and 70 °C. Removal efficiency drops off between 20 °C and 50 °C, indicating a higher activation energy for Fe removal relative to the other metals studied.

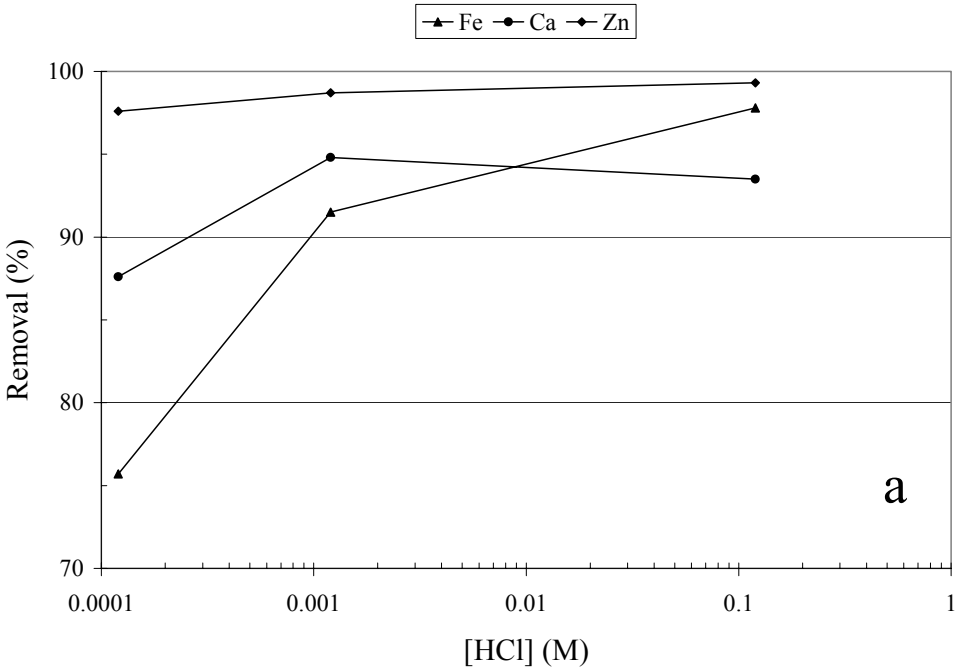

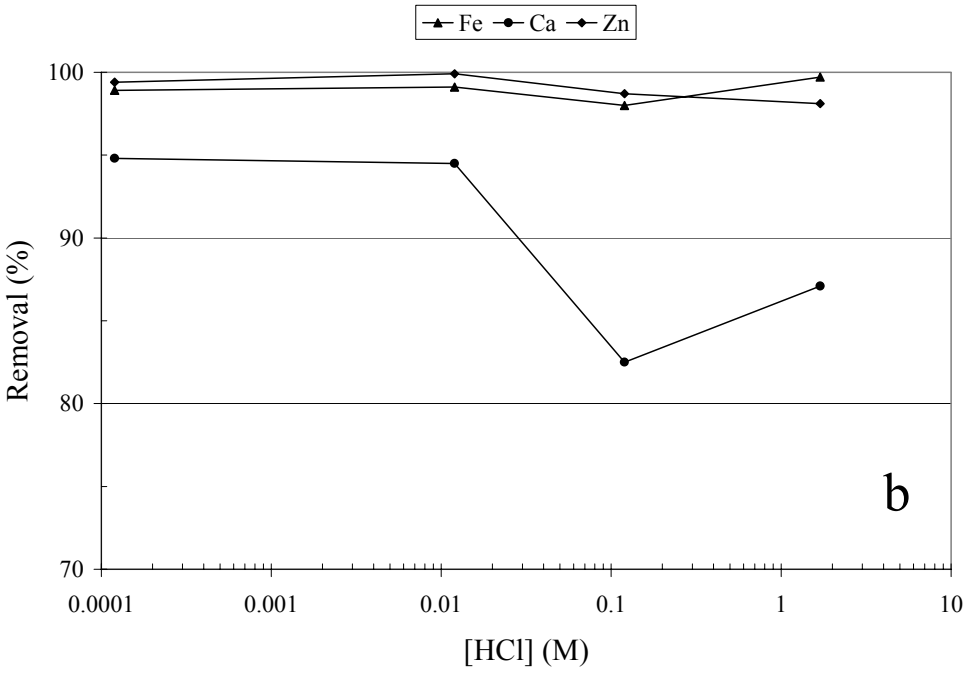

Figures 2.8a and 2.8b: Metal removal of dilute HCl solutions at 20 °C (a) and 70 °C (b).

Bath dynamics effects were tested by cleaning wafers in a continuous overflow rinse bath which was spiked with different levels of HCl. This ensured that fresh HCl solution was always in contact with the wafers, thus reducing the influence of diffusion and loading on the ultimate metal removal. A comparison of the efficiency of Fe removal across different HCl concentrations in both the rinse tank and in a static bath is shown in Figure 2.10. The metal removal not only follows the exact trend as in the static tank but is also very close in absolute value. The pH and temperature of the liquid solution are primarily responsible for the metal removal and bath loading is not an issue at these challenge levels. Fe removal over time in a 0.0012M solution in the rinse bath is shown in Figure 2.11. The maximum metal removal of this solution is reached in the first five minutes, following which, no measurable increase in metal removal is observed (the decline with time is believed to be due to analytical variability). The critical parameters to control are again shown to be the temperature and HCl concentration (pH).

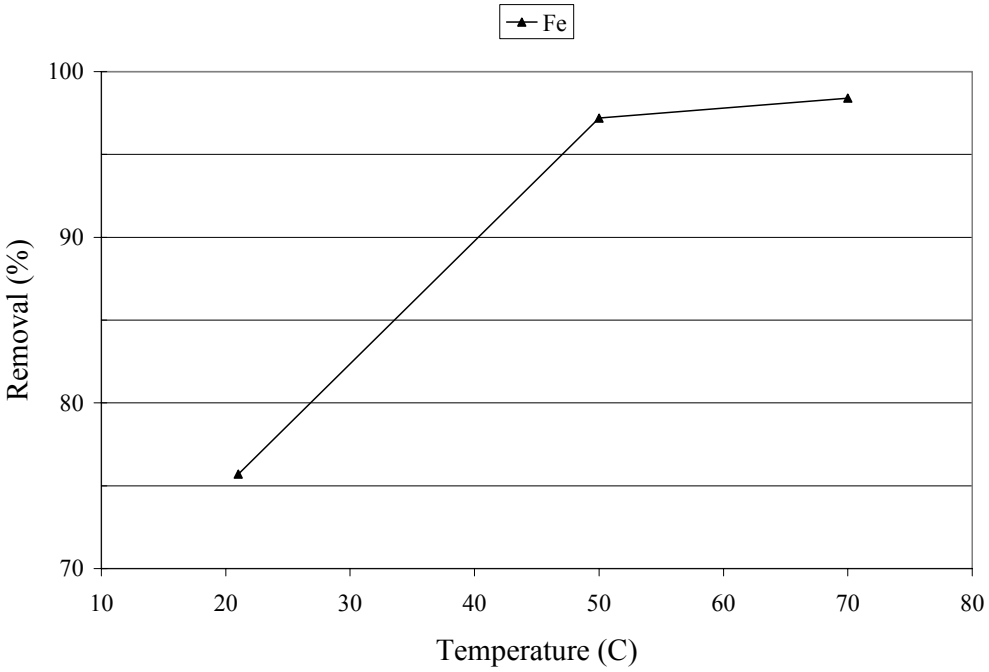

Figure 2.9: The effect of temperature on the metal removal efficiency of a 0.12 mM HCl.

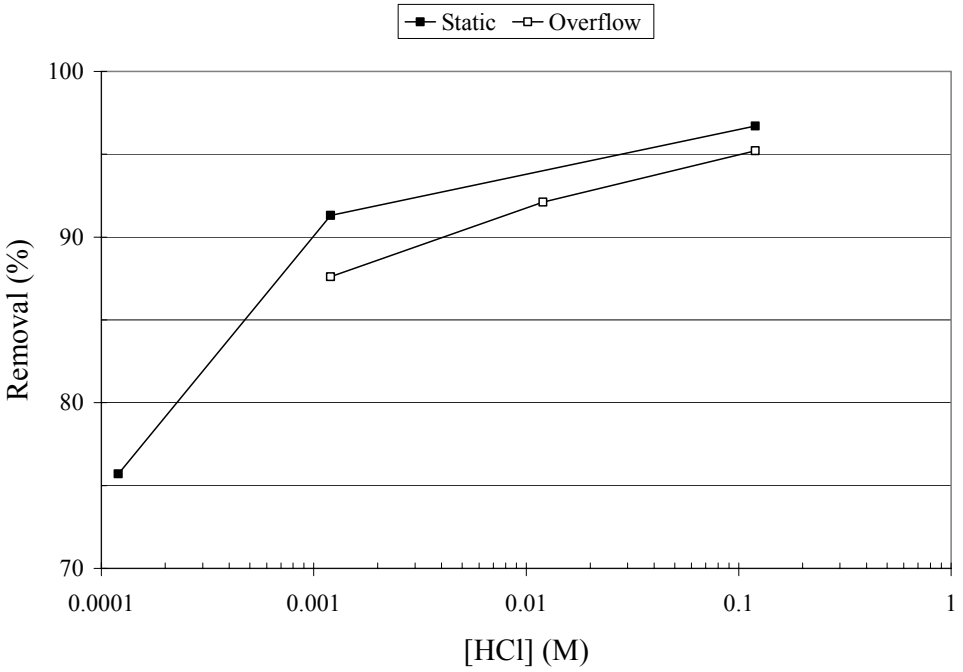

Figure 2.10: Fe removal as a function of bath dynamics.

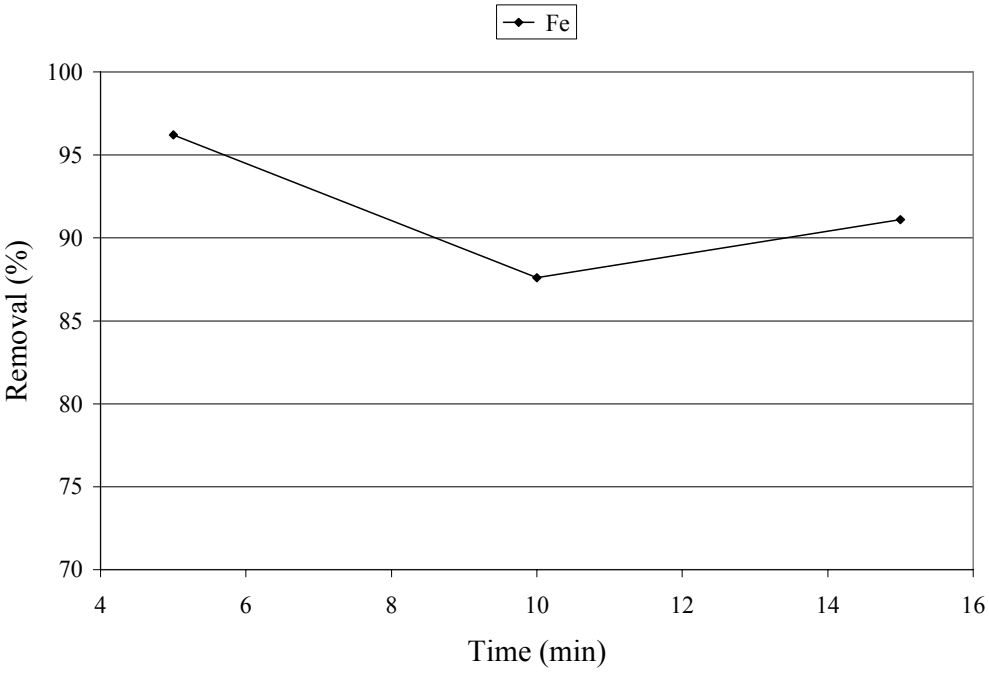

Figure 2.11: Fe removal as a function of time in 0.0012 M HCl.

2.3.3 Results – Particle Addition

Riley and Carbonell have shown that particle deposition onto silicon wafers is greatly reduced at pH values above 2-2.5.[12,13] This was explained by the fact that the isoelectric point for silicon and silicon dioxide is between pH 1.8 and 2.2.[12-15] At a pH above the isoelectric point, the wafer surface has a net negative charge, while below it, the wafer surface has a net positive charge. It has been reported that many of the particles in a liquid will be negatively charged as anions are usually more poorly hydrated than cations and so are more readily adsorbed onto the particle surface.[14] Therefore, at a pH above 2-2.5 an electrostatic repulsion barrier between the particles in the solution and the surface is formed. This barrier impedes particle deposition from the solution onto the wafer surface during immersion. Below pH 2, the wafer surface is positively charged, while many of the particles remain negatively charged, removing the repulsion barrier and resulting in particle deposition while the wafers are submerged. This is why it is commonly observed that a standard SC2 solution is particle "dirty". The pH of that solution is below 0 and so the wafers have a highly positive surface charge.

The practical implication for dilute HCl is that at concentrations higher than 0.01 M (~1:1000 dilution of 37% HCl), particle deposition should occur while the wafers are submerged, much as is the case with a standard SC2, while at concentrations below 0.01 M, particles will not deposit. Figures 2.12a and 2.12b show the results of the tests run in static baths, demonstrating that particle addition can be greatly reduced with these diluted acid cleans. In Figure 2.12b a sharp drop-off in particle addition between pH 2.0 to 2.5 can be seen, which is in agreement with the theoretical prediction of Riley and Carbonell.

Figure 2.13 shows the result obtained when processing wafers in an overflow rinse bath. Liquid particle levels were measured at each concentration of HCl. Prior to running the wafers,

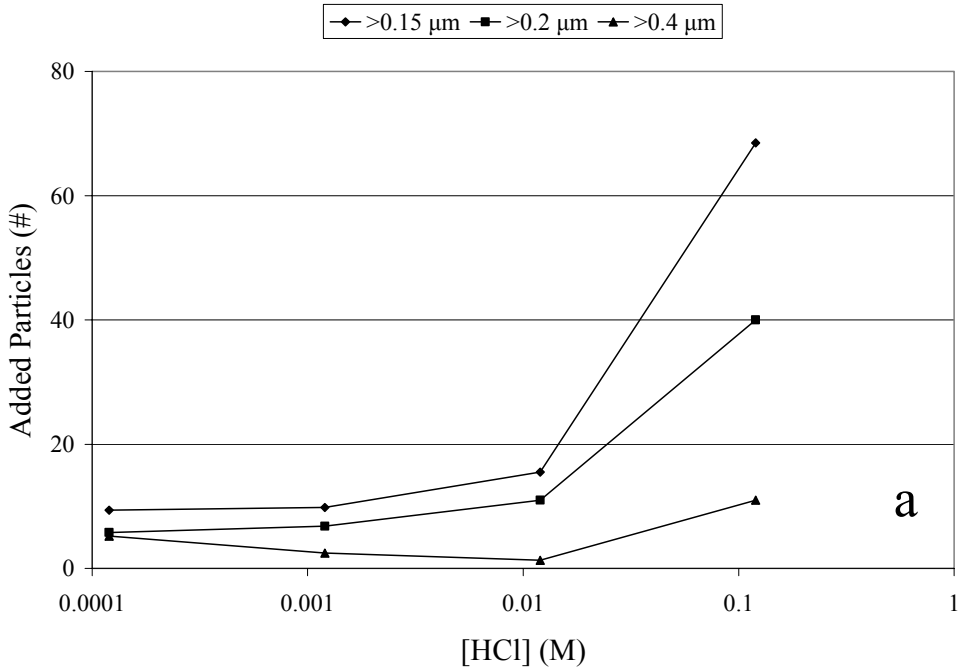

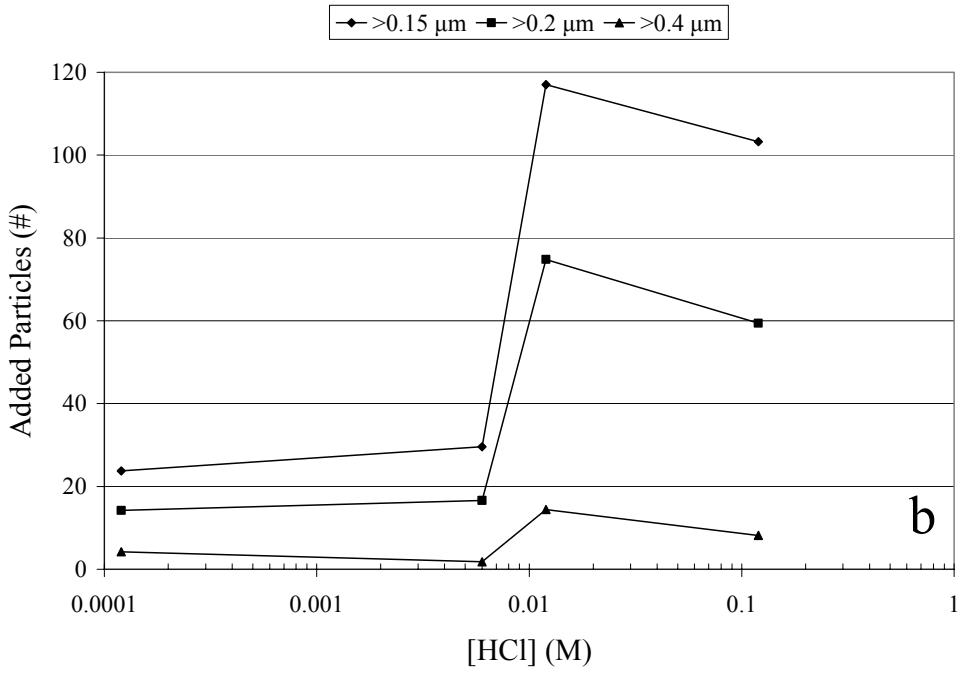

Figures 2.12a and 2.12b: Dilute HCl particle addition in 10 minutes at 20 °C (a) and 70 °C (b).

liquid particle levels were tested and at 0.01 M, the particle level in the overflow bath was approximately the same as in the static tank, while at 0.1 M it was 10X higher and at 0.001 M it was 10X lower. The difference in overflow bath liquid particle levels was primarily driven by particles introduced by the HCl injection pump. The results on the wafer surface as shown in Figure 2.13 clearly demonstrate that with a cleaner liquid the particle addition from HCl can be driven to zero by controlling the concentration.

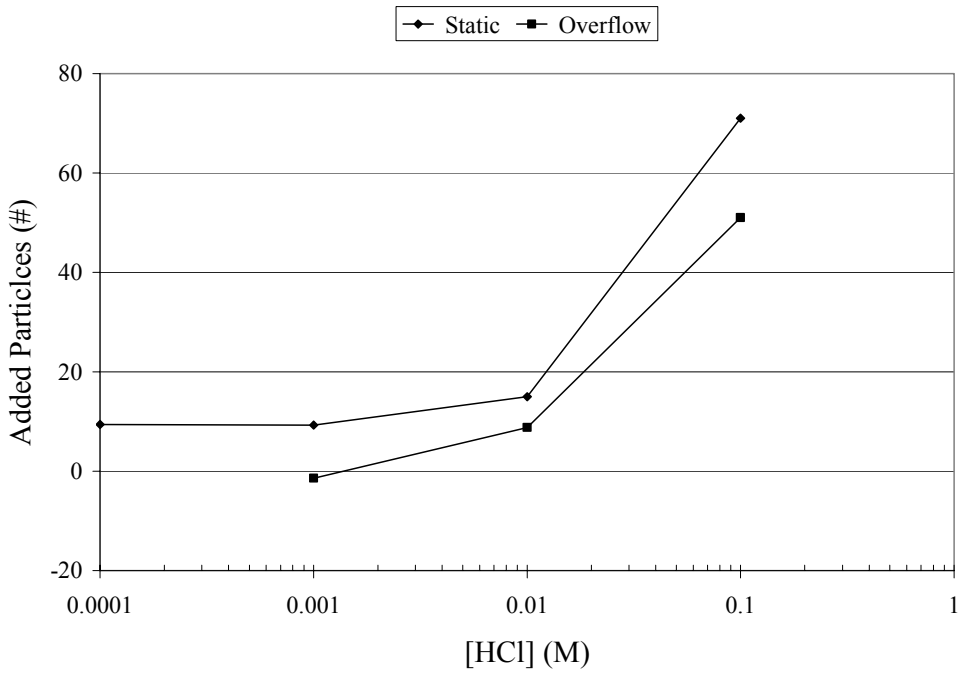

Figure 2.13: Effect of bath dynamics on particle deposition in dilute HCl solutions.

Figure 2.14 further demonstrates that there is no particle addition from the bulk liquid, as the length of time that the wafers were immersed in 0.0012 M HCl had no impact on how many particles were added or removed, again in agreement with Riley and Carbonell.

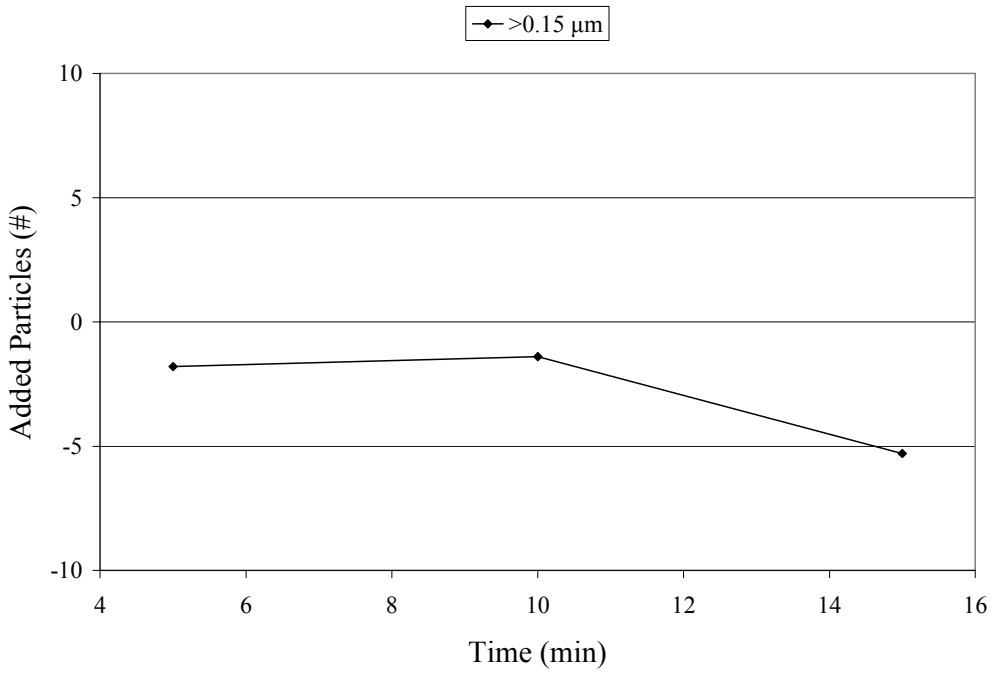

Figure 2.14: Particle deposition over time from 0.0012 M HCl.

2.3.4 Optimized Metal and Particle Cleaning

Optimizing the metal and particle performance of the dilute HCl cleans primarily requires controlling two parameters: temperature and pH (HCl concentration). Higher temperature and lower pH are expected to improve the metal removal and overall robustness of the solution while higher pH improves the particle behavior. In Figures 2.15a and 2.15b the process windows existing at 20 °C and 70 °C allowing for maximum metal removal and minimum particle addition can be seen. At 20 °C, metal removal is the limiting factor with metal removal dropping off quickly at concentrations below 0.0012 M. The optimum solutions lie between 0.012 and 0.0012 M HCl. While this is a good range for a process window (one order of magnitude) the situation can be improved dramatically by increasing the temperature. Figure 2.15b shows that metal removal is greatly improved by higher temperature, with no appreciable loss in metal

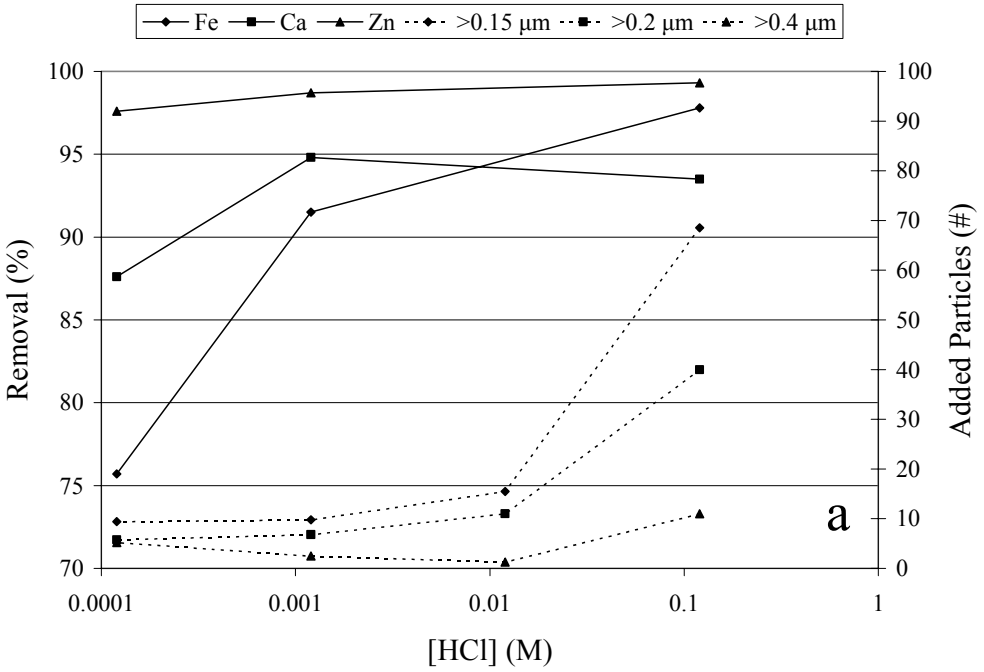

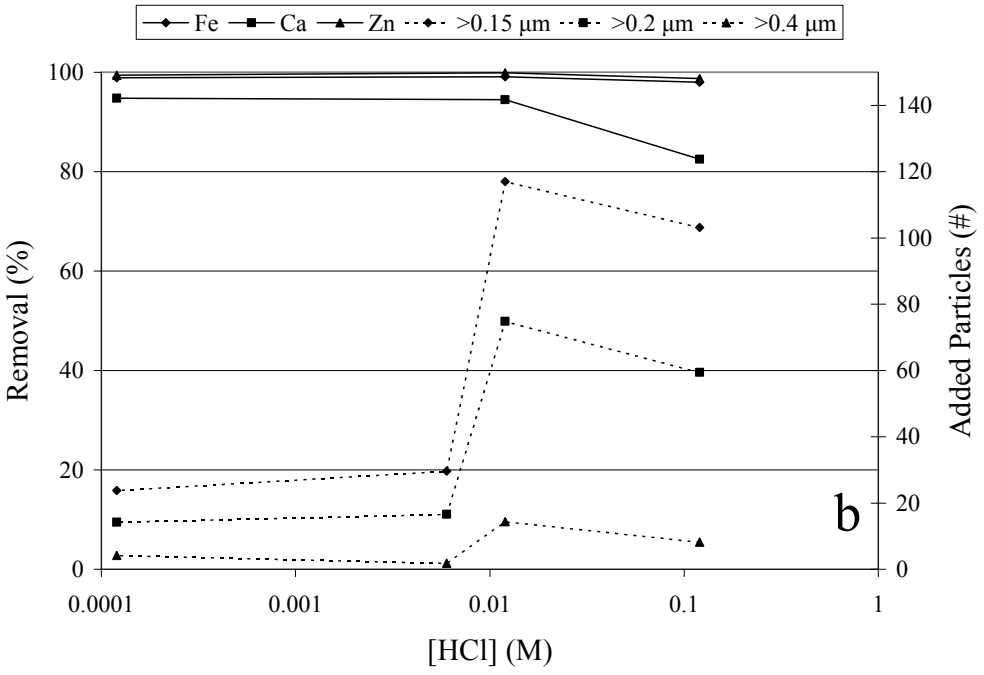

Figures 2.15a and 2.15b: Metal removal and particle addition behavior of dilute HCl at 20 °C (a) and 70 °C (b).

removal even at concentrations down to 0.0001 M. Figure 2.11 demonstrates that the immersion time could be as short as five minutes. This process should produce optimum metal removal and particle performance while still allowing one order of magnitude of variation in concentration and 10 °C to 20 °C variation in temperature for tuning to a particular process flow.

2.3.5 Conclusions

The lifetime of H_2O_2 is not of critical importance as dilute HCl will remove metals as effectively as SC2 with H_2O_2 present. With the cost of ultra pure chemicals rising it is important to maximize the efficiency of their use. Removing H_2O_2 from the SC2 clean as well as increasing the dilution of the HCl both result in significant cost savings to the fab.

While this work was performed in a bath, the results are equally applicable for spray tools. There is no issue of H_2O_2 decomposition in a spray tool as the chemicals are mixed during use and are not in contact with the wafers for very long. However, significant cost savings can be realized by reduction in the amount of HCl used and also by elimination of the H_2O_2 from this processing step.

Dilutions of HCl can be used to effectively remove oxidized metals from the surface of hydrophilic wafers. They also have some effectiveness at removing metallic Cu on the surface of hydrophobic wafers, no doubt being assisted by dissolved O_2 in the solution. By lowering the concentration below the critical threshold of 0.01 M, the metal removal process can be performed without paying the penalty of depositing particles. This particle behavior is in perfect agreement with theoretical models. An optimum temperature and concentration of 50 °C and 0.001 M is therefore proposed. This allows for one order of magnitude variation in concentration and 10 °C to 20 °C variation in temperature without serious degradation in the metal and particle

performance. The metal removal in these solutions reached its maximum in five minutes or less, allowing a faster total cleaning cycle time.

2.4 Reduction to Manufacturing Practice

2.4.1 Experimental

Having illuminated the chemical principles governing the SC2 process step and demonstrating that the mixture could be greatly simplified to dilutions of HCl excluding H_2O_2, the next step was to test the new clean in practice in a wafer fab. This was accomplished by evaluating a new pre-gate/furnace surface preparation sequence in a manufacturing research and development facility at Texas Instruments. The chosen sequence of chemicals for the clean was: 4.9% HF - 1:1:5 SC1 – 1:3400 dilute HCl (DHCl) with a DI rinse in between each chemical step and a spin rinse dry (SRD) at the end of the sequence. The DHCl clean used a 3400:1 (~0.0036 M) HCl solution at 55 °C. The DHCl clean sequence was tested versus the baseline cleaning sequence (Table 2.3) prior to gate oxide growth in a MOS capacitor manufacturing flow.

Sequence	Description
DHCl Pre-Gate Clean	4.9 % HF – 1:1:5 SC1 – 1:3400 Dilute HCl – Spin Rinse Dry
PFC	4.9 % HF – 1:1:5 SC1 – 1:1:5 SC2 – 1:1:5 SC1- Spin Rinse Dry

Table 2.3: Definitions of pre-gate clean sequences used.

After completion, the capacitors were electrically tested using the two common methods discussed in Section 1.2.5: 1) Q_{bd}, or charge to breakdown, in which a measured amount of charge is passed continuously through a gate oxide until it breaks down and begins passing charge freely and 2) E_{bd}, or voltage breakdown, in which voltage is ramped across the gate oxide

until it breaks down and begins passing charge freely. The total charge passed before breakdown is known as the Q_{bd} and the voltage at which the gate breaks down is known as the E_{bd}. Results of both types of testing were compared between the two cleaning sequences. Testing on both PMOS (B doped substrate) and NMOS (P doped substrate) was carried out with the capacitor in accumulation (i.e. negative bias for PMOS and positive bias for NMOS) in both cases.

2.4.2 Gate Oxide Integrity Electrical Results

As shown in the data summary in Table 2.4 as well as in Figures 2.16 and 2.17 there is no statistically significant difference in Q_{bd} between the two pre-gate cleans. The N/+ data in Table 2.4 do not include the tail of the distributions (below 14 C/cm^2). Capacitor area for this test was 0.05 cm^2, and about 1400 capacitors were probed in accumulation for each split (~280 on each of five wafers) with a substrate injection of 100 mA/cm^2. The N/+ wafers showed excellent distributions for both PFC and DCHl cleans, with the DCHl split having a slightly higher average. The primary failure distribution for the DCHl split had a lower standard deviation than the PFC split. Both sets of wafers showed about 20% failure in the reliability region (3-8 MV/cm). The distribution of failures in this lower region was identical for both cleans.

Sequence	Q_{bd} (C/cm^2)	
	N/+	P/-
DHCl	32.2 $\pm$ 10	1.95 $\pm$ 1.0
PFC	38.5 $\pm$ 11	2.27 $\pm$ 1.0

Table 2.4: Q_{bd} Distribution as a function of Pre-Clean

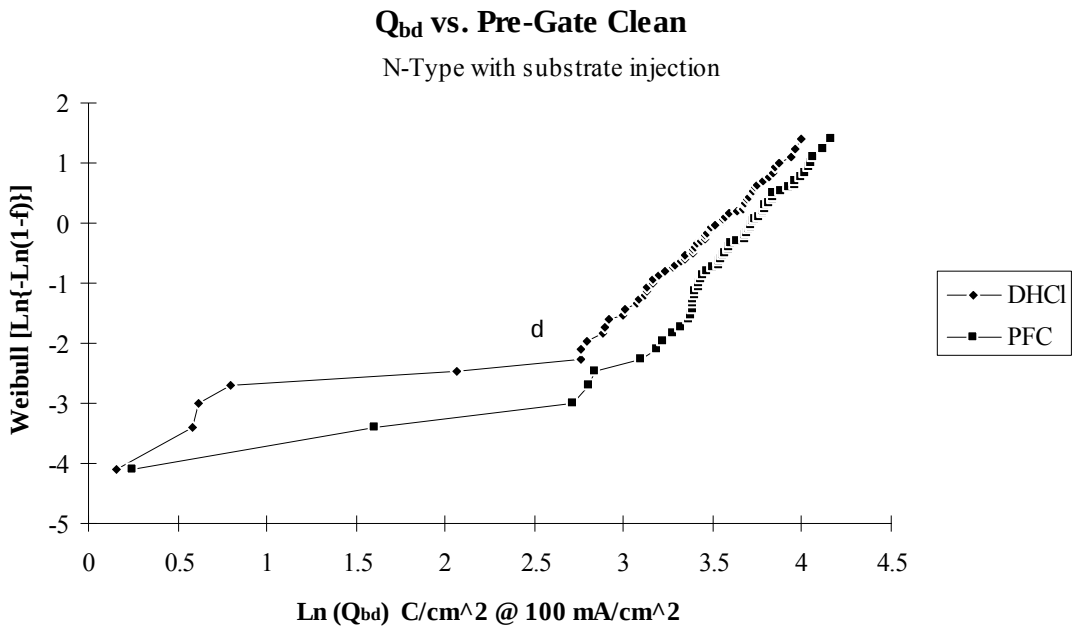

Figure 2.16: Weibull distribution of charge-to-breakdown (Q_{bd}) as measured on ten sites/wafer for three wafers each for DHCl and PFC cleaning splits.

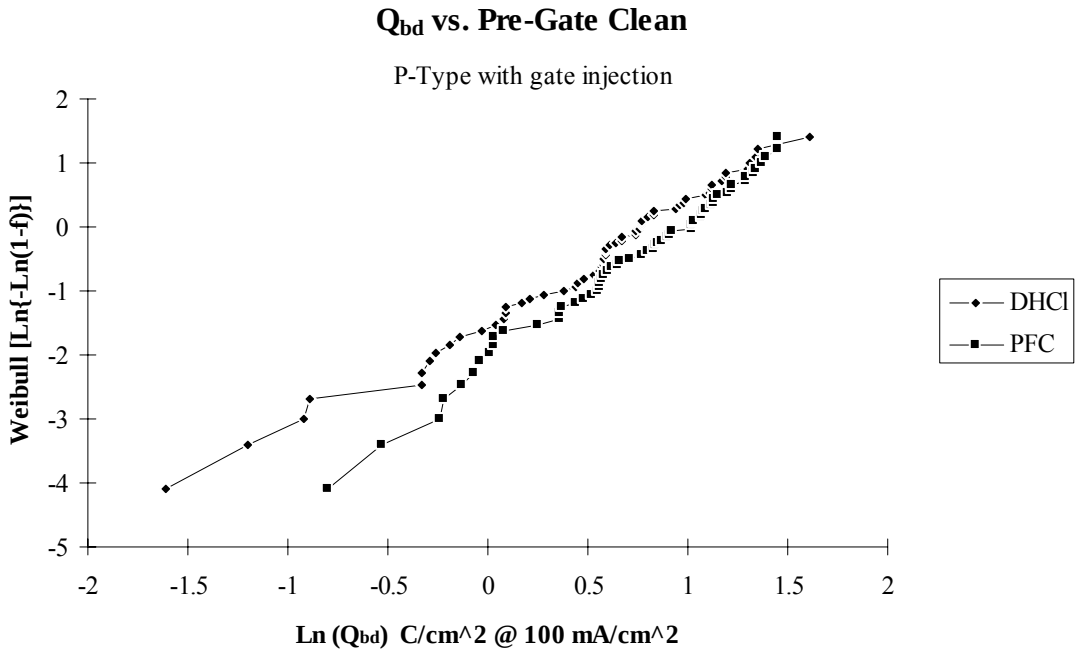

Figure 2.17: Weibull distribution of charge to breakdown (Q_{bd}) as measured on ten sites/wafer for three wafers each for DHCl and PFC cleaning splits.

Overall the DHCl process showed superior V_{bd} performance as well for both N/+ and P/- wafers. The data are summarized in Table 2.5 while the histograms and probability distributions are given in Figures 2.18-2.21. V_{bd} was measured on 1400 sites/wafer for five wafers each for DHCl and PFC cleaning splits. All wafers were probed in accumulation. Results for N/+ wafers are depicted in Figure 2.18. About 85% of both sets fall into the 10.6 MV/cm bin. 15.5% of the DHCl distribution falls into the 11.1 MV/cm bin, while 16.5% of the PFC distribution falls into the 10.0 bin. Figure 2.19 shows the probability distribution for the results in Figure 2.18. Near the peak of the distribution the slopes of the 2 lines are almost identical, but the median value of the DHCl distribution is about 0.2 MV/cm higher showing it is slightly better than the baseline clean. Figure 2.20 shows the Vbd distribution for the P/- wafers. The averages of the two primary distributions (near 10 MV/cm) are similar, but the standard deviation of the DHCl distribution is almost half that of the PFC data. Figure 2.21 shows the probability distribution for the P/- wafers. While the median values are similar, the DHCl slope is lower.

Sequence	V_{bd} (MV/cm)	
	N/+	P/-
DHCl	11.0 + 0.57	10.9 + 0.29
PFC	10.8 + 0.71	10.8 + 0.48

Table 2.5: Breakdown voltage distribution as a function of pre-clean.

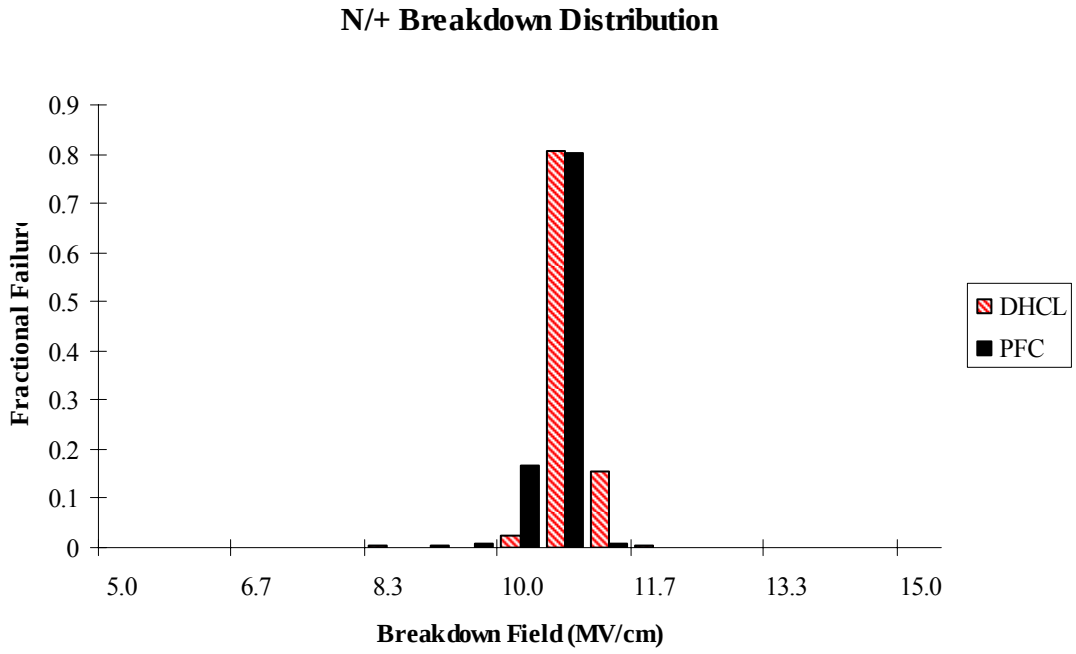

Figure 2.18: Voltage to breakdown (V_{bd}) measured on N/+ wafers.

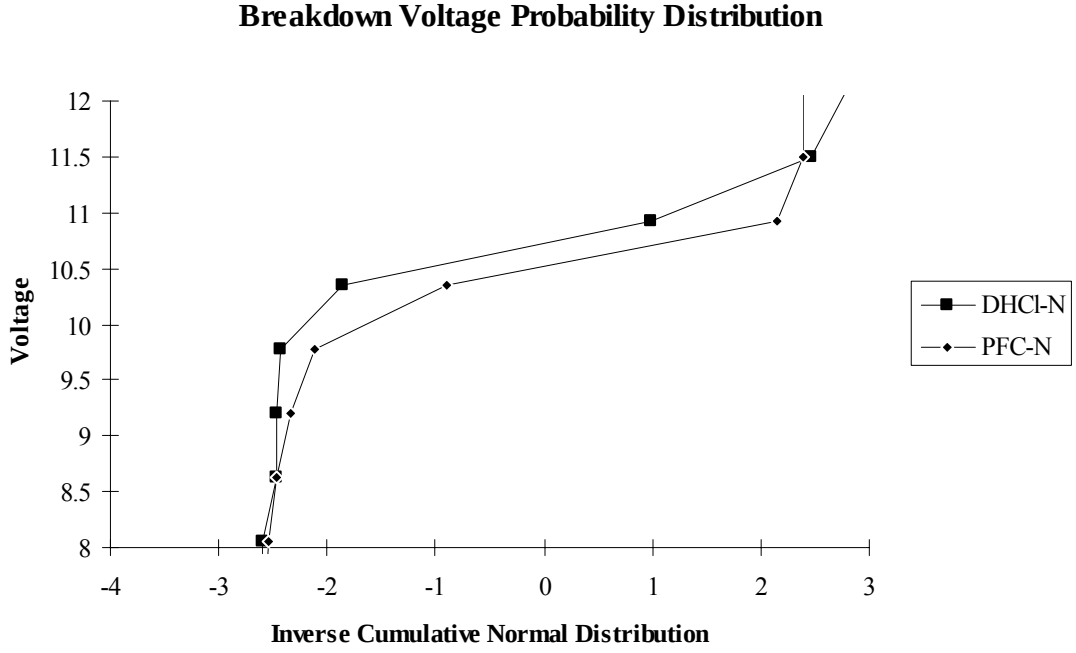

Figure 2.19: Probability distribution of the data in Figure 2.18.

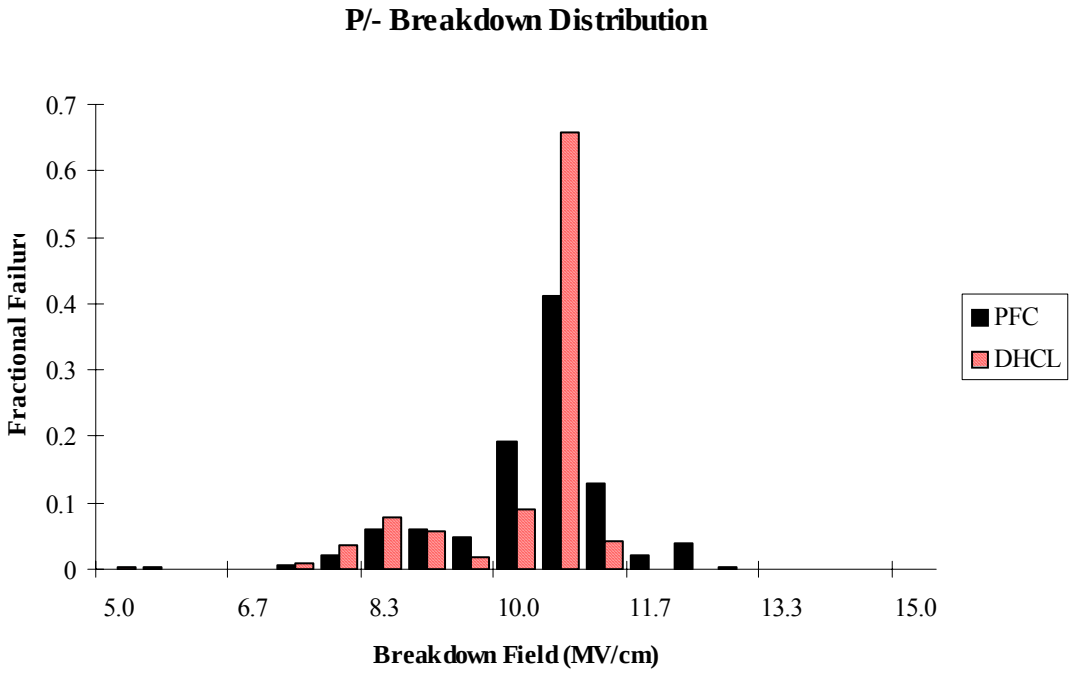

Figure 2.20: Voltage to breakdown (Vbd) as measured on P/- wafers.

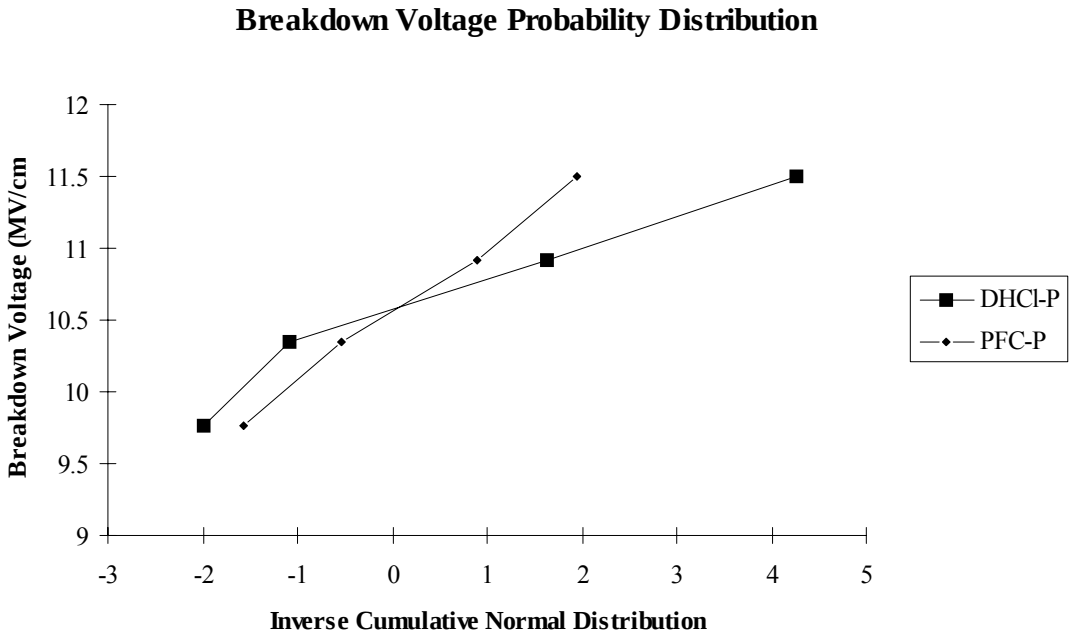

Figure 2.21: Probability distribution of the data in Figure 2.21.

2.3.3 Conclusions

The dilute HCl pre-gate/furnace clean sequence (HF-SC1-DHCl) was proven to be viable in a manufacturing environment. The process resulted in slightly superior gate oxide integrity (GOI) as measured by E_{bd} while Q_{bd} was unchanged versus the baseline sequence (HF-SC1-SC2-SC1). Chemical usage is greatly reduced due to the sequence being shorter and lower concentration of HCl being used. The process has subsequently been implemented in processing for multiple technology nodes at Texas Instruments.

2.4 General Conclusions

In this chapter, a specific cleaning chemistry, the SC2 clean, was investigated from a fundamental chemical standpoint. It was found that the standard processing conditions and mixing ratios made very inefficient usage of the chemicals. With an activation energy or 106 kJ/mol and a reaction rate that is 2^{nd} order in [HCl], it was demonstrated that the low pH and high temperature generally employed in manufacturing cause rapid decomposition of the H_2O_2, indicating that H_2O_2 could be eliminated entirely. It was clearly demonstrated that H_2O_2 decomposition by metallic contamination, which has been shown to be a significant concern for the basic SC1 mixture, does not occur in the acidic environment of the SC2 chemistry, likely due to the low pH interfering with specific reactions in either of the currently proposed mechanisms.

Follow up testing demonstrated that metal removal could be accomplished with significantly less HCl (>2 orders of magnitude less) especially if higher temperatures were used. A beneficial side effect of reducing the HCl concentration was found to be a significant reduction in particle deposition once the pH was increased to >2.5. This was found to be a consequence of moving the pH above the isoelectronic point of SiO_2 resulting in the surface

being negatively charged and therefore unattractive to particles in solution which are predominantly negatively charged. Application of the chemical knowledge gained led to testing in a manufacturing flow where DCHl was found to give equivalent to superior electrical results when compared to baseline cleans that used much more concentrated chemistries.

2.5 References

(1) Kern, W.; Puotinen, D.A. *RCA Review* **1970** *31* 187.

(2) Schmidt, H.F.; Meuris, M.; Mertens, P.W.; Rotondaro, A.L.P.; Heyns, M.M.; Hurd, T.Q.; Hatcher, Z. *Jpn. J. Appl. Phys.* **1995** *34* 727.

(3) Walling, C. and Cleary, M. *Int. J. Chem. Kin.* **1977** *IX* 595.

(4) Kremer, M. *Int. J. Chem. Kin.* **1985** *17* 1299.

(5) Barb, W.G.; Baxendale, J.H.; George,P.; Hargrave, K.R. *Trans. Faraday Soc.* **1951** *47* 591.

(6) Kremer, M. *Trans. Faraday Soc.* **1962** *58* 702; **1963** *59* 2535.

(7) Schmidt, H.F.; Mertens, P.W.; Meuris, M.; Verhaverbeke, S.; Heyns, M.M.; Kubota, M.; Dillenbeck, K. *IES 39th Annual Technical Meeting 1993 Proceedings Vol. I;* IES: Mount Prospect Illinois, 1993; p 238.

(8) Laitinen, H.A. *Chemical Analysis;* McGraw Hill: NY, 1960; p 411.

(9) Meuris, M.; Heyns, M.; Kuper, W.; Verhaverbeke, S.; Philipossian, A. *ECS Proceedings 91-11: ULSI Science and Technology 1991;* ECS: Pennington NJ, 1991.

(10) Schmidt, H.F.; Mertens, P.W.; Meuris, M.; Verhaverbeke, S.; Heyns, M.; Dillenbeck, K.; *Proceedings of UCPSS 1992*; IMEC Press: Leuven Belgium.

(11) Neumann, C. and Eichinger, P. *Spectrochemica Acta*, **1991** *46B* No.10 1369.

(12) Riley, D.J. and Carbonell, R.G. *J. of Coll. and Interface Sci.***1991** *158* 259.

(13) Riley, D.J. and Carbonell, R.G. *J. of Coll. and Interface Sci*. **1991** *158* 274.

(13) Lee, J-K; Liu, B.Y.H.; Rubow, K.L. *IES 39th Annual Technical Meeting 1993 Proceedings Vol.1;* IES: Mount Prospect, Illinois, 1993; p 209.

(14) Parks, G. *Chem. Rev*. **1965** *65* 177.

CHAPTER 3

METAL ION ADSORPTION ONTO SILICON OXIDE SURFACES

3.1 Introduction

In order to make improvements in cleaning and to meet the challenges of future generations of devices it is necessary to understand the chemistry of contaminant metal ions both in solution as well as on the surface of the wafer. In Chapter 2, the conclusion was reached that metals can be readily removed from silicon oxide (silica) surfaces even when using extremely dilute acid solutions. It has also been observed that different metals will adsorb to the silicon oxide surface with widely varying degrees of efficiency.[1-5] It would be very useful then to be able to accurately predict which metals would be most likely to adsorb on silicon oxide surfaces and which would be most difficult to remove, especially (as discussed in Chapter 1) as the semiconductor industry continues to utilize an ever growing number of metals with each successive technology node that is developed. To date, various approaches to understanding and predicting adsorption of metals onto oxidized silicon wafers have been put forward, with varying degrees of success, including ones based on electrochemical thermodynamics (ie Pourbaix diagrams), solubility/precipitation, adsorption/desorption kinetics, equilibrium thermodynamics, and Langmuir film deposition.[6-10] All of these give empirical descriptions of the adsorption phenomena but do not provide much predictive ability. In this chapter, the chemical phenomena that control metal adsorption on silica surfaces will be discussed, resulting in the proposal of a simple, qualitative approach to determining the affinity of a given metal in solution for the silicon oxide surface. The strength of this approach lies in the fact that it relates well studied behaviors of metals in solution to their behavior at the oxide surface of silica gel.

3.1.1 Metal Ions in Solution

When a metal ion is placed in aqueous solution it will stabilize its positive charge by surrounding itself with a hydration sphere of water molecules, usually six in total. If other chemical species (ligands) are present in the solution, especially Lewis bases, the metal can preferentially coordinate with the ligands (until thermodynamic equilibrium is obtained) thereby displacing the H_2O coordinated to the metal, as shown:

$$M(H_2O)^{6x+} + yL^- \rightarrow ML_y(H_2O)_{6-y}{}^{(x-y)+} \quad 3.1$$

Ignoring the hydration sheath, as ligands are added, stepwise formation constants can be calculated from the equilibrium concentrations,

$$K_1 = \frac{[ML]}{[M][L]} \quad 3.2$$

$$K_2 = \frac{[ML_2]}{[ML][L]} \quad 3.3$$

$$K_3 = \frac{[ML_3]}{[ML_2][L]} \quad 3.4$$

(p, T, I = constant) where p = pressure, T = temperature, and I = solution ionic strength. For K_x where $x>1$, it is customary to use β_x, overall formation constants, instead of K_x for the formation constants to simplify analysis and calculations, e.g.,

$$\beta_2 = \frac{[ML_2]}{[M][L]^2} \quad 3.5$$

$$\beta_3 = \frac{[ML_3]}{[M][L]^3} \quad 3.6$$

A quick analysis will show that $\beta_2 = K_1K_2$ and $\beta_3=K_1K_2K_3$.[11] Ligands can be monodentate (one reactive site per ligand) or, in the case of chelating agents, polydentate (multiple reactive sites per ligand).

A special case of the above occurs during the process of hydrolysis, in which a proton is ejected from a metal's surrounding water sheath, acidifying the water and creating a Lewis base (OH^-) that coordinates with the metal as shown:

$$M(H_2O)_6^{x+} \rightarrow M(OH)_y(H_2O)_{6-y}^{(x-y)+} + yH^+ \qquad 3.7$$

This speciation process will repeat until the metal achieves thermodynamic equilibrium. The equilibrium condition of this reaction can be characterized by a hydrolysis constant, defined as,

$$K_{hy} = \frac{[H^+]^y[M(OH)y(H_2O)_{6-y}^{x-y+}]}{[M(H_2O)_6^{x+}]} \text{ (p,T,I = constant)} \qquad 3.8$$

The sequential ejection of protons can be characterized and the stepwise equilibrium constant assigned a subscript that denotes how many protons have been ejected (ie K_{h1}, β_{h2}, β_{h3}, etc…). The hydrolysis process has been well characterized for many metals and reliable tables of overall stability constants can be located in the literature.[12,13] These constants make it possible to calculate the anticipated hydrolytic speciation of a given metal over a wide pH range.

In the case of some metals, especially those with high oxidation states, as pH increases, one or more hydroxyl groups coordinated with the metal will lose their remaining proton, resulting in the formation of a metal oxide (e.g. chromate ion, manganate ion):

$$Cr^{6+} + 4H_2O \rightarrow H_2CrO_4 + 6H^+ \qquad 3.9$$

Depending on pH, this can result in the formation of polynuclear species having oxygen bridges between the metal ions.[14,15]

$$2HCrO_4^- \leftrightarrow Cr_2O_7^{2-} + H_2O \qquad 3.10$$

In the case of some metals, iron being an example, the metal can go from free ion (Fe^{3+}) to hydroxide ($Fe(OH)_3$) to oxide ($FeO(OH)$) and back to hydroxide ($Fe(OH)_4^-$) as pH is increased. Where a metal is in this cycle will certainly impact how well it is able to react with the silica

surface. For the metals and pH ranges studied in this dissertation, this phenomena does not play a major role but it is definitely one to be aware of in making practical application of the conclusions of this work, especially in the case of metals like Zr, Hf, and Ti.

Finally, the coordination sphere surrounding a metal in chemical solution is not static. The ligands attached to the metal are continually exchanging both with ligands in the surrounding solvent, and with the solvent itself in most cases. The rate of this process is determined primarily by the metal, with the ligand and solvent playing minor roles in the majority of cases. In the simplest case of a hydrolyzed metal exchanging with water molecules in its coordination sphere, the rate of this exchange can span up to 16 orders of magnitude between, for example, Cu^{2+} which exchanges on the nanosecond timescale and Ru^{3+} which exchanges on the order of once per day.[15] While this particular phenomenon is not explored in great detail in this dissertation, and indeed, does not play a major role in the results discussed as all metals investigated exchange in the <<1 second regime, it is included as a note for potential further study in the context of semiconductor manufacturing.

3.1.2 The Silicon Oxide (Silica) Surface

It is known that organic and inorganic acids will adsorb on silica gel surfaces. Various authors have successfully used complexation and ligand exchange to describe the observed absorption.[16-22] Stability constants have been determined for several different oxide surfaces, including silica, titania, ferria, and alumina.[16,17,23] The precise nature of the bonding between the surface and the adsorbing species is still an active area of debate. Work with organic acids has shown that the reactions at the surface can be inner sphere in nature, i.e. reaction occuring via a bridging ligand, but this has not been shown decisively in the case of metals.[16,19] It has been proposed by some that the published data support the conclusion that metals bonding to oxide

surfaces do so via an outer sphere mechanism wherein the metal retains its complete hydration sheath of water/hydroxyl molecules.[19] Successful models have been proposed based on the assumption of both inner and outer sphere mechanisms.[17,21] In the case of metals there are many difficulties associated with determining the exact mechanism controlling metal adsorption at the surface of silica. This is due to the fact that several phenomena, adsorption, hydrolysis and precipitation, converge in a very narrow pH range making it difficult, if not impossible to separate them (contributing to the multitude of proposed mechanisms in the literature for metal adsorprtion on the surfaces of oxidized silicon wafers). This does not mean, however, that useful patterns cannot be found based on metal and silica reactivity.

The surface of silicon and metal oxides are covered by hydroxyl groups when in contact with aqueous solutions. These hydroxyl groups are able to pick up and release protons from solution resulting in the observed pH dependence of the surface charge. Silica has weakly acidic hydroxyl groups on the surface as is evidenced by a point of zero charge (pzc) at pH ~2 and an estimated K_a of $10^{-6.8}$. Thus the surface can act as an ion exchange or coordination site for both water and ions present in the solution.[16,17,22,24]

When describing metal adsorption on the silica surface, an approach similar to that used to describe metal interactions with water molecules can be used with great success. The reaction of a metal at the surface can be described as follows:[17]

$$\equiv SiOH + M^{x+} \rightarrow \equiv SiOM^{(x-1)^+} + H^+ \qquad 3.11$$

$$2 \equiv SiOH + M^{x+} \rightarrow (\equiv SiO)_2 M^{(x-2)+} + 2H^+ \qquad 3.12$$

Formation constants for the surface complexes formed on the silca surface can therefore be defined as follows:

$$K_{s1} = \frac{\{\equiv SiOM^{(x-1)+}\}[H^+]}{\{SiOH\}[M^{x+}]} \quad 3.13$$

$$\beta_{s2} = \frac{\{(\equiv SiO)_2 M^{(x-2)+}\}[H^+]^2}{\{\equiv SiOH\}^2[M^{x+}]} \quad 3.14$$

p,T,I = constant, {} indicates a surface concentration, [] indicates a solution concentration.

The silanol groups (≡Si-$(OH)_x$ (x=1,2)) covering the silica surface were reported long ago to behave as weakly acidic ion exchangers.[22] The protons bound to the oxygen atoms are readily displaced by other positive ions (e.g. metal cations). The displacement of a proton from a silanol on a silica surface by a metal ion is very similar to the displacement of a proton from a water molecule by a metal ion. In both cases, a metal ion is reacting with an X-OH molecule (X = Si or H) with a resulting displacement of a proton. While, at a given pH, displacement of a proton from a silica surface is energetically favored over displacement of a proton from a water molecule, it has been noted that, for a given metal, the energetics of the two reactions are proportional to one another.[17,22,25] Simply put, the tendency of a metal ion in solution to react with water is proportional to the tendency of that metal ion to react with silanol, i.e. the more readily hydrolyzable a metal is (with correspondingly larger K_{h1}) the more readily it should react with the silica surface (with correspondingly larger K_{s1}). Metal ions with high charge/radius ratios will hydrolyze to a greater extent than those with smaller ratios, leading to the correlation between the ratio of metal charge/ionic radius and adorption on silica that has been previously observed.[10,26] The correlation between K_h and K_s has been reported for silica gel in the past and it was demonstrated by Schindler (at I = 1), that the two types of stability constants could be linearly fit by the equation (having a least square mean fit = 0.99):[17,24]

$$\log K_{s1}K_{s2} = -0.09 + 0.62 \log K_{h1}K_{h2} \quad 3.15$$

Thus, an inspection of hydrolysis constants for metals should give an immediate indication of how thermodynamically favorable its adsorption is relative to other given metals, assuming only H_2O is present. Since it is currently impossible to quantify {SiOM} and {SiO_2M} and determine if the surface metals in this study are attached to one silanol or two on the surface of the wafer, and given that some of the metals tested do not form a second hydrolysis product (e.g Ca) it is useful to re-plot the first formation constants, K_{s1} versus the first hydrolysis constant K_{h1}, (which gives an equation with a least square mean fit = 0.98):

$$\log K_{s1} = -0.39 + 0.58 \log K_{h1} \qquad 3.16$$

The results of this calculation are shown in Figure 3.1. A comparison of the trend in calculated

Metal	K_{h1}	K_{s1} (calculated)	Metal	K_{h1}	K_{s1} (calculated)
Ag +	-11.9	-7.3	La 2+	-8.5	-5.3
Al 3+	-5.4	-3.5	Mg 2+	-12.0	-7.4
Ba 2+	-13.2	-8.0	Mn 2+	-10.8	-6.7
Be 2+	-5.7	-3.7	Nd 3+	-8.0	-5.0
Bi 3+	-1.4	-1.2	Ni 2+	-10.2	-6.3
Ca 2+	-12.6	-7.7	Pb 2+	-7.9	-5.0
Cd 2+	-10.3	-6.4	Pd 2+	-2.3	-1.7
Ce 3+	-8.1	-5.1	Sc 3+	-4.9	-3.2
Co 2+	-9.9	-6.1	Sm 3+	-7.9	-5.0
Cr 3+	-4.2	-2.8	Sn 2+	-3.6	-2.5
Cu 2+	-8.2	-5.1	Sn 4+	-1.0	-1.0
Dy 3+	-8.0	-5.0	Sr 2+	-13.4	-8.2
Er 3+	-7.9	-5.0	Tb 3+	-7.9	-5.0
Eu 3+	-7.8	-4.9	Th 4+	-4.2	-2.8
Fe 2+	-9.7	-6.0	Tl 3+	-0.9	-0.9
Fe 3+	-2.6	-1.9	U 4+	-1.6	-1.3
Ga 3+	-2.6	-1.9	V 3+	-2.7	-2.0
Gd 3+	-8.0	-5.0	Y 3+	-8.1	-5.1
Hf 4+	-1.2	-1.1	Yb 3+	-7.7	-4.9
Hg 2+	-3.8	-2.6	Zn 2+	-9.2	-5.7
In 3+	-4.4	-3.0	Zr 4+	-0.6	-0.7

Table 3.1: Comparison of log K_{h1} values taken from the literature and the corresponding calculated log K_{s1}.[12]

K_{s1} values to the surface adsorption measured experimentally should provide an indication of whether or not the surface coordination model has merit or not.

3.1.3 Silica Gel and Oxidized Silicon Wafer Surface Similarities

It is not unreasonable to think that the surface of an oxidized silion wafer, exposed to an aqueous solution, will be very similar chemically to that of a silica gel particle in contact with an aqueous solution. This is borne out by the results reported in the literature to date and will be discussed in more detail. The equations cited describing metal adsorption on silica gel surfaces lead to several predicted results which have been demonstrated with oxidized silicon wafer surfaces.

Based on the proposed metal coordination model it should never be possible to generate levels of metal adsorption larger than the surface concentration of the reactive ligand $\{Si(OH)_x\}$. If the generally accepted value for {–OH} on silica gel (4.6-5.5 OH/nm^2) is applied, it could be expected that the metal concentration on the surface of oxidized silicon wafers would never exceed (4.6 - 5.5) x 10^{14} at/cm^2 unless some other phenomenon besides coordination were occurring.[27] Additionally, two ways to manipulate the surface concentration would be to vary $[H^+]$ and $[M^{x+}]$. Both observations are supported by published data in the literature.[28-31] All published data to date shows a saturation of metal picked up from cleaning solutions at or less than 1 x 10^{14} at/cm^2. It has also been shown in the cited literature that high pH solutions are much more sensitive to metal contamination than low pH solutions. [29,31,32]

One way in which to decrease $[M^{x+}]$ is to add a competing ligand to the solution. If the ligand-metal complex is more stable than the silica-metal complex, then the ligand can effectively prevent the metal from adsorbing on the surface, as has been shown multiple times with chelating agents and oxidized silicon wafers.[30,32-36] A comparison of the ligand-metal

complex stability constant with the hydrolysis constant or can indicate how effective they will be in preventing metal adsorption on silica. It should be noted, however, that this is not true in all cases as it has been shown that certain ligands added to a solution can also stabilize the metal on the silica gel surface, thereby increasing its adsorption efficiency.[37]

Strictly speaking, in the thermodynamic equilibrium equations, $[M^{x+}]$ is the concentration of the free metal ion, not including any hydrolysis products. It is reasonable to assume that hydrolysis products of metals will also react and form mixed complexes on the surface of the oxide where the metal is not only attached to the wafer surface but is also attached to one or more hydroxyl ions or other ligand present in solution.[19-21] It has been proposed that it is quite possible that particular hydrolysis products will dominate the adsorption at a given pH and any quantitative model will certainly need to take hydrolytic speciation into account.[9] From a qualitative standpoint, it is expected that the basic trend implied by hydrolysis stability constants will be a useful guide but that a certain amount of scatter in the data is to be expected as long as speciation is not quantitatively accounted for. Given that only one bond to the silica surface is necessary to result in adsorption, it is reasonable to assume that the existence of one interchangeable coordination site on the metal is all that is required to see a measurable level of absorption from solution.

There is a significant difference in surface area between silica gel and oxidized silicon surfaces. This difference has implications both for analysis and for the applicability to silicon wafers of stability constants generated using silica gel. Silica gel naturally has a significantly larger absolute number of reactive sites per unit volume in solution as it has a surface area that is described in terms of m^2/g in the literature.[17,19-22] This allows silica gel researchers to work with the silanol concentration experimentally and mathematically as if it were a dissolved ion in

solution as opposed to being a solid surface. It also means that in general, relative to the concentration of metal ions in solution, the reactive silanol sites are significantly more abundant. For oxidized silicon wafers, the exact opposite is true. The relative small surface area (353 cm^2 for a 150 mm wafer, neglecting the very edge of the wafer) means in most cases, (especially for metal concentrations >10 ppb) that the absolute number of metal ions in a cleaning bath will be greater than the absolute number of SiOH sites available. Even if it is assumed that the wafer surface is exposed to the metal ions contained in the boundary layer defined by the diffusion length of a metal ion over the course of the experiment (~1mm under test conditions used in this study), it must be kept in mind that the concentration of metal ions in this boundary layer is relatively unchanging, as additional ions will diffuse in from the bulk solution.[38] This is shown in greater detail in Table 3.2. A practical implication of this is that while a quantitative model becomes more difficult to verify experimentally, for metals with ligand exchange rates that are fast relative to the exposure time, graphing the calculated surface stability constant versus the

Ion	at/cm^3 per ppb	Atoms in 50 L Bath at 1 ppb	Atoms in 50 L Bath at 10 ppb	Atoms in 50 L Bath at 10 ppm	Reactive SiOH per wafer
Mg	2.48E+13	1.24E+18	1.24E+19	1.24E+22	3.53E+16
Ca	1.50E+13	7.51E+17	7.51E+18	7.51E+21	3.53E+16
Sr	6.87E+12	3.44E+17	3.44E+18	3.44E+21	3.53E+16
Ba	4.39E+12	2.19E+17	2.19E+18	2.19E+21	3.53E+16
Fe	1.08E+13	5.39E+17	5.39E+18	5.39E+21	3.53E+16
Co	1.02E+13	5.11E+17	5.11E+18	5.11E+21	3.53E+16
Ni	1.03E+13	5.13E+17	5.13E+18	5.13E+21	3.53E+16
Cu	9.48E+12	4.74E+17	4.74E+18	4.74E+21	3.53E+16
Pb	2.91E+12	1.45E+17	1.45E+18	1.45E+21	3.53E+16
Al	2.23E+13	1.12E+18	1.12E+19	1.12E+22	3.53E+16
Zn	9.21E+12	4.61E+17	4.61E+18	4.61E+21	3.53E+16

Table 3.2: Calculated metal atoms present in solution relative to the number of reactive silanols per wafer.

measured surface metal concentration will give a good indication of whether or not the proposed model has any validity or not.

It is also important to note that because of the reduced surface area, it is not possible to gather the kind of bonding information that can be generated from silica gel studies as the concentrations are too low. The practical implication being that {SiOM}, {SiO_2M}, {SiO^-}, and {$SiO2^{2-}$} can't be quantified with current analytical techniques. This makes it even more important to critically evaluate whether or not silica gel provides a good model for oxidized wafers since a great deal of bonding and reactivity information coulud be available to the semiconductor industry if the proposed analogy holds.

The simplest applicability of the complexation model is in the range of pH < 9 although it can be usefully applied across the entire pH range. At pH's > 9, the problem of silica dissolution grows with pH which further complicates the situation as the range of possible side reactions grows immensely. It can be expected however, that the tendencies of a given metal to adsorb at lower pH's will remain the same relative to other metals and so this model can be profitably applied to SC1 solutions as well as SC2 or other acidic chemistries. Quantification of SC1 solutions may prove difficult but no doubt appropriate correction terms can and will be developed by others.

Finally, it must be recognized when evaluating experimental data from very applied tests (like the ones contained in this work) that the values of stability constants published in the literature for silica metal complexes are generally with solutions with well controlled ionic strengths of 1. This is not typical of wafer cleaning solutions and reduces the value of the published constants for quantitatively calculating expected surface coverage.

3.2 Experimental and Results

3.2.1 Adsorption of Metals from Low pH Nitric Solution

Silicon wafers, CZ, p-type, <100>, 1-30 Ωcm, 150 mm diameter, were prepared by scribing and then cleaning the wafers with a 1:1:5 SC1 (NH_4OH:H_2O_2:H_2O) - 1:100 HF:H_2O – 4:1 H_2SO_4:H_2O_2 sequence in order to produce an oxidized silicon surface with low initial metal contamination. These wafers were then contaminated with individual metals using a spin coating technique.[39] In this technique, the wafer is put on a vacuum chuck, a 50 mL aliquot of 10%

NIST Solution	Element	Measured Concentration
1% HNO3	Barium	9.20
10% HNO3	Bismuth	9.40
10% HNO3	Cobalt	10.10
10% HNO3	Copper	10.50
10% HNO3	Iridium	9.70
10% HNO3	Lead	9.70
10% HNO3	Molybdenum	9.60
10% HNO3	Nickel	10.30
10% HCl	Platinum	9.80
10% HNO3	Ruthenium	10.30
10% HNO3	Strontium	9.50
10% HNO3	Tantalum	9.80
10% HNO3	Tungsten	9.60
10% HNO3 + 2% HF	Zirconium	9.90

Table 3.3: Solutions used with measured metal concentrations shown. Target was 10 ppm.

HNO_3 NIST solution containing 10 ppm of a given metal is pipetted onto the wafer and is allowed to stand for 10 minutes, after which is it spun to dryness at 2000+ rpm. Ten minutes allows the surface/solution reaction to come to a steady state.[28,31] After this, the wafer is then measured using either TXRF or VPD-ICP-MS, depending on which technique is most appropriate for the metal. The NIST solutions used for each metal are shown in Table 3.3 along

with the concentration that was measured in the solution by ICP-MS. In all cases, the intended concentration was 10 ppm. As can be seen the solutions were, with the exception of Ba, within 5% of the target concentration.

3.2.2 Results of Metal Adsorption from Low pH Nitric Solution

The metal concentrations seen on the wafers can be seen in table 3.4. In the case of Ir, Cu, Ni, Pt, and Ru TXRF was used due to the fact that their high redox potentials results in an inherently poor collection efficiency for the vapor phase decomposition droplet collection (VPD-DC)

Element	DL	Final	Calculated K_{s1}
Barium	0.01	66.0	-8.00
Bismuth	0.01	83.9	-1.20
Cobalt	0.03	256.0	-6.10
Copper	0.40	305.0	-5.10
Iridium	1.00	74.3	
Lead	0.01	51.8	-5.00
Molybdenum	0.02	516.0	
Nickel	0.50	242.0	-6.30
Platinum	1.00	128.0	
Ruthenium	1.00	224.0	
Strontium	2.00	186.0	-8.20
Tantalum	3.00	237.0	
Tungsten	0.01	360.0	
Zirconium	0.02	1580.0	-0.70

Table 3.4: Wafer surface metal concentrations measured after exposure to contaminated HNO_3. All results are in 10^{10} at/cm^2. Calculated K_{s1} (c.f. Section 3.1.2) is provided for reference.

analytical preparation technique. In the case of Sr and Ta, the ICP-MS samples were lost during analysis and so TXRF data is all that was available for review. Clear differences in the amount of each metal adsorbed on the wafer surface can be readily seen. With the exceptions of Bi and Pb,

these differences trend with the K_{s1} values shown in the table and will be discussed in the Conclusions section of this chapter.

3.2.3 Iron and Calcium Adsorption Versus pH

Silicon wafers, CZ, p-type, <100>, 1-30 Ωcm, 150 mm diameter, were prepared by scribing, cleaning, and thermal oxidation. After this, they were treated with a 35% HNO_3 solution at 87 °C for 15 minutes followed by rinsing in DI water for 10 minutes and then were spun dry. This additional treatment was to help ensure that the surfaces were hydroxylated and fully protonated, as well as to ensure the lowest starting metal levels possible.[25]

A tank was then filled with DI water and spiked to 100 ppb of the desired metal which was in a 0.5M HNO_3 solution. The pH was then measured using a standard pH electrode and recorded. Wafers were dipped in the solution for 10 minutes after which they were rinsed in DI water and spun dry. Between each set of wafers, an known aliquot of HCl was pipetted in to the bath, stirred in and then the pH was measured with the pH electrode. This process was repeated several times to cover the pH range of 4.3 to 0.2. After all wafers had been processed, they were then measured using the VPD-DC-TXRF technique.

3.2.4 Results of Iron and Calcium Adsorption Versus pH

The results of this can be seen in Figure 3.1 below. Clear difference can be seen between Fe^{3+} and Ca^{2+} with the Fe^{3+} being much more efficient at adsorbing on the wafer surface. This fits with the K_{s1} values shown in Table 3.4. It is also in agreement with results published with silica gel.[17] A more complete discussion of the results will be carried out in the Conclusions section.

3.2.5 Metal Adsorption from 1:1:5 SC1

While the principle mechanism being proposed for metal adsorption onto silicon oxide surfaces can be dealt with more precisely at pH's less than 9 (above which silica and silicon oxide dissolve, further complicating the situation in solution and at the surface), it should certainly be

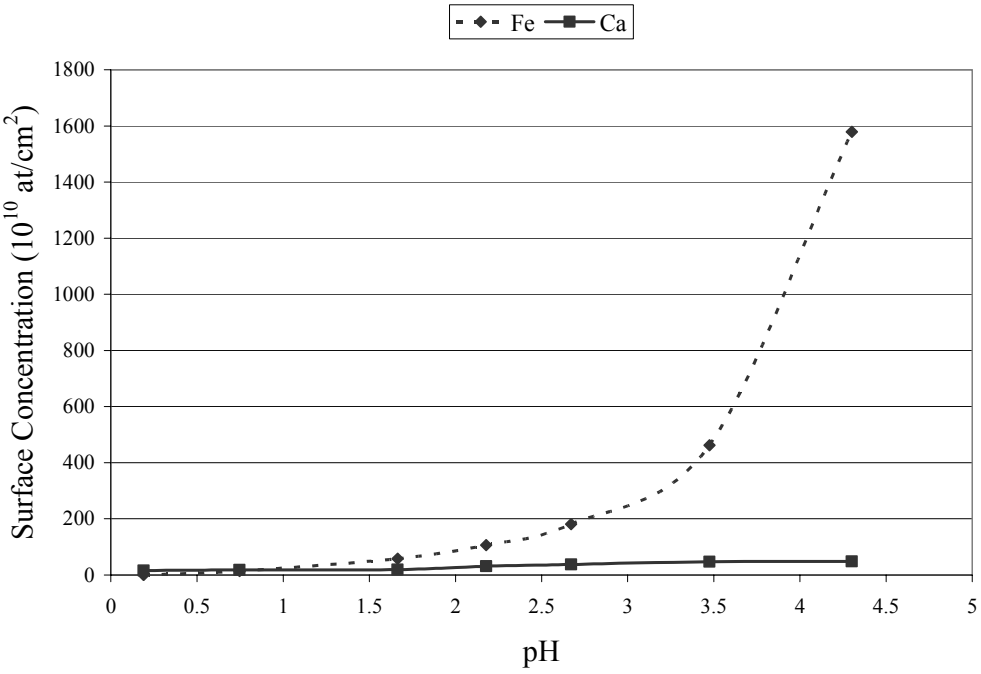

Figure 3.1: Fe and Ca surface concentration versus pH for a 100 ppb solution of Fe^{3+}.

useful as a guide to which metals would be most likely to adsorb from the commonly used SC1 solution which has a pH of 9-11.[40] To test this, silicon wafers, CZ, p-type, <100>, 1-30 Ωcm, 150 mm diameter, were prepared by deglazing with dHF to remove all oxides, leaving a clean silicon surface. A series of 1:1:5 SC1 solutions were mixed in a bath and individually spiked with various levels of different metals using NIST standard solutions. The clean silicon wafers were dipped into the SC1 for 10 minutes, DI rinsed, and spun dry. Analysis of each metal adsorbed on

the surface was carried out using VPD-DC sample preparation technique followed by graphite furnace atomic absorption (GFAA) analysis.

3.2.6 Results of Metal Adsorption from 1:1:5 SC1

The results of this experiment are shown in Table 3.5. Discussion of the results of this experiment will be undertaken in the Conclusions section.

	0.05 ppb	0.1 ppb	0.2 ppb	0.5 ppb	1 ppb	5 ppb	10 ppb
Al	9.20E+10	1.84E+11			1.84E+12		1.84E+13
Ca	7.31E+08				1.46E+10		1.46E+11
Fe	3.52E+10			3.52E+11		3.52E+12	7.03E+12
Mg		2.83E+09			2.83E+10		2.83E+11
Ni			1.73E+09		8.64E+09		8.64E+10
Zn	3.71E+09	7.41E+09			7.41E+10		7.41E+11

Table 3.5: Surface concentration in at/cm^2 versus ppb of a given metal in a 1:1:5 SC1 solution.

3.3 Conclusions and Discussion

As was proposed in the Introduction, it is expected that if the surface of an oxidized silion wafer is behaving in the same manner as the surface of silica gel particles then it would be expected that the results of the above experiments could be understood in terms of the complexation model for metal adsorption on silica gel that has been successfully applied by others.[16-25] As the conditions chosen for these experiments were very much "real world", meaning conditions that are encountered in a manufacturing environment, it is expected that there will be some divergence from results obtained when tests are performed under the well controlled, ideal circumstances reported in the literature. The major differences, as mentioned in the Introduction reside in the uncontrolled ionic strength of these solutions and in the relative abundance of metal ions relative to the available silanol reactive sites.

This former difference certainly accounts for some of the non-linearity in the data. Counterions in the solutions (NO_3^-, Cl^-, NH_3, NH_4^+, O_2H^-) are all expected to take part in solution and surface reactions, impacting final results that are obtained. The latter, surface limited reaction difference makes analysis somewhat easier as the concentration of metal in solution is essentially infinite with respect to the surface. However it can cause nonlinearity as metal ions on the surface can be expected to change surface conditions, making it harder for additional ions to approach the surface and attach.[20] Trends in the data should be the same though and major differences should be minimal if the expected chemical principles are indeed controlling the results.

It has been demonstrated by Schindler under carefully controlled conditions that it was possible to treat surface reactions of silica gel with metals using metal complexation theory and mathematics. After measuring the adsorption of four different metals by silica gel, a pH vs percent adsorption (calculated as percent of metal ion removed form solution) graph was generated as shown in Figure 3.2. As can be seen, the trend is Fe^{3+}>>Pb^{2+}>Cu^{2+}>Cd^{2+} with the rise generally occurring over two pH units for any given metal. This result compares quite favorably with the experimental results seen in Figure 3.1. At first glance in Figure 3.1, it would appear that the area of strongest rise in Fe adsorption is occurring between pH 2 and 4, however, it should be noted that a two orders of magnitude rise occurs between pH 0 and 2 which would account for the results seen by Schindler. It will be recalled that in Schindler's case, the metal ions were the limiting reactant, whereas in this work, the surface silanols are the limiting reagents so the 100X rise in the surface contentration of metal that is observed in Figure 3.1 between pH 0 and 2 would account for the 100% rise in adsorption that Schindler observes. The results seen in Figure 3.1 for Ca^{2+} are also understandable in that Ca^{2+} does not begin to

appreciably hydrolyze until about pH 8 which would suggest that little adsorption should be observed across the pH range tested. This is, in fact, what is observed.[12]

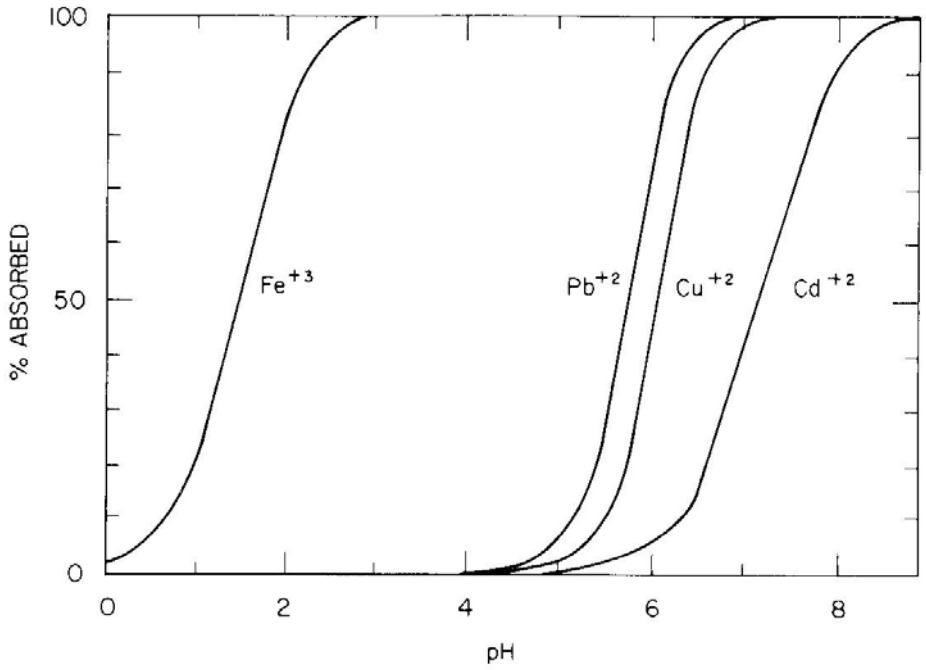

Figure 3.2: Percent adsorption of four metals onto silica gel from solution versus pH. Reprinted from *Journal of Colloid and Interface Science*, Vol 55, P.W. Schindler, B. Fürst, R. Dick, P.U. Wolf, Ligand Properties of Surface Silanol Groups, pp 469-475, Copyright (1976), with permission from Elsevier.

As was noted by Schindler, the pH of the rise in adsorption closely corresponded to the first hydrolysis constant of a given metal. This correlation gave rise to the linear equation with an r-squared value of 0.99 shown earlier in the Introduction: [17]

$$\log K_{s1}K_{s2} = -0.09 + 0.62 \log K_{h1}K_{h2} \qquad 3.15$$

From which it was noted that the simpler equation:

$$\log K_{s1} = -0.39 + 0.58 \log K_{h1} \qquad 3.16$$

could be derived with an r-squared value of 0.98. This simpler equation allows one to calculate a series of K_{h1} values for all metals for which the first hydrolysis constant, K_{s1} is known.

This relationship becomes very useful for analyzing the data from the metal surveys that were undertaken in 10% HNO_3 (pH < 1) and in SC1 solution (pH 9 -11). As noted earlier, since the metal ions in both cases are in great abundance in solution relative to the surface silanols available to the metal ions, a graph of the final surface concentration versus the calculated K_{s1} extrapolated from Schindler's results should give a very good idea of how valid this complexation mechanism hypothesis is. Figure 3.3 shows such a graph for the case of 10 ppb

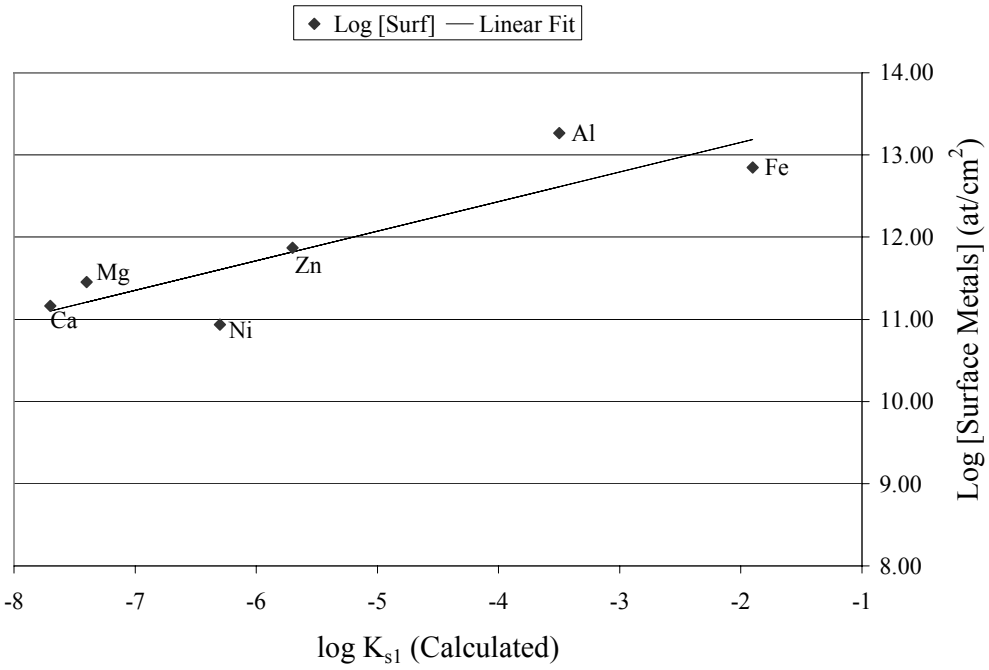

Figure 3.3: Log surface concentration in at/cm^2 for wafers exposed to 1:1:5 SC1 containing 10 ppb of given metals (raw data in Table 3.3) versus the caculated log K_{s1} from Schindler.

concentration of metals in SC1. The r-squared is 0.76 in this particular case, which, while much poorer than Schindler's, is also carried out under significantly less controlled circumstances.

As shown in table 3.4, only 8 of the 14 metals tested at low pH have hydrolysis contants available in the literature. A graph of this data along the same lines of Figure 3.3 results in Figure 3.4. In this case, the fit is very good with the exception of Pb (K_{s1} = -5.0) and Bi (K_{s1} = -1.2). Excluding those two metals, the r-squared for the linear fit is 0.87, even better than was seen with SC1 (the complication of a dissolving oxide surface is avoided in this case) while with them included, the r-squared is 0.15 indicating that there is something fundamentally different about the behavior of these two metals in this particular situation. Why Pb and Bi do not behave as expected is not known but it is possibly due to the fact that Pb^{2+} and Bi^{2+} both complex much

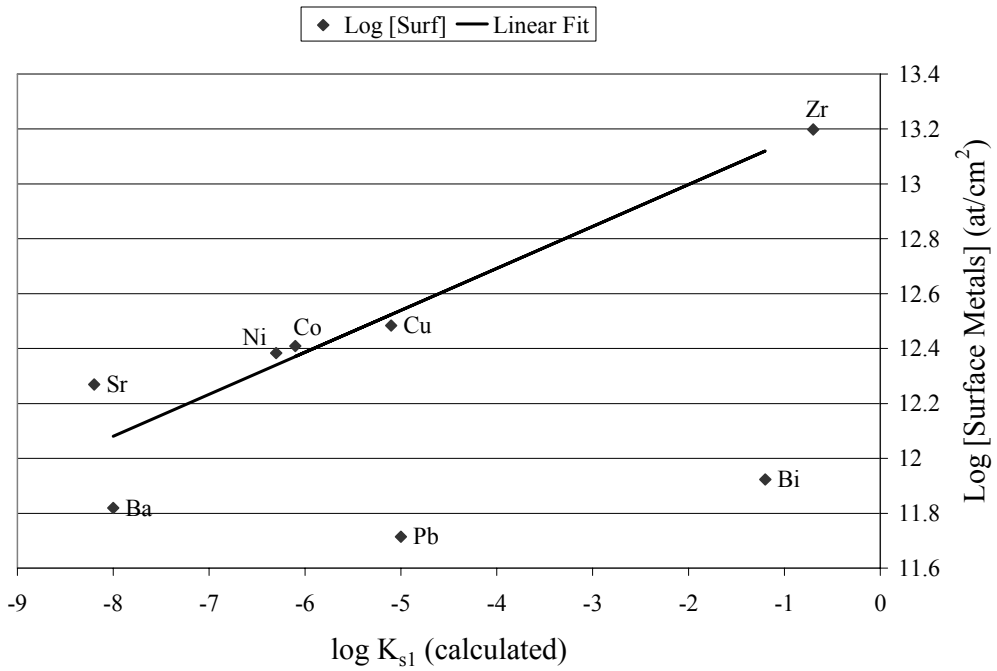

Figure 3.4: Log surface concentration in at/cm^2 for wafer exposed to 10% HNO_3 containing 10 ppm of a given metal (raw data in Table 3.2) versus the caculated log K_{s1} from Schindler.

more strongly with NO_3^- anions than any of the other metals tested. In any case, it deserves additional study in future work.

This approach can be applied to data in the literature with the same pattern emerging. As an example, Loewenstein published a general survey of metal deposition versus a pH range of 3-5.6.[10] A graph of his results at pH 4.5 are shown in figure 3.5. Again, the fit is very good for all but one metal. In this case, the odd metal is Fe^{3+} which is very surprising given its conformance to expectations versus pH in the SC1 experiment, presented earlier. Loewenstein notes this variance from expectation and offers the explanation that it must be due to the Fe^{3+} being already hydrolyzed to a great extent at pH 4.5. This explanation does not satisfy however when considering the results that have been shown in this chapter in SC1, which, at pH 10-11 contains

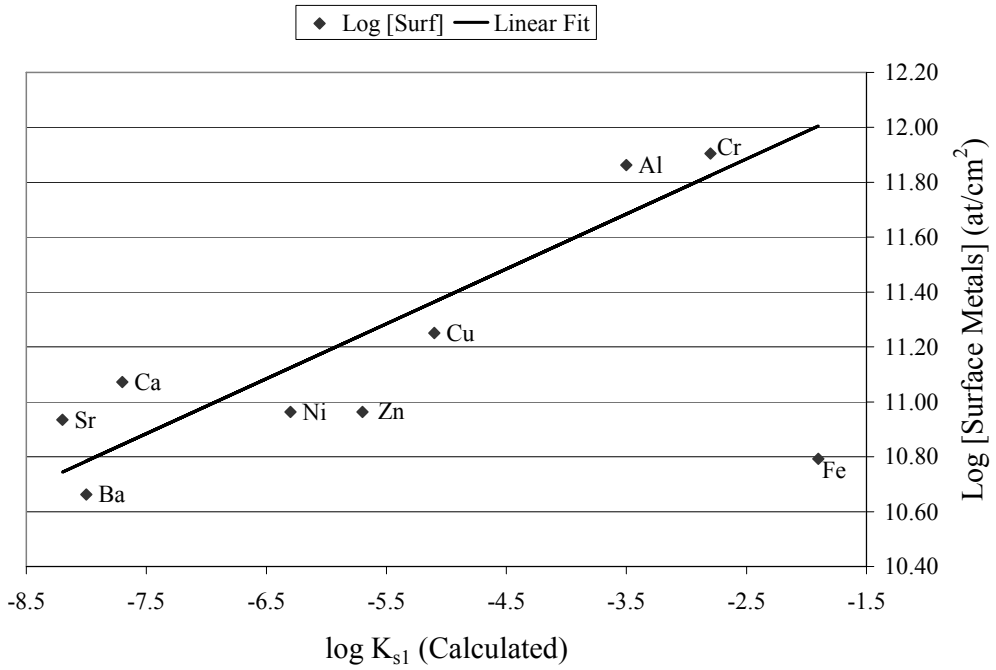

Figure 3.5: Log surface concentration in at/cm^2 (from Loewenstein) for wafer exposed to 0.1M HNO_3 containing 100 ppb of given metals versus the caculated log K_{s1} from Schindler.[10,17]

Fe^{3+} as a mix of hydrolysis products only.[9] Some other explanation is likely correct but can only be speculated about at this time.

As was noted in the Introduction, another key boundary condition on the complexation model is that the concentration of silanols on the surface of the wafer will almost certainly not exceed (4.6-5.5) x 10^{14} at/cm^2 as is the generally accepted case with silica gel.[41] The implication of this is that there should be a practical limit of ~5 x 10^{14} at/cm^2 of any given metal that can be put on an oxidized silicon wafer from solution. A test of this using SC1 and Fe and Ca is shown in Table 3.6. In the case of Fe it can be seen that each decade increase in Fe concentration results in a corresponding decade of increase for metal on the surface, until the low 10^{13} threshold (~10% of a "monolayer") is reached, at which point, the increase begins to drop off. For Ca, the first order dependence on metal concentration is ongoing at 100 ppb as the surface concentration is still below the 10^{13}. A survey of the literature shows many authors run into this same limit even when adding up to 1 ppm of Fe to SC1. [29-31]

	Control	+0.1 ppb	+1.0 ppb	+10 ppb	+100 ppb
Fe	4.35	25.2	272	1509	2544
Ca	<0.7		3.1	18.3	260

Table 3.6: Fe^{3+} and Ca^{2+} adsorption measured on silicon oxide from SC1 spiked to progressively higher levels of each metal. Results in 10^{10} at/cm^2.

While not proving the case conclusively, all of these results reported in this chapter support the proposal that the surfaces of oxidized silicon wafers are chemically similar to the surface of silica gel particles. This being the case, it is not a large intuitive leap to state that silica gel chemistry and literature results can be used to profitably explain and predict the

chemistry of metals at the surface of oxidized silicon wafers. Further work will have to be done to take the (what at best can be described as qualitative) approach proposed in this dissertation, and construct a more rigorous, quantitative model that can accurately predict expected adsorption levels for a given metal if the pH, ionic strength, concentration of potential ligands, and other thermodynamically significant variables are known. To achieve this goal it will also be necessary to either create new analytical techniques or new methods of applying current analytical techniques so that the surface concentrations of all reaction products can be determined down to the range of 10^9 to 10^{10} at/cm^2.

3.4 References

(1) Kern, W. and Poutinen, D.A. *RCA Review* **1970** *31* 207.

(2) Kern, W. and Poutinen, D.A. *RCA Review* **1970** *31* 234.

(3) Hourai, M.; Naridomi, T.; Oka, Y.; Murakami, K.; Sumita, S.; Fujino, N.; Shiraiwa, T. *Jpn. J. Appl. Phys.* **1988** *27* L2361.

(4) Anttila, O.J.; Tilli, M.V.; Schaekers, M.; Claeys, C.L. *J. Electrochem. Soc.* **1992** *139* 1180.

(5) Schmidt, H.F.; Mertens, P.W.; Meuris, M.; Verhaverbeke, S.; Heyns, M.M.; Dillenbeck, K. *Proceedings of First International Symposium on Ultra Clean Processing of Silicon Surfaces;* IMEC Press: Leuven Belgium; 1992.

(6) Norga, G.J.; Kimerling, L. *J. Electron. Mater*. **1995** *24* 397.

(7) Helms, C.R.; Park, H. *ECS Proceedings **1994** 94-7* 26.

(8) Ryuta, J. ; Yoshimi, T.; Kondo, H.; Okuda, H; Shimanuki, Y. *Jpn. J. Appl. Phys*. **1992** *31* 2338.

(9) Mori, Y.; Uemura, K. ; Shimanoe, K. J. *Electrochem Soc* **1995** *14* 3104.

(10) Loewenstein, L.M.; Charpin, F.; Mertens, P.W.; *J. Electrochem. Soc.* **1999** *146* 719.

(11) Inczédy, J. *Analytical Applications of Complex Equilibria*; Ellis Horwood Limited: Chichester, U.K. **1976**; p 26.

(12) Kragten, J. *Atlas of Metal-Ligand Equilibria in Aqueous Solution*; John Wiley and Sons: New York, 1978.

(13) Sillen, L.G. et al, *Stability Constants of Metal Ion Complexes*.; The Chemical Society: London ,1964; *Supplement No. 1* 1971.

(14) Baes, C.F.; Mesmer, R.E. *The Hydrolysis of Cations;* John Wiley and Sons: New York, 1976.

(15) Burgess, J. *Ions in Solution: Basic Principles of Chemical Interactions*; Ellis Horwood Limited: Chichester, U.K. 1988.

(16) Stumm, W.; Kummert, R.; Sigg, L. *Croat. Chem. Acta* **1980** *53 (2)* 291.

(17) Schindler, P.W.; Fürst, B.; Dick, R.; Wolf, P.U. *J.Colloid Sci.* **1976** *55* 469.

(18) Schindler, P.W. *Metal Ions in Biological Systems* **1984** *18* 105.

(19) James, R.O.; Healy, T.W. *J.Colloid Sci.* **1972** *40* 42.

(20) James, R.O.; Healy, T.W. *J.Colloid Sci.* **1972** *40* 53.

(21) James, R.O.; Healy, T.W. *J.Colloid Sci.* **1972** *40* 65.

(22) Dugger, D.L.; Stanton, J.H.; Irby, B.N.; McConnell, B.L.; Cummings, W.W.; Maatman, R.W. *J. Phys. Chem.* **1964** *68* 757.

(23) Schindler, P.; Wälti, E.; Fürst, B. *Chimia* **1976** *30* 107

(24) Schindler, P.; Kamber, H.R. *Helvetica Chimica Acta* **1968** *51* 1781.

(25) Ahrland, S.; Grenthe, I.; Norén, B. *Acta Chem. Scand.* **1960** *14* 1059.

(26) Hurd, T.Q. et al, *ECS Proceedings* **1995** *95-20* 277.

(27) Iler, R.K. *The Chemistry of Silica*; John Wiley and Sons: New York 1979; p 665.

(28) Loewenstein, L.; Mertens, P.W. *J. Electrochem. Soc.* **1998** *145* 2841.

(29) Hayami, Y.; Okui, Y.; Ogawa, H.; Fujimura, S. *ECS Proceedings* 97-3; The Electrochemical Society: Pennington, NJ 1997; p 97.

(30) Hall, L.; Sees, J.; Hurd, T.; Schmidt, B.; Bellay, L.; Loewenstein, L.; Mertens, P.W. *Proceedings of the Fourth International Symposium on Ultra Clean Processing of Silicon Surfaces;* Scitec Publications: Switzerland 1999; p 53.

(31) Mouche, L.; Tardif, F.; Derrien, J.; *J. Electrochem. Soc.* **1995** *142* 2395.

(32) Hurd, T.Q.; Rotondaro, A.L.P.; Sees, J.; Misra, A.; Appel, C.;*ECS Proceedings 97-35;* The Electrochemical Society: Pennington, NJ 1997; p 105.

(33) Sugihara, Y.; Tanaka, K.; Kawakami, M.; U.S. Patent 5302311, 1994.

(34) Hayashida, I.; Kakizawa, M.; Umekita, K.; Nawa, H.; Maraoka, H.; U.S. Patent 5290361, 1994.

(35) Martin, A.R.; Baeyens, M.; Hub, W.; Mertens, P.W.; Kolbesen, B.O. *Microelectronic Engineering* **1999** *45* 197.

(36) Gale, G.W.; Rath, D.L.; Cooper, E.I.; Estes, S.; Okorn-Schmidt, H.F.; Brigante, J.; Jagannathan, R.; Settembre, G. *J. Electrochem. Soc.* **2001** *148* G513.

(37) Smith, G.W.; Jacobson, H.W. *J. Phys. Chem.* **1964** *68* 757.

(38) Lide, D.R. Ed. *CRC Handbook of Chemistry and Physics, 77th Ed.* CRC Press: New York 1996**.**

(39) Hourai, M.; Naridomi, T.; Oka, Y.; Murakami, K.; Sumita, S.; Fujino, N.; Shiraiwa, T. *Jpn. J. Appl. Phys*. **1988** *27* L2361.

(40) O'Brien, S. *TI Technical Report Number 08-94-28*, 1994**.**

(41) Iler, R.K. *The Chemistry of Silica*, John Wiley and Sons: New York 1979; p 633.

CHAPTER 4

BEHAVIOR OF METAL CONTAMINANTS ON SILICON SUBSTRATES DURING HIGH TEMPERATURE THERMAL CYCLES

4.1 Introduction

The deleterious effects of metallic contamination on silicon devices have drawn the attention of researchers since the early days of the semiconductor industry.[1-9] Not only can they easily be transferred to the wafers from non-optimized process tools and low quality gases and chemicals, but they also strongly reduce the yield of silicon devices.[10,11,12] Metals can degrade the dielectric properties of gate oxides causing premature breakdown and diffuse into the bulk of the silicon material resulting in an increase of the junction leakage and a reduction of the minority carrier lifetime.[4,5,13,14]

Metallic contamination is specified at 10^9 at/cm^2 in advanced ultra large scale integration (ULSI) technologies.[15] However, contamination up to 10^{12} at/cm^2 has been observed during processing.[10,11] Electrically active metallic contamination present in silicon can be evaluated directly with quantitative techniques like deep level transient spectroscopy (DLTS), or indirectly by analyzing its effect on the electrical properties of the material.[16] In this second approach, minority carrier lifetime (MCLT) and minority carrier diffusion length (L) have become common measures of the amount of contamination present in silicon wafers due to their fast sample preparation and wafer mapping capabilities.[17]

During high temperature thermal processing, as occurs in the semiconductor manufacturing front end of line, metal contaminants have three paths they can follow: 1) stay at/on the surface, 2) evaporate, or 3) diffuse into the silicon substrate. While it is rarely possible to absolutely quantify to what extent each path is followed by a given metal, it is possible to

combine known thermodynamic information with measurements to reach reasonable conclusions about how each metal will preferentially behave under a given set of circumstances. Metals that follow the first path can be readily detected in most cases using surface analytical techniques like TXRF or VPD-ICP-MS. Those following the second path can only be detected if they happen to spread to neighboring wafers and cause detectable changes in their surface or bulk properties. Metals that follow the third path can be detected by their impact on MCLT and L as measured by the microwave photoconductance (μPCD, c.f. Section 1.3.1) and surface photovoltage (SPV, c.f. Section 1.3.2) techniques, respectively, if they create minority carrier traps of sufficiently large capture cross section near the conduction band for n-type silicon, near the valence band for p-type silicon, or near mid-band gap for any doping type.

Following diffusion into the bulk silicon crystal, depending on their solubilities and diffusivities, metals will exhibit one of several behaviors. If their diffusivity is high and their solubility is low (e.g. Cu) metals will tend to precipitate, either at the surface or in the bulk. If their diffusivity is low and/or their solubility is high (e.g. Fe), they will tend to form either substitutional defects (replacing a Si atom in the crystal) or interstitial defects (residing in the spaces between atoms in the crystal). The general trend is that the tendency to form subsitutional defects increases with atomic number in a given period, with those heavier than the elements Fe, Ru, Os (3d, 4d, 5d) preferentially forming substitutional defects while Fe, Ru, Os and metals with lower atomic numbers preferentially forming interstitial defects. Most electrically active defects formed by metals in silicon are due to interstitial defects and will exhibit four different charge states: double positively charged (++), single positively charged (+), neutral (0), and single negatively charged (-). Changes in these charge states due to electrical activity result in what are known as double donor (++/+), donor (+/0), and acceptor (0/-) states. The activation

energies of these states are measured from the neighboring band edge with either a negative sign, indicating distance from the conduction band (e.g. E_c-0.xx eV) or with a positive sign, indicating distance from valence band edge (e.g. E_v+0.xx eV).[32]

Interstitial defects are able to form what are known as donor-acceptor pairs with substitutional impurities such as doping atoms. In the case of Fe, its positively charged donor state is able to form an electrostatic bond with the neighboring negatively charged acceptor state of a B atom, resulting in an FeB "pair". These types of pairings have been detected between many elements, including between the substitutional and interstitial forms of a single metal (e.g. Au_sAu_i).

In the first part of this chapter, MCLT measured by microwave photoconductance decay (μPCD) and L measured surface photovoltage (SPV) are evaluated and used to study Fe and Cu dissolved in silicon wafers, while TXRF is used to measure them on the silicon wafer surface. A broad concentration range of controlled contamination is used that is relevant for ULSI processing. In the second part of this chapter, what is learned from the detailed study of Fe and Cu in the way of metrology and experimental methodology is then applied to a broad range of metals (Ba, Bi, Co, Ir, Mo, Ni, Pb, Pt, Ru, Sr, Ta, W, and Zr) that are of interest in semiconductor manufacturing due to their potential uses as new materials in advanced devices. Surface and bulk analyses are applied as appropriate to give an accounting of their behavior during thermal processing.

4.2 Experimental for Fe and Cu Contamination

Initially, a comprehensive study of the characterization techniques was performed for the case of Fe contamination in p-type silicon. For that purpose, Czochralski grown (Cz), p-type, <100>, 6-10 and 24-36 Ωcm, 125 mm diameter wafers, with medium oxygen content, received

uniform Fe contamination from Fe spiked 0.25:1:5 (NH_4OH:H_2O_2:H_2O SC1) solutions.[18] The resulting Fe surface concentration measured by vapor phase decomposition – droplet collection – total reflection x-ray fluorescence (VPD-DC-TXRF, c.f. Sections 1.2.1 and 1.2.3) was in the range between 10^9 at/cm^2 and 10^{13} at/cm^2.[19] The surface contamination was subsequently diffused into the wafers by thermal treatments at 900 ºC for 30 min in: dry O_2, wet H_2+O_2 (pyrophoric) or N_2 ambients. The ramp-up for the treatments in oxidizing ambient was done in 5% O_2. The cool down in all cases was performed at a rate of 5 ºC/min until 650 ºC in N_2. The samples were then removed from the furnace to ambient room temperature in 10 min. This procedure was intended to reproduce typical processing conditions found in semiconductor manufacturing. Oxidation of silicon in dry O_2 or wet H_2+O_2 atmospheres is routinely performed for the formation of oxide films. Generally dry O_2 is used for films of 1000A thickness or less while pyrophoric H_2+O_2 is used to grow oxide films thicker than 1000A as the H_2O formed by the reaction of H_2+O_2 is smaller than O_2 and so thicker oxide films can be grown in a shorter period of time than is possible with O_2. Annealing in a N_2 atmosphere is performed whenever it is desirable to subject silicon wafers to a thermal treatment without growing any oxide films, e.g. to diffuse implanted species into the silicon or to improve interface properties between oxide films and the underlying silicon substrate.

A second set of experiments was performed where both n-type and p-type substrates (Table 4.1) were used to address the impact of the doping type on the activity of the impurities in silicon. The Fe contamination was deposited as described before from spiked SC1 solutions in a controlled and uniform way. Copper was transferred to hydrophobic wafers from Cu spiked diluted HCl solutions (1:10^4, HCl:H_2O). The resulting surface contamination was in the range of

10^9 to 5 x 10^{13} at/cm^2.[20] In this second set of experiments, annealing in dry oxygen at 900 ºC for 30 min was used to drive the impurities into the wafers.

MCLT was measured by μPCD with a Phoenicon GmbH instrument operating at 22 GHz in reflection mode. L was evaluated using by the SPV technique using a Semiconductor Diagnostics Inc. model CMS-IIIA.[21] Also, the bulk Fe content was calculated in p-type silicon from the dependence of the minority carrier diffusion length on the FeB pair concentration.[21] To allow the FeB pairing reaction to reach a steady state in the p-type samples, a week was allowed to pass between annealing and measurement.

Growth method	Cz	FZ	Cz	FZ
Doping type	p	p	n	n
Resistivity (Ωcm)	10-20	10-20	10-12	5.8-6.6

Table 4.1: Description of the substrates used in the second set of MCLT studies.

Hydrogen passivation via removal of all oxide films by HF (deglazing) was used for incoming inspection of the silicon wafers by μPCD. This procedure passivates the surface dangling bonds with protons and allows the extraction of the MCLT value of the starting material without the need of any thermal treatment. Only wafers with MCLT > 300 μs were selected to be used for further experiments in accordance with the limits specified in the Semiconductor Industry Association (SIA) roadmap.[15] The passivation was accomplished by immersion for 10 min in a 4.9 % HF solution at room temperature followed by a 5 min DI water overflow rinse and N_2 spin dry. To illustrate the method, in Figure 1, the effective lifetime of poor quality Cz and high quality float zone (FZ) p-type wafers is shown as a function of the

elapsed time after passivation. A clear difference between the initial value of the effective MCLT measured by μPCD ($\tau_{\mu PCD}$) is observed when comparing these CZ and FZ wafers. The lifetime of the FZ wafers is 2 to 3 times higher than that of the CZ wafers. This might be related to intrinsic defects or contamination present in this particular set of CZ samples.[22] The surface passivation after the HF treatment is relatively stable in cleanroom air. The low surface recombination velocity can be kept for at least 5 hours after the HF passivation (Figure 4.1). This is in agreement with what has been observed for hydrogen terminated surfaces stored in H_2O where the surface passivation remains intact for several hours.[23]

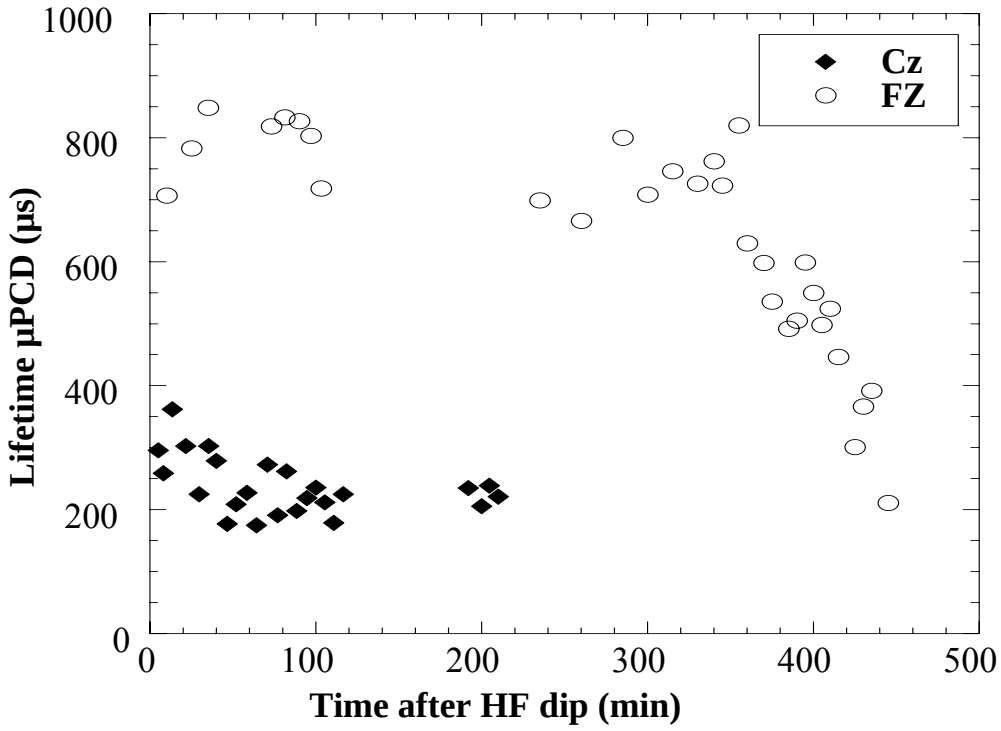

Figure 4.1: Minority carrier lifetime measured by μPCD as a function of the exposure time to cleanroom air after HF passivation for non-contaminated p-type Cz and FZ wafers.[20] Reproduced by permission of The Electrochemical Society, Inc.

4.3 Results and Discussion

4.3.1 - μPCD and SPV Analysis of Fe Contaminated p-type Silicon

When the Fe concentration in the bulk silicon determined by SPV is plotted as a function of the initial Fe surface contamination measured by VPD-DC-TXRF a good correlation is obtained for all annealing ambients (Figure 4.2).[21] However, the amount of Fe driven into the substrate depends on the ambient used during annealing. In dry O_2, approximately 50 to 70 % of the

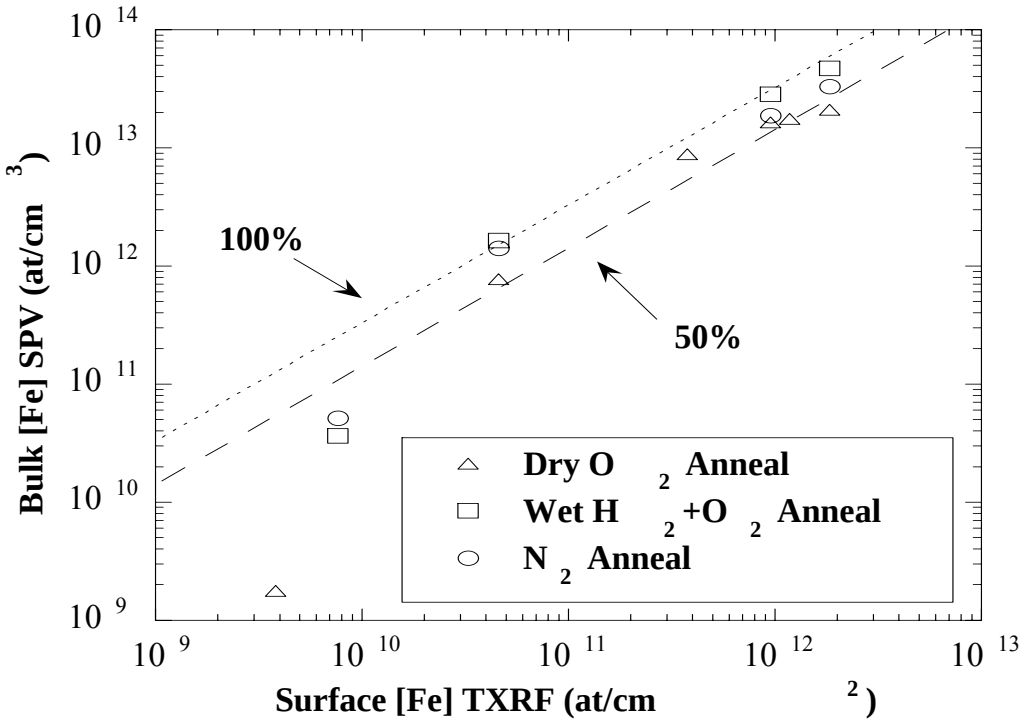

Figure 4.2: Fe concentration in bulk silicon measured by surface photovoltage as a function of the Fe surface concentration before annealing for p-type Cz samples annealed at 900 ºC for 30 min in different ambients. The 100% and 50% lines are where points would be expected to fall if 100% and 50% of the Fe was being driven into the bulk silicon crystal, respectively.[20] Reproduced by permission of The Electrochemical Society, Inc.

surface Fe contamination is incorporated in the substrate. The use of N_2 ambient causes the diffusion of 70 to 100 % of the surface contamination in the bulk. This may be understood by the fact that in an inert ambient the majority of the surface contamination can diffuse into the bulk whereas in a dry oxidizing environment part of the Fe is segregated from the bulk by the growing oxide layer.[24] Interestingly, when the wafers are annealed in a wet oxidizing ambient almost 100% of the surface contamination is incorporated in the bulk. The difference in the behavior of the Fe contamination during annealing in dry and wet oxidizing ambients is possibly caused by the presence of hydrogen during the wet oxidation. The reaction of the Fe with O_2 or SiO_2 could be inhibited or reduced by the hydrogen due to its reducing properties. This in turn would allow the Fe to remain mobile and diffuse into the substrate. This difference can also be seen in the surface concentration before and after thermal treatment as shown in Table 4.2 where less residual Fe is measured on the surface after wet oxidation as compared to dry oxidation.

The effective MCLT ($\tau_{\mu PCD}$) as a function of the bulk Fe contamination for wafers annealed in different ambients is shown in Figure 4.3. The criticality of the surface passivation can be observed on the effective lifetime values. The oxide layer that is formed on the wafers during annealing in dry and wet oxidizing ambients, provides a low surface recombination velocity, allowing the bulk lifetime to dominate the μPCD measurements (as discussed in Chapter 1).[25,26] This effect is crucial for the analysis of lowly contaminated wafers where the bulk lifetime is expected to be very high and can only be determined if the wafers have a good surface passivation. For heavily contaminated samples, the bulk MCLT is low and dominates the measurements even if the wafers are poorly surface passivated. The results for the nitrogen

Condition	Pre	Post O_2	Post H_2+O_2
HF Control	0.08	0.31	0.88
SC1 Control	4.35	0.56	0.77
SC1+0.1 ppb Fe	25.2	6.7	0.48
SC1+1 ppb Fe	272	38.7	2.86
SC1+10 ppb Fe	1508	1166	697
SC1+100 ppb Fe	2544	1835	690

Table 4.2: Surface Fe concentration, measured by VPD-DC-TXRF in 10^{10} at/cm^2 before and after thermal treatment in both dry and wet ambients at 900 °C.

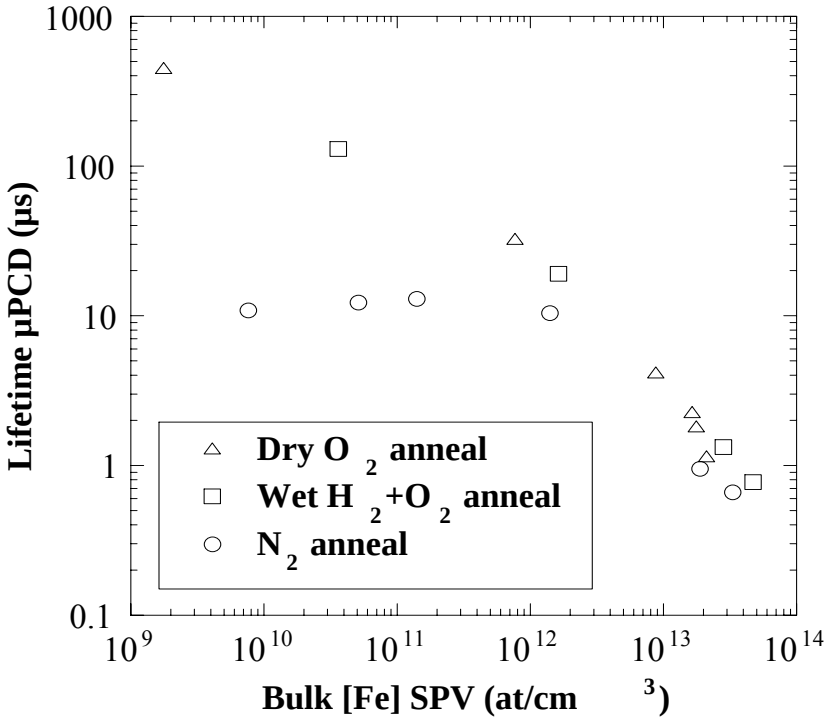

Figure 4.3: Minority carrier lifetime measured by microwave photoconductance decay as a function of the Fe bulk concentration after annealing for p-type Cz samples annealed at 900 ºC for 30 min in different ambients.[20] Reproduced by permission of The Electrochemical Society, Inc.

annealed samples in Figure 4.3 illustrate the effect of the surface passivation on the MCLT measured by μPCD. In this case, the wafers are expected to have a poor surface passivation and therefore, for bulk [Fe] lower than 10^{12} at/cm^3, the measured lifetime is limited by the surface recombination velocity and saturates at values of approximately 10 μs.[26] Samples with similar levels of contamination that have a surface oxide layer show higher values of MCLT as in this case the surface recombination is not a limiting factor and the bulk lifetime still dominates the results. Wafers with bulk [Fe] higher than 10^{12} at/cm^3, have low bulk MCLT which dominates the measurements even in the case of wafers with poor surface passivation. This confirms that a good surface passivation is essential for consistently measuring bulk MCLT with μPCD over a wide range of contamination levels.[26]

More detailed studies of the behavior of the effective lifetime measured by μPCD as a function of the bulk [Fe] determined by SPV were performed. The values from Figure 4.3 for the wafer annealed in dry and wet oxidizing ambients were complemented with measurements for the whole range of Fe contamination, especially in the low concentration portion (Figure 4.4). Only dry and wet oxidizing ambients were used to drive the contamination into the substrates to optimize the surface passivation of the samples. A good correlation between the $\tau_{\mu PCD}$ and the Fe content in the bulk is obtained (Figure 4.4). A linear decay of the $\tau_{\mu PCD}$ with the bulk [Fe] is observed in the range from $3x10^{11}$ to $4x10^{13}$ at/cm^3. In this region the recombination activity of the FeB pairs can be characterized by their effective capture cross-section $\sigma_{e(FeB)}$ according to the equation:

$$\sigma_{e(FeB)} = \frac{1}{\tau_{bulk}\, v_{th}\, N_{Fe}} \qquad 4.1$$

where $v_{th} = 10^7$ cm/s is the carrier thermal velocity at room temperature, N_{Fe} is the bulk Fe concentration (measured by SPV) and τ_{bulk} is assumed to be equal to $\tau_{\mu PCD}$. Calculating from the

results obtained in the linear portion of the graph gives $\sigma_{e(FeB)} = 3.5 \pm 0.6 \times 10^{-15}$ cm^2. To study the effect of the surface passivation on the minority carrier diffusion length (L) measured by SPV, oxide passivated wafers were analyzed and then remeasured after removal of the oxide surface layer with HF (Figure 4.5). On the non-passivated samples, L saturated at values around 500 μm. This is in agreement with the maximum values that can be measured with the standard SPV method on non-passivated wafers, where L_{max} = 0.7 wafer thickness, which in this case is equal to 455 μm.[26] On the other hand, on the oxide passivated wafers L increased to values around

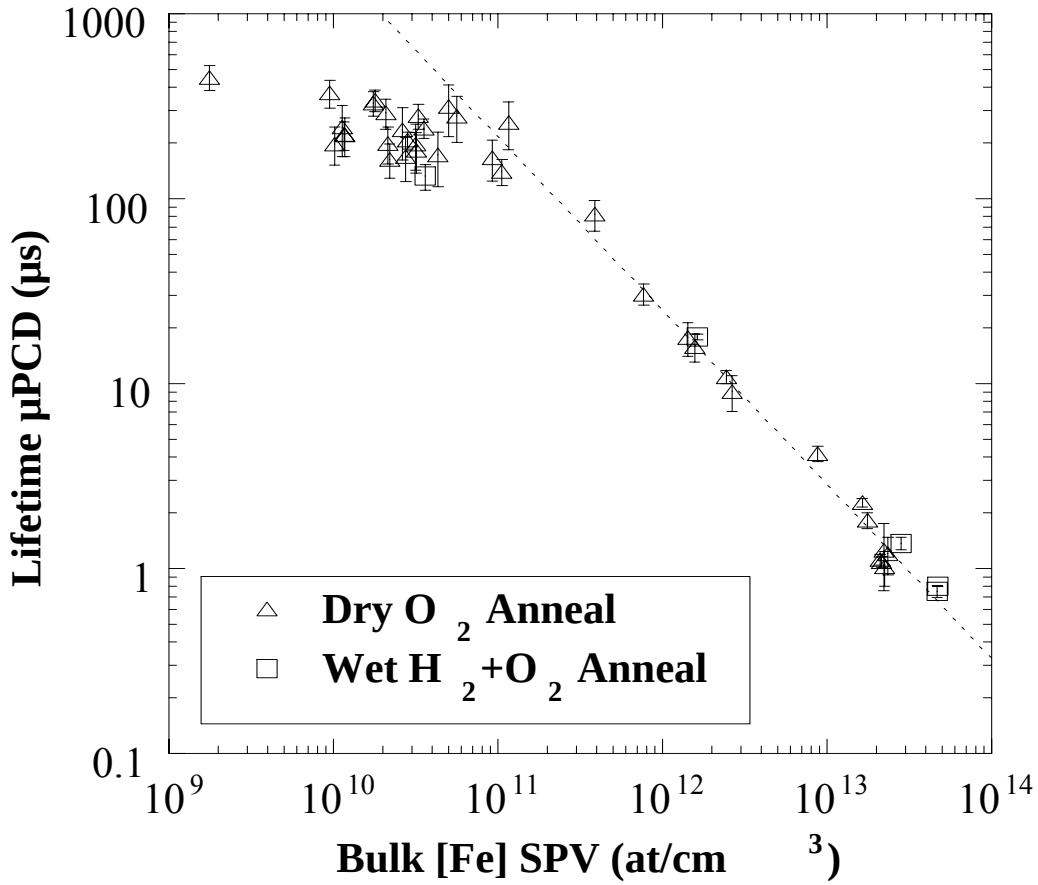

Figure 4.4: Minority carrier lifetime measured by microwave photoconductance decay as a function of the Fe bulk concentration after dry and wet anneals.[20] Reproduced by permission of The Electrochemical Society, Inc.

2000 μm. Those higher-than wafer thickness values are associated with an artifact of the SPV method and are expected to be observed when the wafer backside has a low surface recombination velocity.[27] A general consequence of this is that it is possible to see L increase in wafers following oxidation if no electrically active contaminants are introduced during the oxidation process.

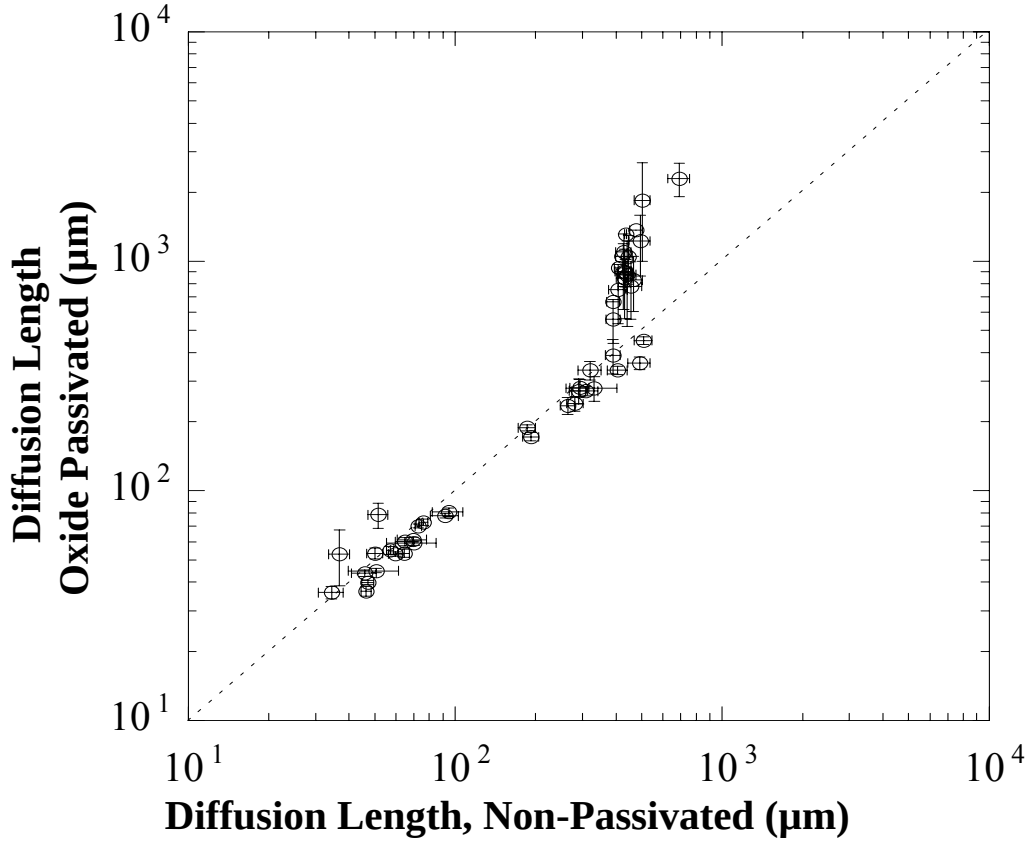

Figure 4.5: Diffusion length measured by SPV on p-type Cz wafers before and after the removal of the surface oxide passivation.[20] Reproduced by permission of The Electrochemical Society, Inc.

As was noted in Chapter 1, interstitial Fe (Fe_i) and FeB pairs are very different in their ability to act as minority carrier traps. Analysis of the recombination activity of Fe_i was performed by comparing the L measured on wafers that had the FeB pairs dissociated by intense light exposure with the L measured before dissociation.[28] For a wide range of Fe contamination it is possible to observe that Fe_i causes a reduction of L by a factor of 2 to 3 when compared to values measured in the presence of FeB pairs (Figure 4.6). For bulk [Fe] < $5x10^{10}$ at/cm^3 this distinction in the recombination activity is not evident anymore indicating that the accuracy of

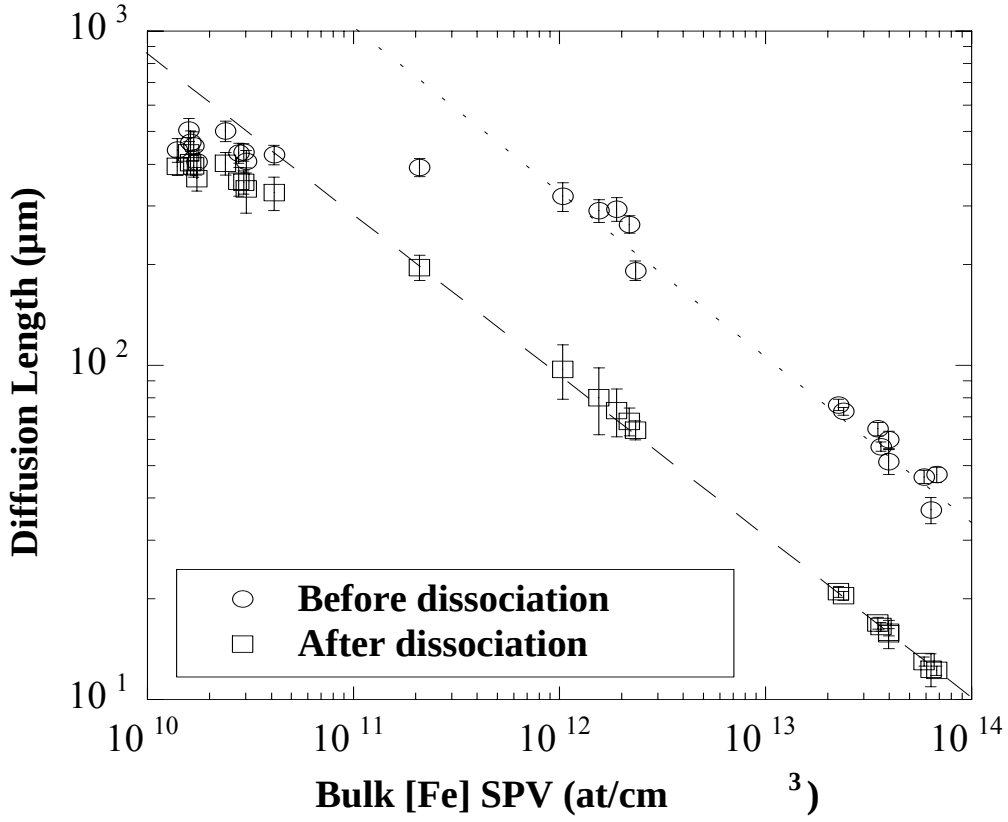

Figure 4.6: Minority carrier diffusion length measured by SPV as a function of the bulk Fe concentration for p-type Cz wafers before and after the dissociation of the FeB pairs.[20] Reproduced by permission of The Electrochemical Society, Inc.

the determination of the Fe content in the bulk silicon might be compromised for values lower than that.

The minority carrier lifetime from the SPV measurements can be estimated from L with equation:

$$L^2 = D_n \tau_{SPV} \qquad 4.2$$

with D_n being the electron diffusion coefficient equal to 38 cm/s^2. Using the calculated τ_{SPV} as τ_{bulk} in equation (1), it is then possible to estimate the electron capture cross-section of the FeB pairs ($\sigma_{e(FeB)}$) and Fe_i ($\sigma_{e(Fe_i)}$) from the SPV measurements. The obtained values are $\sigma_{e(FeB)}$ $=2.5\pm0.5x10^{-15}$ cm^2 and $\sigma_{e(Fe_i)} = 3.0\pm0.1x10^{-14}$ cm^2 which are in good agreement with the literature.[29] The $\sigma_{e(Fe_i)}$ being one order of magnitude larger than $\sigma_{e(FeB)}$ shows, as expected, that Fe_i is a more efficient electron trap than the FeB pair. Comparing the values of $\sigma_{e(FeB)}$ as calculated from SPV ($2.5\pm0.5x10^{-15}$ cm^2) and μPCD ($3.5\pm0.6x10^{-15}$ cm^2) a good agreement is obtained indicating that both approaches give comparable results that are both in good agreement with the literature.

4.3.2 - Impact of Fe and Cu Contamination in p-type and n-type Silicon.

Following the procedure described in Section 4.2, surface Fe contamination was intentionally deposited on n-type and p-type wafers (Table 4.1) and was driven into the substrates by annealing at 900 ºC for 30 min in dry O_2. To simplify discussion and analysis, the bulk [Fe] was measured on the p-type samples with SPV and these bulk concentrations of Fe were assumed to be present in the n-type wafers that were processed with the same conditions, following an approach used by others.[7,8] The Fe is expected to be in interstitial sites in both types of substrates and predominantly paired with B in the p-type wafers. The measured $\tau_{\mu PCD}$ plotted as a function of the bulk [Fe] (Figure 4.7) shows that Fe is more detrimental to p-type material

than to n-type.[30,31] Apparently, the $\tau_{\mu PCD}$ on the contaminated FZ wafers of both types is slightly lower than on Cz wafers.

Insight into the recombination activity of Fe in the different substrates can be gained by once again analyzing the capture cross-section (σ) of the Fe traps. In Table 4.3, the values of σ calculated using equation (1) from μPCD and SPV results are presented for p-type Cz (Czp), p-type FZ (FZp), n-type Cz (Czn) and n-type FZ (FZn). It is assumed that Fe is interstitial in n-type material. A very good agreement with the values of the capture cross-section published in

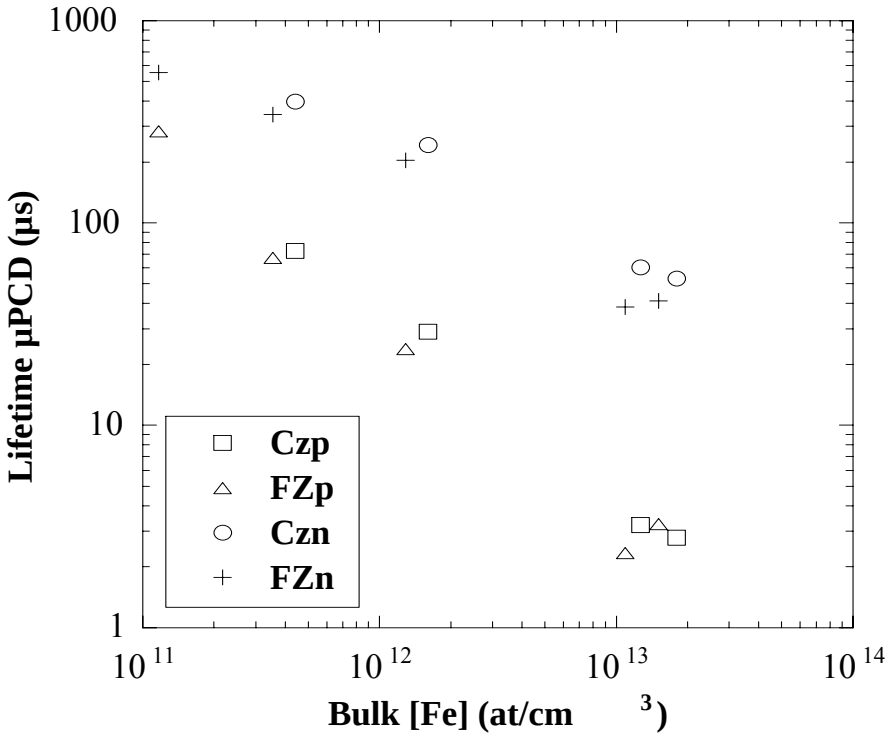

Figure 4.7: Minority carrier lifetime measured by μPCD as a function of the Fe bulk concentration after annealing at 900 ºC for 30 min in dry O_2. Different substrates, as described in Table 4.1, were used.[20] Reproduced by permission of The Electrochemical Society, Inc.

σ	Substrate				Ref.
(10^{-15} cm^2)	Czp	FZp	Czn	FZn	[31]
$\sigma_{e(FeB)}$	3.5±0.6	3.3±0.8	-	-	3.0
$\sigma_{e(Fei)}$	30.2±1.2	37.2±1.9	-	-	26.0
$\sigma_{h(Fei)}$	-	-	0.27±0.21	0.40±0.29	0.13

Table 4.3: Effective capture cross-section calculated for Fe traps in different substrates and their values for Cz and FZ material.[32]

literature is obtained which validates the assumptions made about Fe diffusion being similar in p-type and n-type Si. Interestingly, a strong dependence on the substrate doping type was found.[32] Fe_i is a most detrimental trap when present in p-type material as $\sigma_{e(Fei)}$ is one order of magnitude larger than the $\sigma_{e(FeB)}$ for the carrier injection levels studied. Also, it is clear that the Fe_i trap is more efficient as a recombination center for electrons than for holes,[33] as $\sigma_{e(Fei)}$ is two orders of magnitude larger than $\sigma_{h(Fei)}$. Even when paired with B, Fe in p-type material is more detrimental to the minority carrier properties than Fe in n-type silicon. This leads to the conclusion that tolerable levels of Fe contamination will be higher in n-type than in p-type silicon.

The impact of Cu on the MCLT of the p-type and n-type substrates is shown in Figure 4.8. No appreciable degradation of the minority carrier properties of the p-type material was observed for the whole range of Cu concentrations studied. On the other hand, surface Cu contamination higher than 10^{12} at/cm^2 driven into the substrates by annealing at 900 ºC for 30 min in dry O_2 is highly detrimental to the MCLT of n-type silicon in agreement with the results from literature.[30,34] Given its very high mobility and low solubility at low temperature (Figures

4.11 and 4.12) Cu is expected to pile-up at the SiO_2/Si interface with its redistribution and precipitation behavior during cool down being shown to be dependent on the substrate type.[35] Small and uniformly distributed precipitates are expected to form in the whole bulk of n-type silicon, whereas large colonies at the surfaces are found in p-type material.[34] These precipitates in the bulk region were related to the MCLT degradation of the n-type substrates.

Table 4.4 shows the Cu surface levels measured both before and after thermal processing. Oxidation ambient differences are similar to what was observed with Fe, i.e., wet oxidation tends to diffuse more of the metal contaminant away from the surface and into the bulk as compared to dry oxidation. Wafer doping type results in significant differences, regardless of oxidation ambient with p-type silicon showing much lower surface levels of Cu after annealing as compared to n-type. This is indicative of either a higher solubility of Cu in p-type silicon (unlikely) or an indication of significant differences in the precipitation behavior (possibly due to

Condition	Type	Pre	Post O_2	Post H_2+O_2
HF Control	p	0.0	0.0	0.0
0.1 ppb Cu	p	0.2	0.7	5.6
1.0 ppb Cu	p	0.8	24.0	6.5
10 ppb Cu	p	443.4	4.1	1.7
100 ppb Cu	p	2020.8	10.8	31.3
1000 ppb Cu	p	3616.2	100.6	39.3
HF Control	n	0.0	305.2	9.4
0.1 ppb Cu	n	1.0	35.5	92.1
1.0 ppb Cu	n	2.7	1882.2	1763.2
10 ppb Cu	n	119.7	100.3	94.4
100 ppb Cu	n	2522.3	2251.5	1190.9
1000 ppb Cu	n	8448.3	4732.2	1462.7

Table 4.4: Surface Cu levels measured with VPD-ICP-MS before and after 30 minute, 900 °C anneals in dry O_2 and wet H_2+O_2 ambients. The higher levels post anneal for the n-type control, 0.1 ppb and 1.0 ppb Cu conditions are strong indication of cross contamination during thermal processing.

differences in intrinsic defectivity of the p-type and n-type substrates used in this study). There is significant evidence of evaporative cross contamination occurring during the thermal process, as for the lowest starting conditions on both p-type and n-type substrates, the amounts of surface Cu seen are higher post anneal than pre anneal.

The recombination behavior of Fe and Cu in p-type and n-type material is better understood by evaluating the energy levels of the recombination centers that they introduce in the Si band gap (Figure 1.9). Centers near mid-band gap are more efficient recombination sites than the ones close to the band gap edges as they provide easy access for both holes and electrons to move between the valence and conduction bands.[32] Interstitial Fe introduces a single donor state in the Si bandgap at an energy of E_v+0.43 eV [31] very near the middle of the band gap (E_v+0.55 eV). In p-type Si at room temperature, however, Fe is paired with boron which creates a donor state at E_V+0.1 eV and possibly an acceptor state at E_c-0.23 eV.[32] This agrees with the observed activity of Fe in p-type and n-type silicon. The donor state generated by the Fe_i acts as a much more efficient electron recombination center than the one from the FeB pair and is more detrimental to the MCLT of p-type Si (Figure 4.6). The fact that Fe_i creates a donor state drastically reduces its efficiency as hole recombination center when present in n-type silicon as observed on Figure 4.7.

Copper is expected to be in substitutional sites in the Si matrix and it introduces a series of donor and acceptor levels in the silicon bandgap.[32] The presence of the different centers appears to depend on the thermal history of the sample which makes the analysis of the Cu recombination activity a complex task.[32] At low temperatures only a double donor state is observed at E_c-0.16 eV.[32] This would account for the negligible impact of Cu on the MCLT of p-type silicon (Figure 4.8) and the observed degradation of the minority carrier properties of n-type

material. However, multiple levels have been reported in the lower half of the Si bandgap at E_V+0.23 and E_V+0.45 eV that are highly dependent on annealing and cooling conditions.[32] These levels should have considerable influence on the MCLT of p-type and n-type material, however, no consensus has been reached on the value of their capture cross-section which makes it very difficult to predict their recombination activity and to compare it with the better established traps for Cu and Fe that have been discussed.[32] Moreover, precipitation appears to have a determining effect on the recombination behavior of Cu, affecting not only its distribution in the substrate,

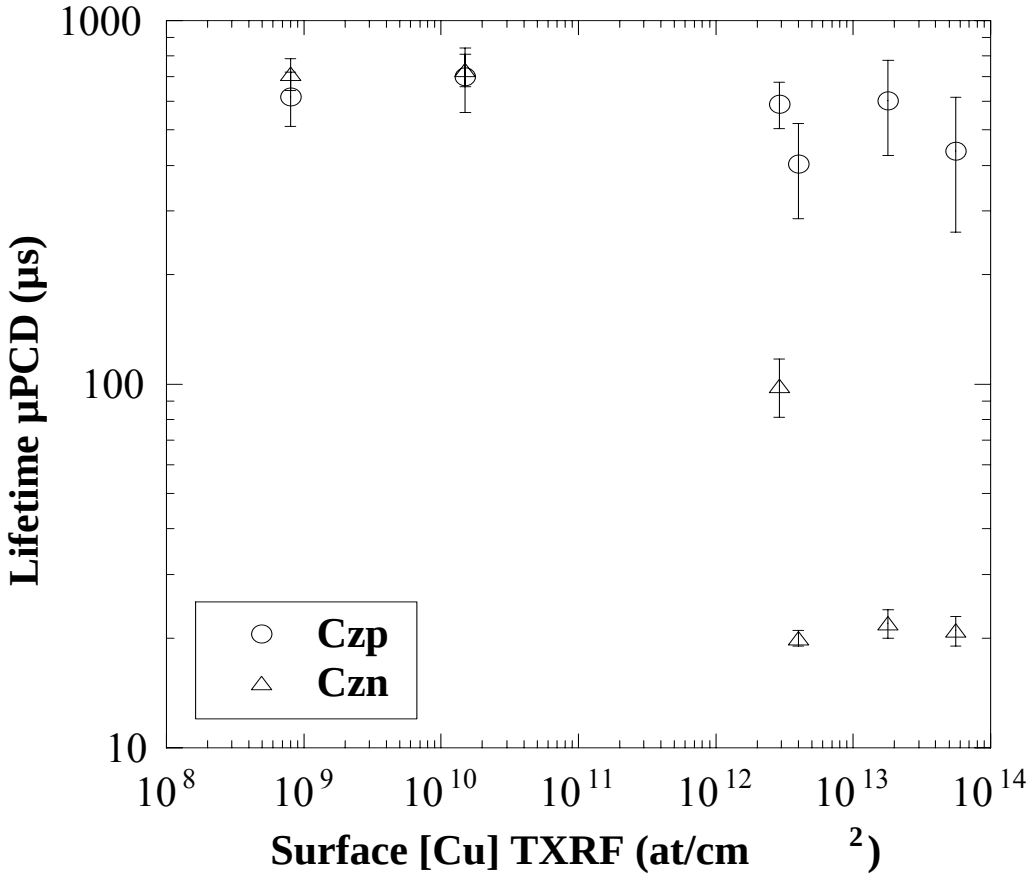

Figure 4.8: Minority carrier lifetime as measured by µPCD on p-type and n-type Cz substrates that have been surface contaminated different levels of Cu prior to annealing at 900 ºC for 30 min in dry O_2.[20] Reproduced by permission of The Electrochemical Society, Inc.

but also influencing its impact on the minority carrier properties of silicon. This should be strongly related to the threshold value observed in Figure 4.8 for MCLT reduction with Cu contamination.

4.4 Experimental for Metal Survey

For this portion of the study, both p-type (<100>, 6-10 Ωcm for surface analyses, and <100>, 10-12 Ωcm for MCLT/SPV analyses) and n-type (<100>, 10-15 Ωcm) type CZ wafers were contaminated by metal adsorption from 10% HNO_3 containing 10 ppm by weight of each metal using a spin on technique.[36] The metals chosen to test were: Ba, Bi, Co, Ir, Mo, Ni, Pb, Pt, Ru, Sr, Ta, W, and Zr. The reasons for the selection of each metal are shown in Table 4.5. The wafers were prepared beforehand by processing through a 1:1:5 SC1 at 65 °C for 10 minutes followed by a complete oxide removal (deglaze) in 0.49% HF for 10 minutes to produce a clean, hydrogen terminated surface. To facilitate metal adsorption on the surface, the wafers were all processed through a 1:4 H_2O_2:H_2SO_4 mixture (SPM or piranha clean) at 110 °C to ensure uniform, metal free, chemical oxide coverage on the surface. Wafers used for testing of minority carrier properties were pre-measured using μPCD (following HF passivation discussed in Section 4.2, cf. Figure 4.1) and SPV with all wafers having >200 μsec MCLT and >400 μm L. Bulk Fe concentration was measured on the p-type wafers using SPV (cf. Section 1.3.2, Equation 1.9). All wafers had $<5 \times 10^{10}$ at/cm^3 of Fe, except those used with Pt and Co which had $<1 \times 10^{11}$ at/cm^3. None of these levels were sufficient to cause serious impact on MCLT or L (cf. Figures 4.4 and 4.6)

After contamination, the wafers were then loaded into a vertical furnace and processed for 30 minutes at 800 °C in three different gas ambients: dry O_2, wet O_2+H_2 (pyrophoric), and

Metal	Reason for Interest
Ba, Sr, Pt, Ru	DRAM memory cells. BaSrTiO3 capacitor with Pt or Ru electrodes. Cu diffusion barrier (Ru).
Pb, Zr, Ir	Ferroelectric memory cells. PbZrTiO3 capacitor with Ir electrode.
Co, Ni	Metal silicides.
Bi, Ta	Ferroelectric memory cells. SrBiTaO3 capacitor.
Mo, W, Ta	Potential metal gate materials.

Table 4.5: Metals tested and why they were selected.

N_2. Intermingled with the contaminated wafers in the furnace were clean control wafers (p-type, <100>, 1-30 Ωcm) that were used for subsequent surface analysis to detect any cross contamination that occurred with each metal during the thermal process. Figure 4.9 shows the order of the loading, including key cross contamination monitor wafers and the flow of gas during the thermal cycle. Slots designated with a "P" or "N" contain p type and n type wafers respectively that were contaminated as described above. Slots designated with an "X" contained clean wafers that were used to monitor evaporative cross contamination in the furnace. Wafers X5, X13, and X21 were used to test front side contamination while wafers X4, X12, and X20 were used to test back side contamination. It should be noted that the back side contamination is always being measured from a p-type wafer. It was not felt that wafer doping would have any influence on evaporative processes. Only results of Ba on p-type wafers raised any doubts about the validity of this initial assumption.

	Gas Flow ----->																	
Process	Slots ---->																	
Dry O_2			N6	N5	N4	N3	N2	N1	X5	X4	P6	P5	P4	P3	P2	P1		
Wet O_2+H_2			N6	N5	N4	N3	N2	N1	X13	X12	P6	P5	P4	P3	P2	P1		
N_2	N8	N7	N6	N5	N4	N3	N2	N1	X21	X20	P8	P7	P6	P5	P4	P3	P2	P1

Figure 4.9: Stacking of P and N type contaminated wafers during 800 °C furnace anneal and location of cross contamination wafers (X).

4.5 Results and Discussion for Metal Survey

4.5.1 General Overview of Results

The amount of each metal detected on the surface of the contaminated wafers before and after thermal processing is shown in Table 4.6. Annealing ambient as well as doping type both play a role in the redistribution of each metal. As discussed in Section 4.1, metal redistribution can follow one of three paths: 1) remain at the surface, 2) evaporate, migrating around and/or out of the furnace in the gas phase or, 3) diffuse into the substrate.

In the case of option 1, it is interesting to note that very few metals (the ones shaded in gray) actually remain quantitatively at the surface. Evaporation is one possibility, given that this processing is occurring at 800 °C. A graph of vapor pressure versus temperature over the range of interest should provide some guidance. To generate the observed vapor pressure in atmospheres for a given metal, the empirical formula,[37]

$$\log(p/atm) = A + BT^{-1} + C\log T + DT^{-3} \qquad 4.3$$

was used, where T is temperature in K, and A, B, C, D are fitting parameters for each metal which are valid for vapor pressures of 10^{-15} to 10^{-3} atmospheres; dividing the output of this calculation by 760 gives the value in torr. Figure 4.10 shows a graph of vapor pressure versus temperature for each metal tested, except Bi, for which accurate fitting parameters are not available. At the temperature at which this test was run (800 °C) only Sr, Ba, Pb, Co, and Ni

Wafer	Pre	Dry P	Dry N	Wet P	Wet N	N_2 P	N_2 N
Ba	66.0	4.6	54.6	5.0	58.0	74.7	53.8
Bi	83.9	<DL	<DL	1.1	0.9	<DL	<DL
Co	256	27.1	30.9	28.3	34.5	55.4	72.4
Ir	74.3	5.5	7.4	<DL	<DL	32.1	44.9
Mo	516	9.9	191	4.1	5.0	28.4	?
Ni	242	102	111	126	114	124	165
Pb	51.8	<DL	<DL	<DL	<DL	<DL	<DL
Pt	128	0.2	0.9	15.2	1.8	97.8	57.6
Ru	224	<DL	<DL	<DL	<DL	<DL	<DL
Sr	186	182	192	172	187	155	175
Ta	237	244	260	160.5	142.2	239	269
W	360	352	397	29.5	6.9	395	382
Zr	1580	1850	1961	1867	1937	1592	2076

Table 4.6: Pre and Post anneal surface concentrations of each metal. All values in 10^{10} at/cm^2. Metals that remain completely at the surface are highlighted in gray.

have vapor pressures that are in the valid range for the equation used. All others are well below, as would be expected from an inspection of their melting and boiling points. Table 4.7 gives a comparison of melting and boiling points of Bi with those of Pb and Ba, indicating that its vapor pressure should be similar to them overall.

	Melting Point	Boiling Point
Pb	327	1755
Bi	544	1564
Ba	727	1870

Table 4.7: Melting and Boiling Points in °C for Pb, Bi, and Ba.

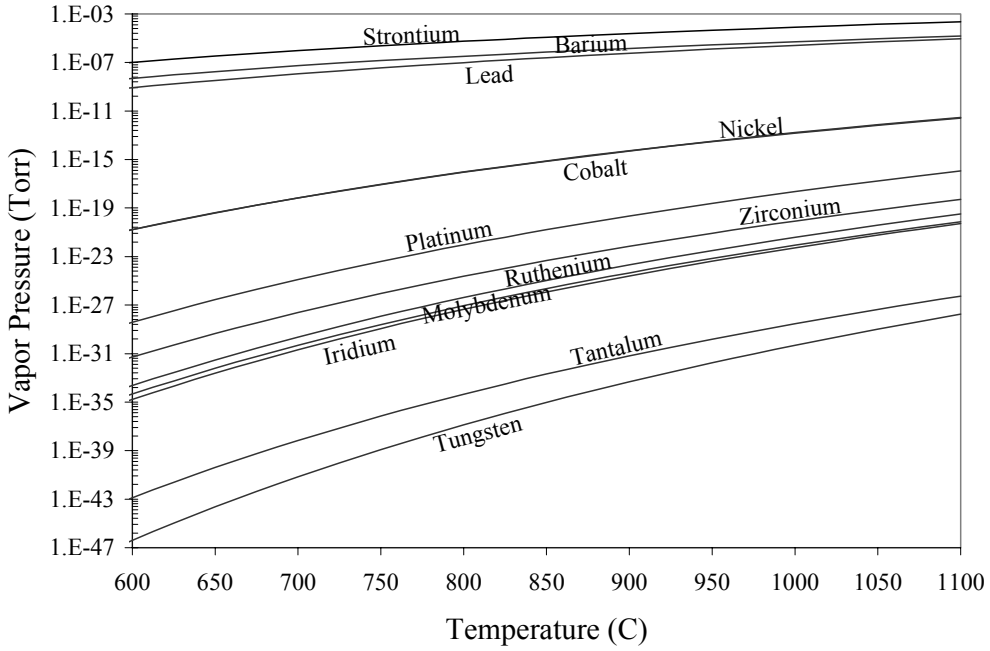

Figure 4.10: Calculated vapor pressure versus temperature over the range of interest. Note that Co and Ni lines are superimposed on one another.

Figure 4.10 would point towards diffusion into the silicon as being the primary route taken by the majority of the metals as, with the exceptions of Ba, Sr, Bi, and Pb, their vapor pressures are too low for them to have evaporated as metals during processing. Figures 4.11 and 4.12, graphing the Si diffusivity and solubility for the studied metals with empirical values from the literature, show that the 4d and 5d metals that are early in the transition series are the only ones without appreciable affinity for diffusing into the bulk of the silicon.[32] This correlates well to Table 4.6 with Ta, Zr, and W all being found remaining on the surface of the wafers under most annealing conditions. Ba and Sr are somewhat unexpected given their relatively high vapor pressures but the results would indicate that they are reacting to form oxides, silicates, or mixtures of both that are not as volatile as the metals themselves.

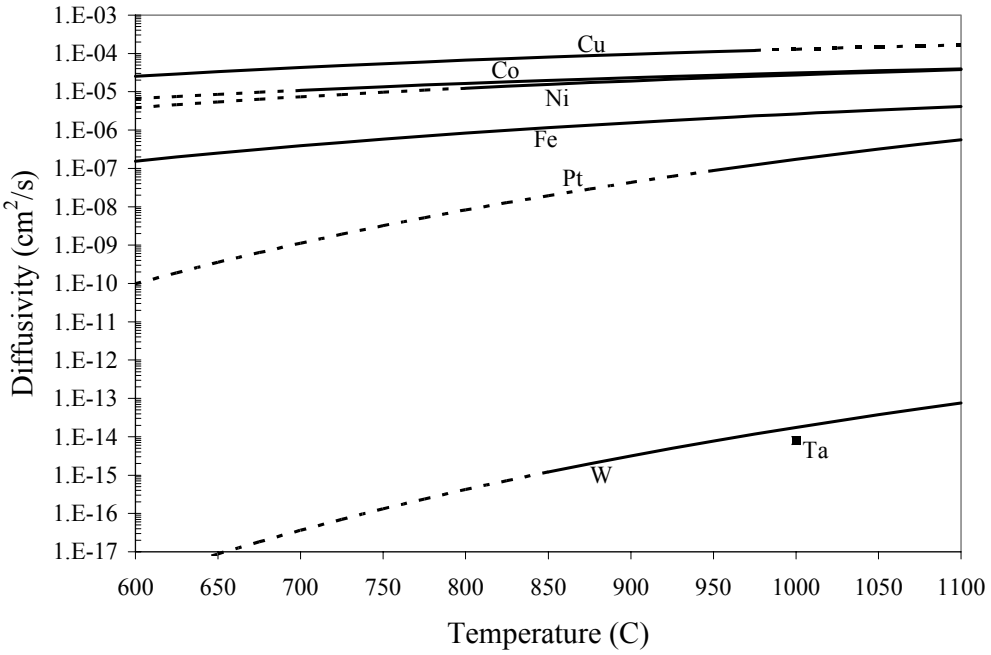

Figure 4.11: Diffusivity in silicon of various metals studied. Solid lines used in temp ranges where empirical equations are valid. Dashed lines are extrapolations.[32]

Cross contamination during annealing was tested by placing clean wafers in the furnace during anneal and then analyzing them for surface metals after anneal. The front sides of wafers placed between the contaminated wafers were measured by both TXRF and VPD-ICP-MS. In all cases, TXRF showed that metals were less than the detection limit of the technique, while VPD-ICP- MS analysis showed detectable levels of each metal, indicating that the cross contamination was primarily located near the edge of the wafer where TXRF cannot measure. This is consistent with the gas flow in the furnace and the path a metal would have to follow to get from the frontside of one wafer to the frontside of another wafer in the furnace. The backside

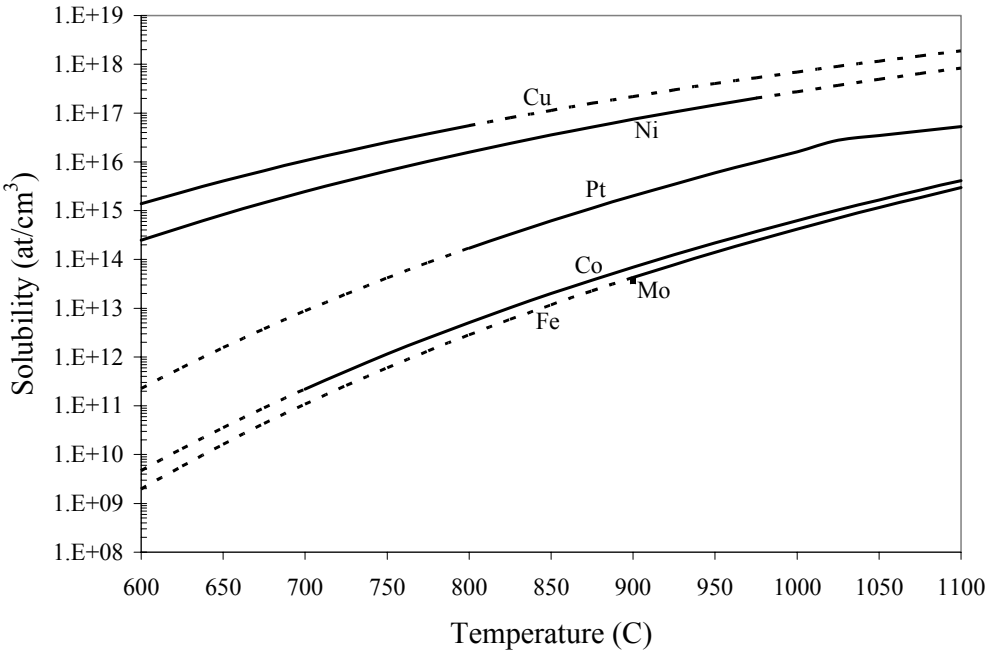

Figure 4.12: Solubility in silicon of various metals studied. Solid lines cover temperature range of empirical equation validity while dashed lines show extrapolation. The "kink" in the Pt solubility line is due to using two equations with exclusive temperature ranges.[32]

of wafers sitting in the middle of the contaminated wafers and whose backside was directly facing the metal contaminated front surface of a wafer in the next slot in the furnace were analyzed by VPD-ICP-MS as well (TXRF cannot measure the unpolished back surface of wafers). Ir, Pt, and Ru were not analyzed as they cannot be measured by this technique as discussed in Chapter 1. The VPD-ICP-MS results for both the contaminated and the cross contamination monitor wafers are shown in Table 4.8. Results are given as a percentage of the metal concentration on contaminated wafers before anneal. All detected cross contamination that was higher than 1% of the starting contamination level on the contaminated wafers was considered evidence of evaporation by a given metal.

	Pre	FSX Dry	FSX Wet	FSX N_2	BSX Dry	BSX Wet	BSX N_2
Metals	E10 at/cm^2	% of Pre	% of Pre	% of Pre	% of Pre	% of Pre	% of Pre
Ba	66.0	0.5	0.4	0.4	2.6	8.1	0.2
Bi	83.9	5.0	21.8	1.9	1.2	3.2	0.3
Co	256	43.6	8.6	0.0	2.8	1.4	0.0
Ir	74.3	<DL	<DL	<DL	NM	NM	NM
Mo	516	0.1	0.0	0.2	41.9	0.0	34.5
Ni	242	0.2	0.6	0.1	2.1	0.6	1.1
Pb	51.8	1.7	2.2	1.1	2.8	2.9	1.4
Pt	128	<DL	<DL	<DL	NM	NM	NM
Ru	224	<DL	<DL	<DL	NM	NM	NM
Sr	186	0.0	0.0	0.1	0.3	0.4	0.0
Ta	237	0.0	9.9	0.0	0.3	3.7	0.1
W	360	10.4	0.5	1.2	5.0	4.6	3.1
Zr	1580	0.1	0.1	0.1	0.4	7.2	0.0

Table 4.8: Percentage of starting surface concentration detected after anneal on: 1. contaminated wafers (Pre), 2. front sides (FSX) of cross contamination monitors and 3. back sides (BSX) of cross contamination monitors. NM means “not measured”.

A few conclusions become readily apparent from an examination of Table 4.8. The first is that almost all metals show evidence of evaporative transfer during anneal. The second is that the transfer from the front side of a contaminated wafer to the backside of its nearest neighbor is generally more efficient than transfer to the front side of a wafer downstream of it. Finally, with the notable exception of Mo, wet oxidation leads to a higher degree of cross contamination than either dry oxidation or annealing in an N_2 ambient.

The vapor pressures shown in Figure 4.10 indicate that in the case of metals like Mo, Ta, and W, evaporation is occurring via a species other than the metal atom as the vapor pressure of

the metal atoms is not high enough to result in the measured amount of evaporative cross contamination. Figure 4.13 plots the atomic evaporation rate of each metal versus temperature using a transform of the relationship developed by Langmuir:[38]

$$\varepsilon = 5.834 \times 10^{-2} \left(\frac{M}{T} \right)^{\frac{1}{2}} p^* \quad \text{g cm}^{-2}\,\text{s}^{-1} \qquad 4.4$$

where M is the molar mass, T is the temperature in K, and p* is the equilibrium pressure which in the case of an atmospheric furnace can be approximated as 760 Torr. Dividing this equation by the molar mass gives the evaporation rate as shown in Figure 4.13. This equation represents an ideal case of a pure metal in contact with a nonreactive atmosphere which is certainly not the case in this experiment. It does provide some rough insight into worst case evaporation rates at these temperatures though.

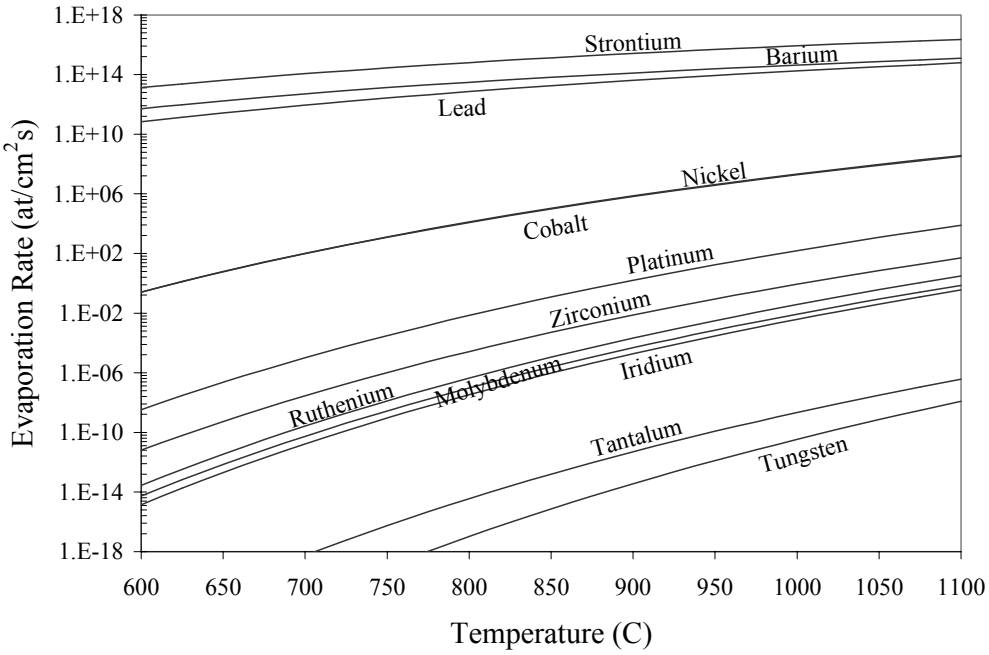

Figure 4.13: Calculated atomic evaporation rate versus temperature from equation 4.4.

For most of the metals, the evaporation rate is in the fraction of an atom per cm^2 per second. The only metals that would be thus expected to measurably cross contaminate based on this data would be Sr, Ba, Pb, and Bi (same reasoning as applied to vapor pressure) with Co and Ni being borderline cases. The contrary behavior of Ba, Sr, Mo, W, and Ta is a good indicator that chemical species other than the metal are involved. In the case of Ba and Sr, they are forming a product that reduces their volatility, while Mo, Ta, and W are apparently forming products that increase their volatility.

As discussed in Section 4.1, SPV and μPCD analysis provide an indirect measure of metal diffusion into the bulk of silicon wafers by quantifying their resultant degradation of minority carrier liftetime (MCLT) and minority carrier diffusion length (L). Both types of measurements were taken on wafers in this study and these results will be discussed next. A list of known electrically active defects and their capture cross sections is shown in Table 4.9 for the metals evaluated in this study. For SPV, all wafers were measured prior to being cleaned to verify that the substrates were of sufficient quality to merit further processing. They were then measured again following high temperature treatment. Figures 4.14 to 4.16 show the minority carrier diffusion lengths that were measured on p-type wafers pre and post anneal in dry O_2, wet O_2+H_2, and N_2 respectively. Figure 4.17 shows the minority carrier diffusion lengths measured with SPV on n-type wafers that were annealed in an N_2 ambient. As demonstrated in Section 4.3, Figure 4.5, the SPV technique is relatively insensitive to τ_{surf} and so provides a reliable, direct indicator of bulk silicon quality.

Following oxidation, whether dry or wet, L looks very similar in Figures 4.14 and 4.15. The results for most metals show some scatter and consistently only Pt and Ir show significant electrical activity, both causing severe degradation of L, with Ir consistently causing a larger

Metal	Interstitial / Substitutional	Donor / Acceptor	(eV)	σ (cm^2)
Ba	NA	NA	NA	NA
Bi	NA	NA	NA	NA
Co	s	d	Ev+0.41	5.0E-18
	s	a	Ec-0.41	2.2E-15
Cu	s	a	Ev+0.46	1.5E-14
	s	aa	Ec-0.16	1.9E-17
	s	d	Ev+0.22	3.0E-14
Fe	i	d	Ev+0.39	3.8E-17
FeB	i-s	a	Ec-0.27	1.6E-14
	i-s	d	Ev+0.10	6.4E-15
Ir	s	a	Ec-0.24	9.1E-15
	s	d	Ec-0.62	7.2E-14
Mo	i	d	Ev+0.28	6.0E-16
Ni	s	aa	Ec-0.07	5.4E-18
	s	a	Ec-0.41	1.2E-16
	s	d	Ev+0.17	5.4E-15
Pb	NA	NA	NA	NA
Pt	s	a	Ec-0.23	2.9E-14
	s	d	Ev+0.32	8.4E-15
	s	dd	Ev+0.08	3.5E-17
Ru	i?	a	Ec-0.14	1.1E-16
	i?	d	Ev+0.26	9.2E-16
Sr	NA	NA	NA	NA
Ta	i?	a	Ec-0.22	2.2E-17
	i?	d	Ec-0.58	>4E-15
	i?	dd	Ev+0.15	6.0E-17
W	i?	d	Ev+0.40	5.0E-16
Zr	i	a	Ec-0.13	>E-14
	i	d	Ec-0.42	>E-14
	i	dd	Ev+0.32	1.3E-17

Table 4.9: Electrically active defect centers and their capture cross sections as collected in Graf.[40]

overall decrease. Pt is known to be electrically active with a carrier recombination energy level near the middle of the Si band gap at E_v+0.32 eV (cf. with Fe_i at E_v+0.39 eV) with a capture cross section that is ~2 orders of magnitude larger than that of Fe (8.4 x 10^{-15} cm^{-1} vs 3.8 x 10^{-17} cm^{-1}). Ir creates two energy states at E_c-0.24 eV and E_c-0.62 eV, both of which have capture cross sections orders of magnitude higher than that of Fe_i (9.1 x 10^{-15} cm^{-1} and 7.2 x 10^{-14} cm^{-1}). Co and Ru, while being generally on the lower end of the distribution following anneal in dry and wet oxidizing environments only show up as being outside the distribution following N_2 anneal as shown in Figure 4.16. Consistent with the results seen with Fe in Figure 4.5, it is reasonable to expect that the results measured following N_2 anneal will be more precise as the measurement artifact that causes artificially high values of L to be measured by SPV will not be a factor.[27] All of the other metals either did not diffuse into the p-type silicon (unlikely for metals

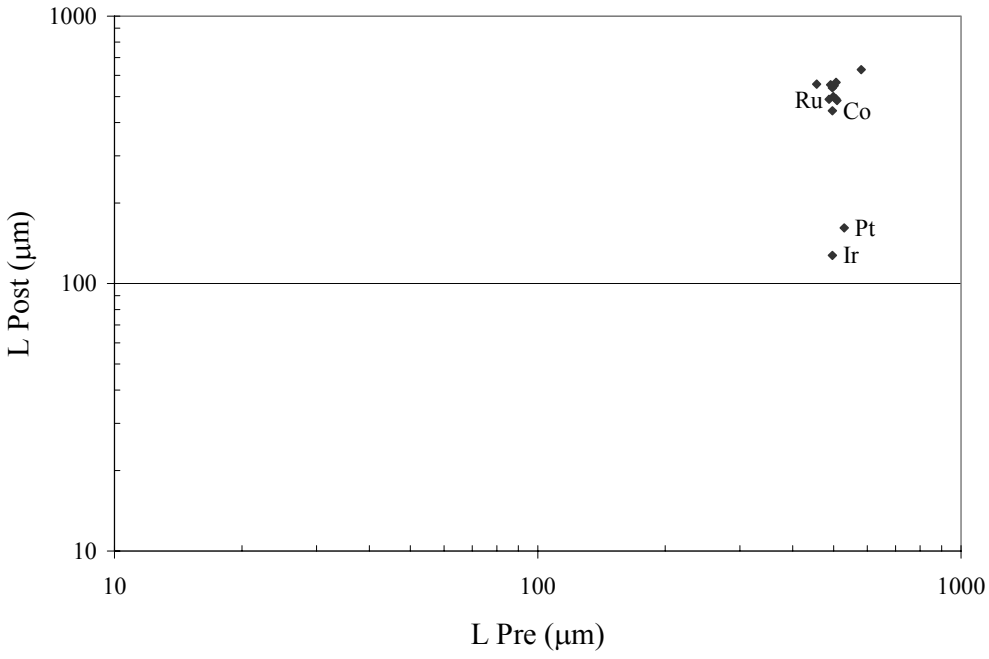

Figure 4.14: Graph of measured L in p-type wafers pre and post 30 minute, 800 °C thermal anneal in dry O_2 ambient.

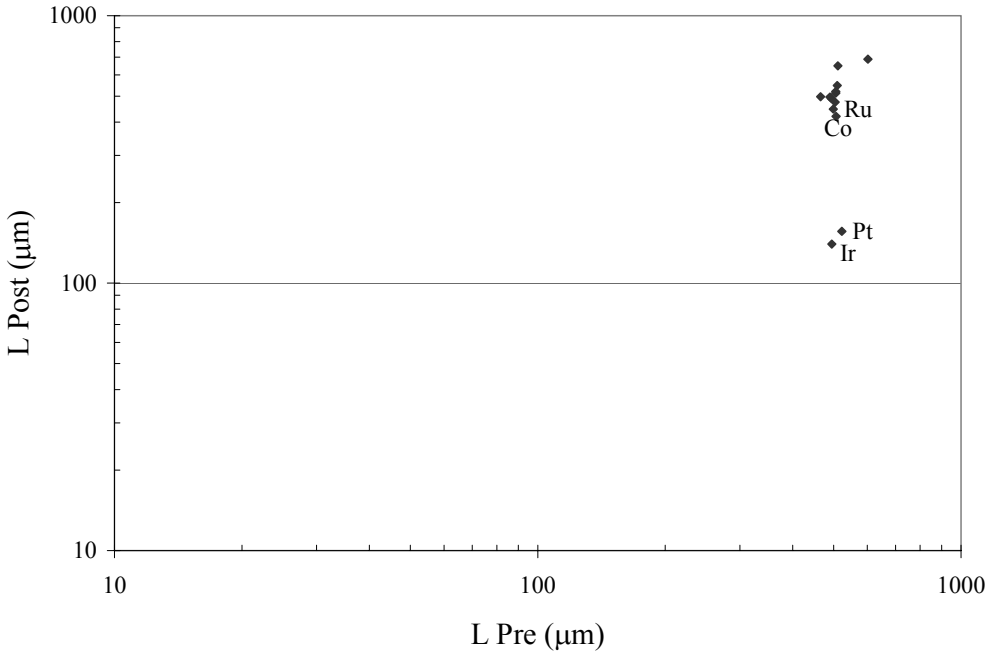

Figure 4.15: Graph of L in p-type wafers pre and post 30 minute, 800 °C thermal anneal in wet H_2+O_2 ambient.

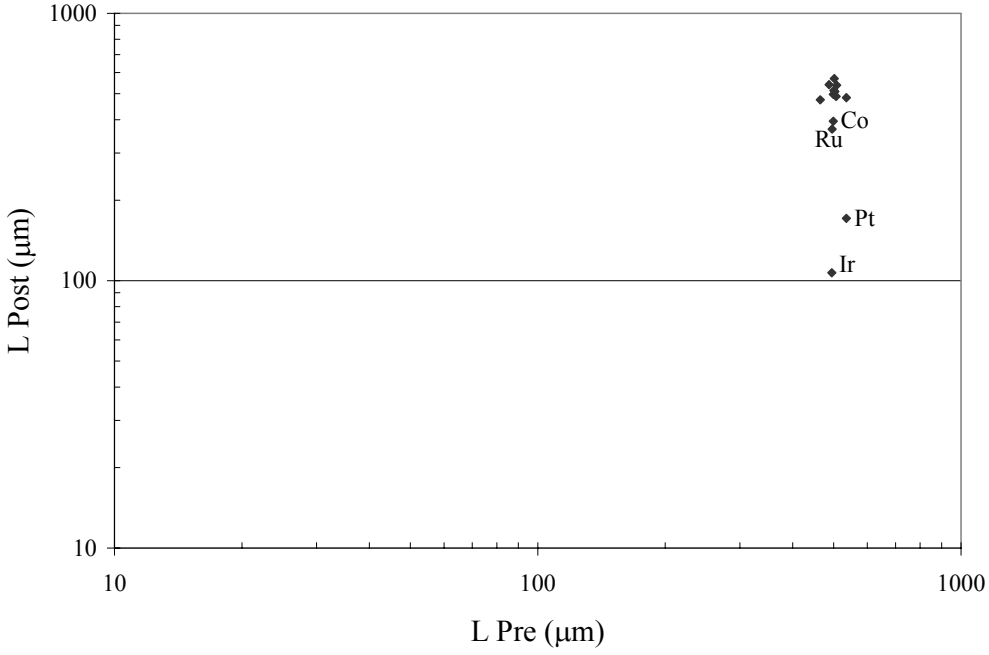

Figure 4.16: Graph of L in p-type wafers pre and post 30 minute, 800 °C thermal anneal in N_2 ambient.

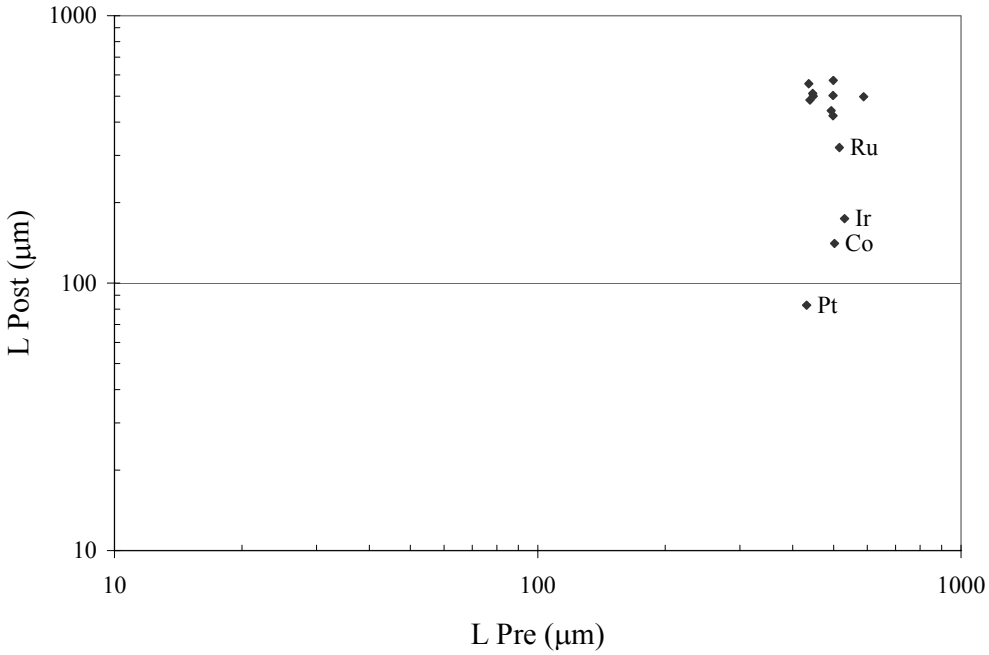

Figure 4.17: Graph of L in n-type wafers pre and post 30 minute, 800 °C thermal anneal in N_2 ambient.

like Co and Ni which are known to be medium/fast diffusers) or they did not form electrically active defects in the silicon under these annealing conditions (more likely).

Given the results on p-type wafers indicating that the N_2 annealed condition is the most sensitive for measuring the impact of metal contamination on L, only the n-type wafers that received N_2 anneal were measured by SPV. The results on n-type wafers are very similar to those on p-type wafers with the notable exceptions that Pt degraded L more than Ir and Co and Ru caused a much more significant degradation in L as compared to p-type. Co is likely due to its acceptor level at E_c-0.41 eV and Ru possibly due to its acceptor level at E_c-0.14 eV.

As clearly shown in Figure 4.3, MCLT as measured by the μPCD technique is very sensitive to τ_{surf}. With a poorly passivated wafer surface, it is impossible to measure MCLT values higher than ~10 μsec. This difference in the two techniques can be exploited to provide an

indirect measure of where low levels of metal contamination may be residing following thermal processes. For example, if L as measured by SPV is high for a given anneal condition and MCLT is high, that is a clear indication that both τ_{bulk} and τ_{surf} are high. If both are low, it is an indication that τ_{bulk} is low but no definite conclusion can be drawn about τ_{surf} as separating the two effects is nearly impossible. Neither of these conditions is very enlightening. It is the case where L measured by SPV is high and MCLT measured by μPCD is low that the situation becomes more interesting. In this situation, the high L equates to high τ_{bulk}, indicating that the metal in question is either not in the bulk or that it is not electrically active while the low MCLT equates to low τ_{surf}, indicating that the metal in question has to some extent been segregated to the oxide/silicon interface in quantities sufficient to cause poor passivation. Attention is now turned to the evaluation of MCLT results that were obtained on the wafers that were annealed in dry O_2 and wet O_2+H_2 ambients and which should have been high τ_{surf}. Figure 4.18 contains results for both p-type and n-type wafers after O_2 and O_2+H_2 annealing conditions. Figure 4.19 provides a compilation of SPV results from Figures 4.14 – 4.17 for easy comparison.

A comparison of Figures 4.18 and 4.19 shows that Co, Ru, Pt, and Ir, cause degradation in MCLT as would be expected from the degradation in L seen by SPV. It also shows that Ba, Sr, Pb, and Bi do not cause degradation in either parameter, which is consistent with the TXRF and VPD-ICP-MS results that indicate that Ba and Sr largely remain at/on surface in/on the oxide film while Pb and Bi have apparently evaporated during the thermal process (cf. Tables 4.6 and 4.8). Ni, Mo, Ta, W, and Zr all show that while they do not impact τ_{bulk}, they are definitely degrading τ_{surf} for both p-type and n-type substrates. Ni and Mo are both known to be medium to fast diffusers in silicon so it is not surprising that these metals could wind up segregating to the oxide/silicon interface during wafer cooldown. What is interesting is that Ta, W, and Zr are

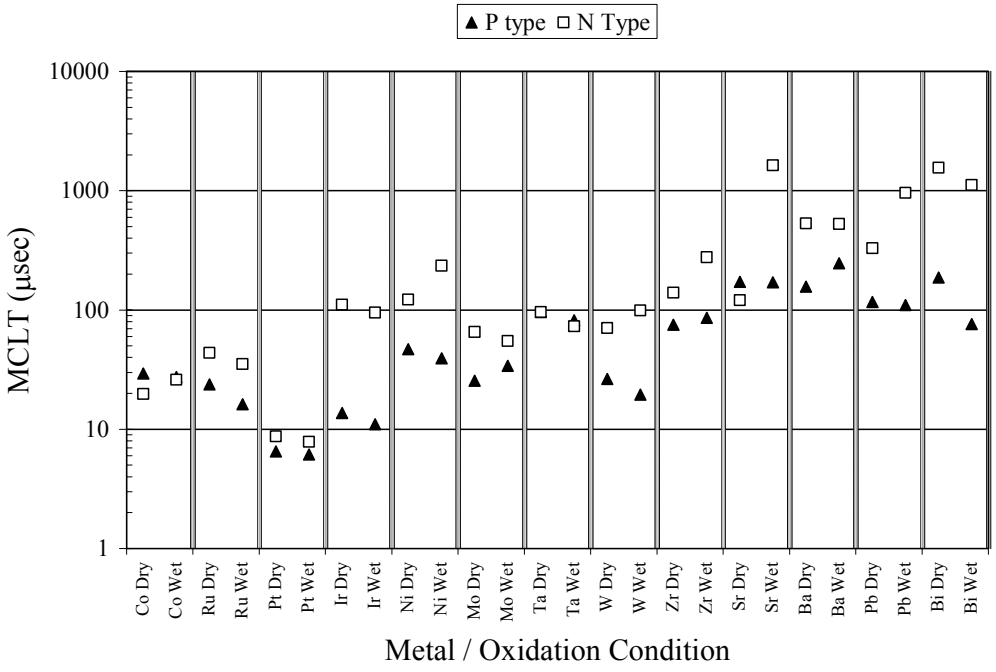

Figure 4.18: MCLT of metal contaminated wafers after 30 minute, 800 °C anneal in dry (O_2) or wet (O_2+H_2) ambients.

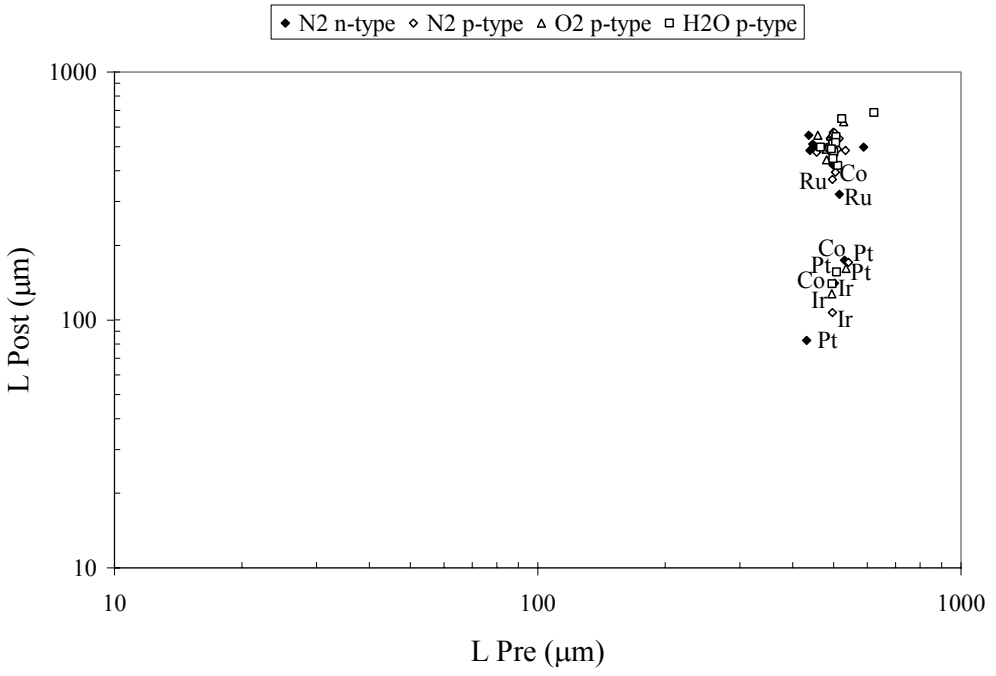

Figure 4.19: Compilation of all p-type and n-type SPV results from Figures 4.14 - 4.17.

showing degradation of interfacial properties. All three of these metals are known to be slow diffusers in Si and readily form oxides.[32] This offset between MCLT and L indicates that each of these metals reacts during the initial stages of the oxidation process and becomes trapped at the interface in sufficient quantities to cause degradation in τ_{surf}.

4.5.2 Consideration of Results Metal by Metal

4.5.2.1 Barium

Barium shows a strong tendency to stay on the wafer surface during thermal processing leading to the conclusion that at the annealing temperature investigated in this study, it preferentially reacts either with the native oxide present (N_2 anneal) or with the thermal oxide that is grown (whether dry or wet). This is in agreement with Boubekur who reported that after 60 minutes at 800 °C, Ba could be found almost quantitatively remaining on the surface.[39] This is also supported by its lack of impact on L in this work and on MCLT in this work as well as in Boubekur as it cannot impact bulk properties if it is not present in the bulk. This is also in agreement with papers reporting that, like the alkali metal Ca, Ba has a strongly negative impact on gate oxide integrity as it remains in the oxide film.[40,41] The one odd result in this study is that Ba was not detected on p-type surfaces following either dry or wet oxidation. This contradicts Boubekur who did not see any difference between p-type and n-type silicon during oxidation. Given his results showing that Ba remains primarily in the oxide, it indicates that the Ba in this study was either not deposited correctly to begin with or that something unknown and uncontrolled has impacted the results.

4.5.2.2 Bismuth

As expected, Bi evaporated during the annealing cycle. It was readily found on neighboring wafers and was not detected at all on the wafer surface after processing. This is the

first known test published using Bi so there is no known literature to compare these results to. Given its overall volatility and lack of impact on L or MCLT, it would appear to be a safe conclusion that Bi volatilizes during thermal cycling and is more likely to be a cross contamination threat than anything else.

4.5.2.3 Cobalt

The behavior of Co has been studied extensively in the literature with its solubility and diffusivity being well defined. It is known to form $CoSi_2$ at temperatures above 550 °C. Based on its high diffusivity and solubility, the results of this study would indicate that some portion of the metal evaporates during the early stages of the thermal process while the rest is trapped once the metal reacts with the surface and then diffuses into the bulk. Very little of it remains trapped in the oxide film while approximately twice as much remains near the surface following N_2 annealing. While creating energy levels near the middle of the band gap, Co has a minor impact on p-type L but has significant impact on n-type L. It degrades MCLT for both p-type and n-type wafers indicating that for p-type wafers some portion of the metal detected at the surface is trapped at the oxide/silicon interface. Due the degradation of L in n-type wafers, on firm conclusions about segregation to the interface can be drawn from the data in this study but it is reasonable to assume that similar behavior could be expected in n-type silicon. Using the equations 4.1 and 4.2 to convert L to τ_{SPV}, assuming that the energy level of interest is the E_v-0.41 eV trap with a capture cross section of 2.2×10^{-15} cm^2, and assuming that 100% of the Co not detected at the surface following the anneal resides in the bulk, it is possible to calculate a theoretical percentage of electrically active Co in the silicon matrix. Performing this calculation gives the result that in p-type Si, 3.3% of the Co is electrically active while in n-type Si, 28.5% is electrically active. Performing this same calculation using the energy level at E_c+0.41 eV gives

the result that approximately 10X more Co is in the wafer than it was initially contaminated with. This would indicate that the trap at E_v-0.41 eV is the one that is predominant in this case. This high percentage of electrically active Co in n-type silicon is very surprising as Co is known to almost quantitatively precipitate during cooling which results in very few Co atoms being in electrically active positions in the silicon matrix.[42]

4.5.2.4 Iridium

The results of this study indicate that Ir is likely to stay in or on the wafer following thermal processing at 800 °C. No evidence of evaporative transfer was detected while clear degradation of the L and MCLT was seen for all annealing conditions and for both p-type and n-type silicon. This is consistent with it forming stable substitutional defects in the silicon lattice, one of which is a donor level at E_c-0.62 eV and one of which is an acceptor level at E_v-0.24 eV.[43,44] Running the same calculations as was done with Co gives the interesting result that for either trap, the resultant percentage of active Ir in the silicon matrix is similar for both p-type and n-type doping. For the trap at E_c-0.62 eV, 6.5% is active in p-type silicon and 3.6% is active in n-type silicon. For the trap at E_v-0.24 eV, 51.8% is electrically active in p-type silicon and 28.1% is active in n-type silicon. Unlike the case of Co, this calculation does not allow for determination of which defect is dominant in controlling L and it is possible that both are playing a role. It is interesting to note that like Fe, wet oxidation appears to drive more of the Ir into the bulk as compared to dry oxidation. In a N_2 ambient, it can be seen that 50% or more of the Ir stayed within 100A of the surface (outer limit of TXRF probing depth). It is also interesting to note that in all cases, the Ir diffused most readily into p-type silicon as compared to n-type, indicating a possible preference for or reaction with B relative to P.

4.5.2.5 Molybdenum

There is limited literature reporting of the behavior of Mo in Si during high temperature processing. What there is indicates that its solubility is >3.6 x 10^{13} at/cm^3 at 900 °C and that it is a medium fast diffuser.[46] It has only one energy level in the lower half of the Si bandgap at E_v+0.28 eV with a $\sigma_e = 6 \times 10^{-16}$ cm^2 that is detectable only in p-type Si.[47] The impact on L is negligible which is in agreement with Aoki who saw only a minor impact on MCLT in p/p+ epitaxial silicon layers. As this work saw clear degradation of MCLT for p-type and n-type CZ wafers, the difference in results between Aoki and this work likely lie in different diffusion and segregation behaviors of Mo in CZ versus highly doped epitaxial wafers. Mo forms $MoSi_2$ when annealed at temperatures in the 500-1100 °C range but the activation energy for this reaction is 3.2eV as compared to 1.7eV for Fe or 1.4eV for Ni.[47] The high degree of cross contamination evident during the thermal anneal of Mo has not been reported elsewhere. In an oxidizing ambient at high temperature, it is likely that some portion of the Mo is being converted to MoO_3 which sublimes at 700 °C. This would be in competition with the Mo diffusing into the silicon substrate or reacting with the silicon oxide surface to form heteromolybdates or even silicomolybdic acid.[48] The difference between wet and dry oxidation may simply be due to where this balance lies in the two different ambients. Why the Mo migrates so readily from one wafer to another during N_2 anneal is more puzzling. The metal itself is not volatile (cf. Figure 4.10) so this could be taken as an indication either that Mo is capable of reacting with the chemical oxide to generate MoO_3 or that there was a low level of O_2 contamination present during temperature ramp that was sufficient to enable its formation.

4.5.2.6 Nickel

Like cobalt, nickel is one of the more thoroughly investigated 3d transition metals. It is known to be a fast diffuser with high solubility in Si at high temperature. It precipitates almost quantitatively during cooling and does not form a high concentration of electrically active defects. It readily forms $NiSi_2$ at temps above 750 °C and so it can be expected that the Ni detected at the surface in this study is likely in this form. Electrical activity would be expected to be minimal as the fraction of electrically active Ni in Si is about 1% of the respective solubility and the mid-bandgap energy level at E_c-0.39eV has a $\sigma_e = 5.6 \times 10^{-17}$ cm^2.[49,50] This is consistent with the lack of impact on L that was observed in this study. MCLT measurements indicate that some portion of the Ni that is measured at the surface after anneal is segregated to the oxide/silicon interface. Given that only very low levels of cross contamination were measured under all conditions, it is reasonable to assume that in the case of Ni, it primarily diffused into the Si.

4.5.2.7 Lead

There is very little known about the behavior of Pb in Si. It is known that it is a very slow diffuser in dielectric films and given its high volatility and the clear evidence of cross contamination, it is reasonable to conclude that Pb largely evaporated from the surface of the wafers and was exhausted along with the carrier gas.[51] No impact to L or MCLT was observed which is consistent with this conclusion.

4.5.2.8 Platinum

There has been a fair amount of literature on the behavior of Pt in Si and the results of this study are consistent with it. It is known to be a fast diffuser with relatively high solubility that forms silicides (Pt_2Si and PtSi) at temperatures above 300 °C.[52] It is also known to impact

minority carrier properties and is used to intentionally reduce MCLT in some applications. In this study it was seen to strongly degrade L and MCLT which is consistent with its known properties. Based on its high diffusivity, high solubility, degradation of L / MCLT and lack of cross contamination, it is reasonable to conclude that in this experiment, Pt diffused into the Si with only a negligible amount being evaporatively transferred to neighboring wafers. If it is assumed that the trap at E_v-0.23 eV is predominant in the n-type silicon and that the trap at E_c+0.32 eV is predominant in the p-type silicon, it can be calculated that the percentage of electrically active Pt is similar for both n-type and p-type wafers at 2.5% and 2.2% respectively. As with Ir, though, this calculation doesn't rule out either of the traps as contributing to the overall degradation in L and MCLT, so it is possible that both are contributing with differing efficiencies depending on doping. It has been reported in the literature that Pt can be gettered by phosphorous diffusion which may explain why in this study less Pt was seen on the surface of n-type wafers than on p-type wafers.[53]

4.5.2.9 Ruthenium

In this study, only limited conclusions can be drawn about Ru due to analytical difficulties. TXRF suffers from an interference with Cl which is ubiquitous and the VPD-DC technique cannot be applied due to ruthenium's highly positive electrode potential relative to Si. Very little literature has been published about Ru contamination in Si but, based on its position in the periodic table, it would be expected to be a medium diffuser.[54] It has been reported that Ru will form silicides at temperatures greater than 450 °C.[55] Very little electrical activity was detected in p-type silicon so it cannot be conclusively demonstrated with this data set if it all diffused into the p-type silicon or not, although MCLT was degraded as well which may be an indication of at least some metal residing at the near surface interface . However, a clear

degradation of n-type L was observed (likely due to the acceptor level at E_c-0.14eV) which is clear evidence that at least some portion of the Ru diffused into the bulk in the case of n-type silicon. It could be argued by extension that it is reasonable to think that it diffused into the p-type silicon as well. As with Ir, there are two energy levels that are potentially the source of the degradation in L that was seen in p-type and n-type wafers. If the level at E_c-0.14 eV is assumed to predominate in n-type silicon and the level at E_v+0.26 eV is assumed to predominate in p-type silicon, it can be calculated that while 89.6% of the Ru is electrically active in n-type silicon, only 8.1% is active in p-type silicon. These results are in agreement with the differences in degree of degradation that was observed for the different doping types.

4.5.2.10 Strontium

Sr was completely tied up in the oxide formed during oxidation and had no impact on minority carrier properties with both L and MCLT showing no serious effect due to the Sr contamination. This is consistent with its behavior reported in the literature where it was found to remain at/near the Si surface and to induce positive charges in silicon oxides.[53] As an alkaline earth metal like Ba and Ca, it has been implicated in causing premature breakdown of gate oxides.[40,41]

4.5.2.11 Tantalum

Tantalum is one of the slowest diffusing of all transition metals (slower than B or P), forming $TaSi_2$ above 550 °C, and so in this study would be expected to remain on or near the surface as was observed in the case of dry oxidation and N_2 annealing.[57] In the case of wet oxidation, there is clear evidence of evaporative loss of the Ta which is surprising given that it is a very high boiling point metal. No impact to L was observed while MCLT was degraded,

indicating some remained at the oxide/silicon interface. These minority carrier effects are consistent with its low solubility in Si and preference for oxide formation.

4.5.2.12 Tungsten

Similar to Ta, W is a very slow diffuser in Si, on the order of B and P, forming WSi_2 at temperatures above 650 °C. For this reason, it would be expected that it would stay at or near the surface of the wafer and have minimal impact on minority carrier properties under the typical conditions tested in this study. Consistent with this, it had no impact on L but showed degradation of MCLT, confirming that at most it partially remains at the oxide/silicon interface. What is most surprising is the fact that W is found at very low levels on the wafer surface following wet oxidation and that there is clear evidence of at least a low level of evaporative cross contamination. Potentially, like Mo which it is chemically similar to, it could be forming WO_3, which, with a melting point of 1473 °C should not be highly volatile but may be enough so to allow escape of the W over the course of the anneal, especially if the wet ambient is more capable of catalyzing the reaction than dry O_2 is.[58]

4.5.2.13 Zirconium

Zirconium is not expected to have a significant diffusivity in Si and there are indications in the literature that this is indeed the case.[59] While it is known to create electrically active defects when grown into Si ingots, it's low diffusivity would lead to the expectation that no impact on L would be observed which was indeed the case.[60] It is also known to easily form oxides and so would be expected to be found at or near the surface of the wafer after thermal processing in all cases and this is what is observed, both by TXRF and by its impact on MCLT. The fact that more Zr is consistently detected on the annealed samples relative to the control sample is likely due to variation in the starting levels of contamination on the wafers. One

interesting observation is the evidence of evaporative transfer of Zr during wet oxidation. This could potentially be happening during the temperature ramp phase, as $Zr(OH)_4$, which decomposes at 550 °C, might be formed and survive long enough to allow evaporation. It is also possible that ZrH_2 which is volatile, could be formed along with ZrS_2 (from the S in the chemical oxide formed by the final SPM clean prior to metal contamination).

4.6 Conclusions

The effects of trace amounts of Fe and Cu in p-type and n-type silicon were investigated with TXRF, microwave photoconductance decay (μPCD) and surface photovoltage (SPV). It was observed that the amount of Fe incorporated in the substrate from surface contamination is dependent on the annealing ambient with wet oxidation resulting in as much incorporation as N_2, while both incorporated significantly more than dry O_2. This diffusion behavior observed with bulk Fe concentration measurements with SPV was confirmed with TXRF surface analyses. The annealing ambient also affects the sample surface passivation, which is a critical parameter for measuring lowly contaminated wafers with μPCD. Treatment in HF solutions can be used to reduce the surface recombination velocity of the substrates permitting the study of non-annealed samples. The diffusion length is only accurately measured by standard SPV for values up to 0.7 times the wafer thickness. This limitation restricts the determination of the bulk Fe content by SPV to values higher than $5x10^{10}$ at/cm^3 in 150 mm wafers with a thickness of 650 μm. The μPCD and SPV techniques can be considered equivalent when samples are properly prepared as shown by the determination of equivalent effective capture cross-section of the Fe traps with both techniques.

Substrate doping type can have a strong impact on the recombination activity of metallic impurities. Fe, as expected, degrades the minority carrier properties in p-type substrates. On the

other hand, the impact of Fe on n-type silicon is at least one order of magnitude lower than on p-type. The tolerable limits for Fe contamination in bulk Si will therefor be best determined by the desired performance of p-type material. In contrast, Cu is highly detrimental to n-type material, but has no significant impact on the minority carrier properties of p-type silicon for contamination up to 5 x 10^{13} at/cm^2. Cu needs to be controlled if good properties are required on n-type silicon. Similar to Cu, Co was seen to be detrimental to n-type material while having only minimal impact on p-type at doping levels of 2.56 x 10^{12} at/cm^2. Pt and Ir were found to degrade minority carrier properties of both p-type and n-type silicon at levels of 1.28 x 10^{12} and 7.4 x 10^{11} at/cm^2, respectively, although Pt appears to be more detrimental to n-type than to p-type, based on impact to L.

	Behavior during thermal process			
Metal	**Surface?**	**Evaporate?**	**Diffuse?**	**Comments**
Ba	√	√		Remains almost completely at the surface. Small amount of cross contamination detected. Majority of metal gone from p type wafers. Presumed evaporated.
Bi		√		None detected at surface and no impact to L. Evidence of significant evaporation. Presumed to have completely evaporated.
Co	√	√	√	Predominantly diffused in, causing degradation in L (n type > p type). Evidence of varying amounts of evaporative cross contamination. 10-15% at surface after oxidation. 20-30% at surface after N2 anneal.
Ir	√		√	10% remains at surface after oxidation. 50% at surface after N2 anneal. No evidence of evaporation. Diffuses in and degrades L.
Mo	√	√	√	2-40% remains on surface, with wet oxidation leaving least on surface. Evidence of significant amount of evaporation. No impact to L but some diffusion into Si expected.
Ni	√	√	√	40-60% remains on surface. Evidence of low level of evaporation. Remainder assumed to have diffused into the bulk. No impact on L.
Pb		√		None detected at surface and no impact to L. Evidence of evaporation. Presumed to have completely evaporated.
Pt	√		√	Very little remains on surface after oxidation but 10-20% remains following N2 anneal. No evidence of evaporation. Diffusion into silicon confirmed by degradation of L.
Ru	?	?	√	None detected after anneal but detection limit was very poor. No evidence of evaporation but same detection limit problem. Diffusion into silicon confirmed by degradation of L.
Sr	√			100% remained on the surface. No evidence of evaporation or diffusion into the bulk.
Ta	√	√		Almost quantitatively remained at the surface. Significant evaporation detected during wet oxidation only. No impact to L and no diffusion expected.
W	√	√		Almost quantitatively remained at the surface. Significant evaporation detected during wet oxidation only. No impact to L and no diffusion expected.
Zr	√	√		Almost quantitatively remained at the surface with low level of evaporation detected during wet oxidation. No impact to L and no diffusion expected.

Table 4.10: Summary of metal behavior during thermal processing observed in survey study.

Finally, the experience gained working with Fe and Cu in detail was applied to a broad spectrum of metals. A summary of their behavior can be seen in Table 4.10. It was found that the behavior of these metals could largely be understood based on their diffusivity, solubility, and vapor pressure at the temperatures encountered during high temperature anneal. It was further seen that deviations from this expected behavior could be understood from reactions that could be expected to occur during processing. The major exceptions to this were the apparent evaporation of Ba from p-type wafers and the apparent evaporation of Ta and Zr during wet oxidation.

4.7 References

(1) Goetzberger, A.; Shockley, W. *J. Appl. Phys.* **1960** *31* 1821.

(2) Katz, L.E. *J. Electrochem. Soc.* **1974** *121* 969.

(3) Busta, H.H.; Waggener, H.A. *J. Electrochem. Soc.* **1977** *124* 1424.

(4) Ward, P.J. *J. Electrochem. Soc.***1982** *129* 2573.

(5) Miyazaki, M.; Sano, M.; Sumita, S.; Fujino, N. *Jpn. J. Appl. Phys.***1991** *30* L295.

(6) Miyazaki, M.; Miyazaki, S.; Kitamura, T.; Aoki, T.; Nakashima, Y.; Hourai, M.; Shigematsu, T. *Jpn. J. Appl. Phys.***1995** *34* 409.

(7) Graff, K.; Pieper, H. *J. Electrochem. Soc.* **1981** *128* 669.

(8) Weber, E.R. *J. Appl. Phys.* **1983** *A30* 1.

(9) Hourai, M.; Murakami, K.; Shigematsu, T.; Fujino, N.; Shiraiwa, T. *Jpn. J. Appl. Phys.***1989** *28* 2413.

(10) Jastrzebski, L.; Henley, W.; Nuese, C.J. *Solid State Technol*, **1992** *35* 27.

(11) Ohmi, T.; Imaoka, T.; Sugiyama, I.; Kezuka, T. *J. Electrochem. Soc.* **1992** *139 (11*) 3317.

(12) Hiraiwa, A.; Itoga, T. *IEEE Trans. on Semicond. Manufact.* **1994** *7 (1)* 60.

(13) Mertens, P.W.; Meuris, M.; Verhaverbeke, S. ; Heyns, M.M.; Schnegg, A.; Gräf, D.; Philipossian, A. *Proc. of the 38th Annual Tech. Meeting of the Institute of Environmental Sciences;* IES: Mount Prospect, IL 1992; p 475.

(14) Henley, W.B.; Jastrzebski, L.; Haddad, N.F. *Mat. Res. Soc. Symp. Proc.* **1993** *315* 299.

(15) Materials and Bulk Processes Roadmap, Semiconductor Industry Association, 1994.

(16) Lang, D.V. *J. Appl. Phys.* **1974** 45 3023

(17) Jastrzebski, L.; Milic, O.; Dexter, M.; Lagowski, J.; DeBusk, D.; Nauka, K.; Witowski, R.; Gordon, M.; Persson, E. *J. Electrochem. Soc.* **1993** *140 (4)* 1152.

(18) Ryuta, J.; Yoshimi, T.; Kondo, H.; Okuda, H.; Shimanuki, Y. *Jpn. J. Appl. Phys.* **1992** *31 (8)* 2338.

(19) Neumann, C.; Eichinger, P. *Spectroch. Acta* **1991** *46B (10)* 1369.

(20) Rotondaro, A.L.P.; Hurd, T.Q.; Kaniava, A.; Vanhellemont, J.; Simoen, E.; Heyns, M.M.; Claeys, C. *J. Electrochem. Soc.* **1996** *143 (9)* 3014.

(21) Zoth, G.; Bergholz, W. *J. Appl. Phys.* **1990** *67 (11)* 6764.

(22) Kitagawara, Y.; Yoshida, T.; Hamaguchi, T.; Takenaka, T. *J. Electrochem. Soc.* **1995** *142 (10)* 3505.

(23) Yasaka, T.; Takakura, M.; Sawara, K.; Uenaga, S.; Yasutaka, H.; Miyazaki, S.; Hirose, M. *IECE Trans. Electron.*, **1992** *E75-C (7)* 764.

(24) Mertens, P.W.; Rotondaro, A.L.P.; Meuris, M.; Schmidt, H.F.; Heyns, M.M.; Gräf, D. *Proc. of the 40th Annual Techn. Meeting of the Institute of Environmental Sciences;* IES: Mount Prospect, IL 1994; p 325.

(25) Stephens, A.W.; Aberle, A.G.; Green, M.A. *J. Appl. Phys.* **1994** *76 (1)* 363.

(26) Kaniava, A.; Menczigar, U.; Vanhellemont, J. ; Poortmans, J.; Rotondaro, A.L.P.; Gaubas, E.; Vaitkus, J.; Köster, L.; Gräf, D. *Mat. Res. Soc. Symp. Proc.* **1995** *386* 389.

(27) Lagowski, J.; Kontkiewicz, A.M.; Jastrzebski, L.; Edelman, P. *Appl. Phys. Lett.*, **1993** *63 (21)* 2902.

(28) Lagowski, J.; Edelman, P.; Kontkiewicz, A.M.; Milic, O.; Henley, W.; Dexter, M.; Jastrzebski, L.; Hoff, A.M. *Appl. Phys. Lett.* **1993** *63 (22)* 3043.

(29) Zoth, G.; Bergholz, W. *Electrochem. Soc. Symp. Proc*.; Electrochem. Soc.: Pennington, NJ 1991; p 643

(30) Naito, S.; Nakashizu, T. *Mat. Res. Soc. Symp. Proc.* **1992** *262* 641.

(31) Hourai, M.; Naridomi, T.; Oka, Y.; Murakami, K.; Sumita, S.; Fujino, N.; Shiraiwa, T. *Jpn. J. Appl. Phys.* **1988**, *27 (12)* L2361.

(32) Graff, K. *Metal Impurities in Silicon-Device Fabrication*; Springer-Verlag: Berlin, 1995.

(33) Hangleiter, A. *Physical Review B*, **1987** *35 (17)* 9149.

(34) Zhong, L.; Shimura, F. *Appl. Phys. Lett.* **1992** *61 (9)* 1078.

(35) Bai, P.; Yang, G.-R.; Lu, T.-M. *J. Appl. Phys.* **1990** *68 (7)* 3313.

(36) Hourai, M.; Naridomi, T.; Oka, Y.; Murakami, K.; Sumita, S.; Fujino, N.; Shiraiwa, T. *Jpn. J. Appl. Phys*. **1988** *27* L2361.

(37) Alcock, C.B.; Itkin, V.P.; Horrigan, M.K, *Canadian Metallurgical Quarterly*, **1984** *23* 309.

(38) Langmuir, I. *Physic Z.* **1913** *14* 1273

(39) Boubekur, H.; Höpfner, J.; Mikolajick, T.; Dehm, C.; Ryssel, H. *J. Electrochem. Soc.* **2000** *147* 4297.

(40) Bearda, T.; de Gendt, S.; Loewenstein, L. ; Knotter, M. ; Mertens, P. ; Heyns, M. *Fourth International Symposium on Ultra Clean Processing of Silicon Surfaces;* Scitec Pulbications, Ltd.: Zuerich-Uetikon, Switzerland 1999; p 11.

(41) Mertens, P.W.; Bearda, T.; Loewenstein, L.M.; Martin, A.R.; Hub, W.; Kolbesen, B.O. Teerlinck, I.; Vos, R.; Baeyens, M.; de Gendt, S.; Kenis, K.; Heyns, M.M. *Defects in Silicon III PV 99-1;* Electrochemical Society: Pennington, NJ 1999; p 401.

(42) Graff, K. *Metallic Impurities in Silicon Device Fabrication 2nd Ed.*; Springer-Verlag: Berlin 2000; p 145

(43) Lemke, H. *Semiconductor Silicon 1994*; Electrochem. Society: Pennington, NJ 1994; p 695.

(44) Lisiak, K.P.; Milnes, A.G. *Solid State Electron.* **1976** *19* 115.

(45) Graf, K. ibid. p 106.

(46) Nicolet, M.-A.; Lau, S.S. V*LSI Electronics;* Academic Press: New York 1983; p 330.

(47) Aoki, M.; Itakura, T.; Sasaki, N. *Japn. J. Appl. Phys.* **1995** *34* 712.

(48) Lewis, R.A. Sr. *Hawley's Condensed Chemical Dictionary 14th E.*; Wiley Interscience: New York 2001; p 759.

(49) Graff, K.; Heim, P.; Pieper, H. *J. Electrochem. Soc.* **1994** *141* 2821.

(50) Lemke, H. Ibid.

(51) Jones, R.E. *Integrated Ferroelectrics*, **1995** *6* 81.

(52) Graff, K. Ibid., 117.

(53) Falster, R. *Appl. Phys. Lett.* **1985** *46* 737.

(54) Lemke, H. Ibid.

(55) Arunagiri, T.N.; Zhang, Y.; Chyan, O.; El-Bounani, M.; Kim, M.J.; Chen, K.H.; Wu, C.T.; Chen, L.C. *Appl. Phys. Lett.* **2005** In Press.

(56) Yamamichi, S.; Muramatsu, Y.; Lesaicherre, P.-Y.; Ono, H. *Japn. J. Appl. Phys.***1995** *34* 5188.

(57) Graf, K. Ibid. 157.

(58) Lewis, R.A. Ibid. 1144.

(59) Quevedo-Lopez, M.A.; El-Bouanani, M.; Gnade, B.E.; Wallace, R.M. *J. Appl. Phys.* ***2002*** *92* 3540.

(60) Lemke, H. *Phys. Status Solidi* **1990** *122* 617.

CHAPTER 5

RUTHENIUM AS A PLATEABLE DIFFUSION BARRIER FOR COPPER

5.1 Introduction

The speed of a signal through the interconnect levels of a device is degraded by both the resistance of the metal used as well as by the capacitive charging of the dielectric lying between the metal lines. The product of the electrical resistance of the metal lines (R) and the capacitance of the dielectric (C) between them (RC) must be minimized if signal speed is to be maximized. This is what has driven the semiconductor industry's migration from Al to Cu for metallization and from silicon oxide to fluorine doped oxide and finally to carbon doped oxide for the intermetal dielectric.

As was discussed in Chapter 1, an integral part of the Cu dual damascene integration process is the conductive diffusion barrier that is used to prevent Cu from penetrating into the surrounding dielectric. It is essential to prevent this penetration as Cu will readily migrate through dielectrics when placed under bias. Beginning with the 180 nm node and continuing through the 130 nm, 90 nm, and 65 nm nodes, the diffusion barrier of choice has been TaN or Ta/TaN bilayers deposited by physical vapor deposition (PVD).[1,2] The relatively high overall bulk resistivity of Ta/TaN (ρ=13 $\mu\Omega$.cm for Ta) necessitates that a PVD Cu film must be used to act as a conductive seed layer for subsequent electrochemical deposition (ECD) of bulk Cu. For 65 nm processing, the thickness of the barrier layer stack is on the order of 10nm on the sides and 30 nm on the bottom while the seed layer is on the order of 60 nm on the bottom and 20 nm on the sides. Given that the smallest feature sizes being filled are ~100 nm wide and ~160 nm deep at metal 1, it is readily apparent that: 1) the higher resistivity barrier is now consuming up

to 20% of the total linewidth and 2) the combination of barrier/seed layer is creating very high aspect ratio structures for the ECD process to fill (>3:1).

This situation creates multiple issues for Cu integration as semiconductor technology moves into the 45 nm node. The first is that an increasing percentage of the total linewidth is being occupied by a higher resistivity barrier with a correspondingly decreasing percentage being occupied by the lower resistivity Cu (ρ_{eff}=2.2 μΩ.cm).[3] The second is that ever increasing aspect ratios are being encountered which creates significant challenges for manufacturing process technology. One approach that would be very useful would be to utilize a barrier metal this is both an effective diffusion barrier for Cu and which has a low enough bulk resistivity that it could serve as a seed layer for the ECD process. This would maximize the percentage of Cu in the metal line and result in lower aspect ratio structures needing to be filled.[3,4,5]

Ruthenium (Ru) potentially provides just such a solution. It is an air stable transition metal with nearly twice the electrical conductivity of Ta (Ru bulk resistivity ρ=7.1 μΩ.cm vs. ρ=13 μΩ.cm for Ta). More importantly, Ru, like Ta, shows negligible solid solubility with Cu even at 900 ˚C.[6] In a recent report, it has been proposed that Ru shows promise of not only being an effective Cu diffusion barrier but also affords direct Cu electroplating without the need of an additional Cu-seed layer.[7]

In this chapter, a 20 nm thick sputter deposited Ru film on a silicon substrate will be evaluated for its suitability as a Cu diffusion barrier that can be directly plated upon. Adhesion between Cu/(20 nm Ru)/Si will be tested by scribe and tape-peel testing before and after thermal annealing. Secondary ion mass spectroscopy (SIMS) profiling and transmission electron microscopy (TEM) will be used to test its diffusion barrier properties up to 450 ˚C. Finally, preliminary electrochemical data will show direct Cu plating with good efficiency can be

achieved on an ultra-thin (< 20 nm) Ru film. Scanning electron microscopy (SEM) images will show uniform Cu plating coverage on Ru without agglomeration

5.2 Experimental

Ruthenium (99.95% pure) was deposited on a pre-cleaned Si wafer using a magnetron sputtering system with a base pressure at 1×10^{-8} torr. The Ru film thickness was measured by cross-sectional high-resolution transmission electron microscopy (HRTEM). Copper (99.99% pure) was deposited on the Ru/Si sample in one of two ways. For the barrier diffusion study, it was deposited via thermal evaporation. For the electrochemical studies, high purity copper sulfate and sulfuric acid were used to make all electrolyte solutions in ultra-pure water (18.2 MΩ). Electroplating was performed using an EG&G Model M 273 potentiostat/galvanostat. A conventional three-electrode cell with a Pt sheet as the counter electrode and silver/silver chloride (3 M NaCl) as the reference electrode was employed. The Cu/Ru diffusion test samples were annealed in vacuum at $< 4 \times 10^{-6}$ torr. SEM imaging was done with a JEOL JSM-T300 electron microscope. HRTEM analysis was carried out on a Philips CM200FEG TEM. Optical images were recorded using a Nikon ME600L microscope. SIMS depth profiling from the wafer back-side was performed using a Cameca 6f SIMS spectrometer. An oxygen beam with an 8 keV impact energy was rastered over a 200×200 μm^2 region and the secondary ion signals were collected from the center of the sputtered area over an area with a 60 μm diameter. The back side of the Si substrate of Cu/Ru/Si samples was carefully polished to within 1-2 μm by a standard mechanical polishing procedure.[8]

5.3 Results and Discussion

5.3.1 SIMS depth-profiling

The sputter deposited Ru thin film has a mean roughness of ~2 nm based on the HRTEM cross sectional measurement. Following PVD Cu deposition, the Cu/Ru/Si samples were annealed with progressively increasing temperatures under vacuum. The stability of the Cu/Ru/Si interface after annealing was then studied using dynamic SIMS depth profiling analysis.[9.10] The inter-diffusion of atoms across the interface between the Cu and Ru and chemical reactions between layers, are revealed by any changes in the secondary ion intensity of the metals that occur at the interface between the two metals. Comparison with appropriate control samples can then establish the extent of inter-diffusion and thereby the efficiency of the diffusion barrier. When significant diffusion occurs, this technique can easily establish the resultant diffusion kinetics.[11,12,13] A potential pitfall of this approach is that that the SIMS technique itself can cause mixing of the metals at the interface (known as knock-on). The primary ion beam used to create the secondary ions can impart enough kinetic energy to drive Cu atoms from the surface that is being analyzed into the underlying Ru layer, thus creating an erroneous impression of thermal inter-diffusion. As the evidence of Cu inter-diffusion that is being tested for is the existence of Cu under the Ru film, a backside SIMS technique was employed. In this technique, the substrate is physically polished from the back to an extent that a subsequent SIMS profile from the back side (from Si through Ru to Cu) can detect the presence of diffusing species without spurious knock-on artifacts.

The interfaces of the as deposited Cu/Ru/Si samples, as well as after 10 minute vacuum anneal at 450 ^{o}C and 550 ^{o}C are shown in Figure 5.1. The lateral distribution of Si, Ru and Cu are shown as a function of sputtering depth based on Si. The atomic concentration is calculated

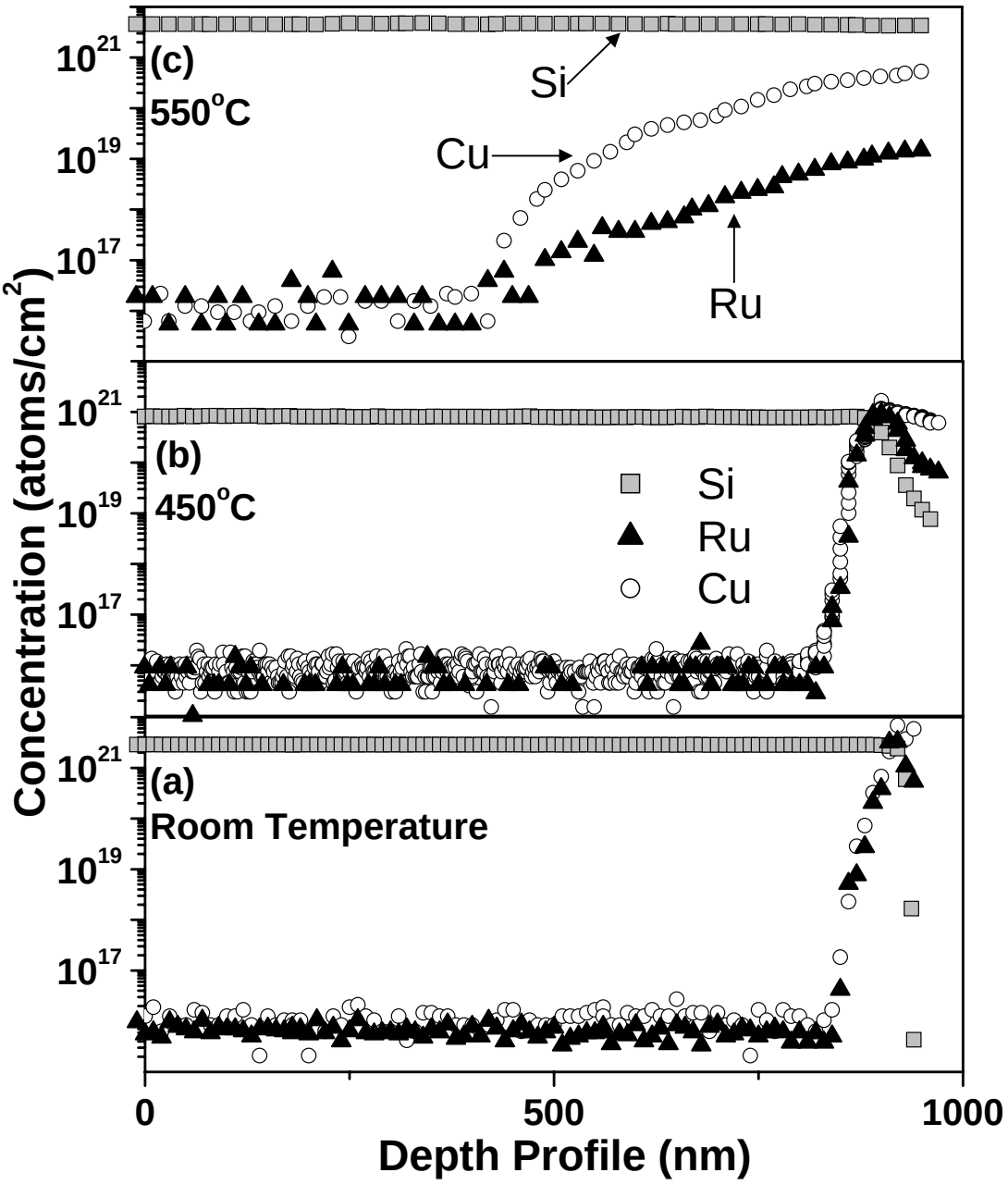

Figure 5.1: Back-side SIMS depth profiles for Cu/(~20 nm Ru)/Si samples: (a) as prepared, (b) after 450 °C annealed, 10 min, (c) 550 °C annealed, 10 min,. Cu diffusion into Si substrate only seen for 550 °C anneal.

from the secondary ion intensity using a relative sensitivity factor for elemental Cu. Initially, the Si secondary ion intensity signal originating from the Si substrate dominates the SIMS profiling with negligible Cu and Ru background signals, as expected. After profiling through the pure Si substrate (~1 μm thick) before and after annealing at 450 ^{o}C, the Si signal begins to drop rapidly with sputtering time and the Cu and Ru signals increase. The Ru and Cu signals show a peak profile that is consistent with a thin Ru/Cu film deposited on the Si substrate. Depth profiling was stopped when the Cu signal approached 10^{21} atoms/cm^3, to avoid Cu contamination of the SIMS instrument between successive profiles. As shown in Figure 5.1b, the interface of the Cu/Ru/Si structure remains well defined after vacuum annealing at 450 ^{o}C for 10 min and indicates no detectable Cu penetration into the Si substrate. The results suggest that the 20 nm Ru thin film impedes the Cu inter-diffusion into the Si substrate. In contrast, the SIMS depth profile for a 550 ^{o}C vacuum annealed Cu/Ru/Si sample, Figure 5.1c, clearly shows both Cu and Ru penetration into the Si substrate for at least 400 nm.

5.3.2 TEM Cross-sectional Imaging

The depth resolution of the SIMS profiling technique limits its ability to distinguish the sequence of the deposited Ru and Cu films precisely, hence the SIMS signals overlap. Additionally, the inherent ion beam mixing effect tends to broaden the apparent width of Ru barrier layer. TEM cross-sectional imaging therefore was utilized to examine the microstructure and physical arrangement of Cu/Ru/Si samples after annealing. As shown in Figure 5.2a, the sputter deposited Ru film is about 20-22 nm thick with a columnar microstructure oriented vertically with respect to Si substrate. The as deposited PVD Cu film consists mainly of less densely packed small Cu grains. In comparison, the TEM image of the 550 ^{o}C annealed sample, Figure 5.2b, shows delamination of the Ru film and Cu penetration into Si substrate that

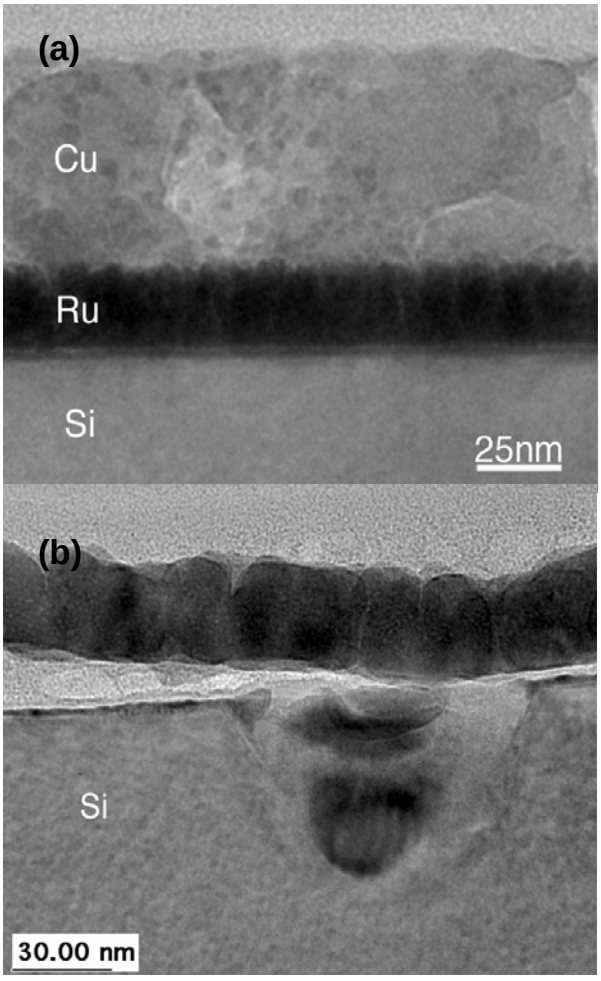

Figure 5.2: Cross-sectional TEM image of (a) as-deposited Cu/Ru thin film stack on Si(100) showing Ru columnar microstructure, and (b) the Cu/Ru/Si sample, vacuum annealed at 550 ºC, showing film delamination as well as diffusion into the Si substrate.

corroborates well the aforementioned SIMS profiling data to reveal the break down of Ru barrier at the higher temperature. In addition, the optical images in Figure 5.3a and 5.3b also reveal rectangular pitting formation that indicates the degradation of interfacial stability in the Cu/Ru/Si sample at 550 ^{o}C.

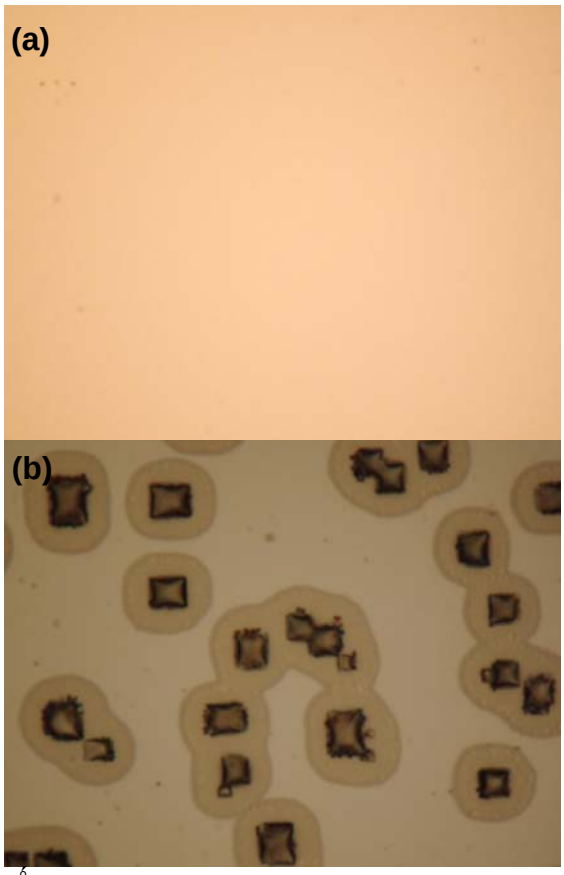

Figure 5.3: PVD Cu (~ 680 Å)/Ru (20 nm)/Si annealed under vaccum for 10 min. at (a) 450 ^{o}C showing similar features as before annealing and at (b) 550 ^{o}C showing Cu color fading and extensive surface change.

5.3.3 Electroplating of Cu

Further testing was carried out to the test the suitability of 20 nm Ru films as seed layers for electrochemical deposition of Cu. Figure 5.4 shows a typical cyclic voltammogram of a Cu plating-stripping cycle. The initial scanning potential was set at the open circuit potential (OCP) of metallic Ru (ca. +0.45 V vs. Ag/AgCl). The Cu plating current starts around -0.1 V and reaches a maximum near -0.3 V, where a more negative applied overpotential drives the Cu plating current into a diffusion-limited condition.[14] On the reverse scan, a cross over nucleation loop was observed between -0.2 and 0 V and followed by a well-defined anodic stripping peak.

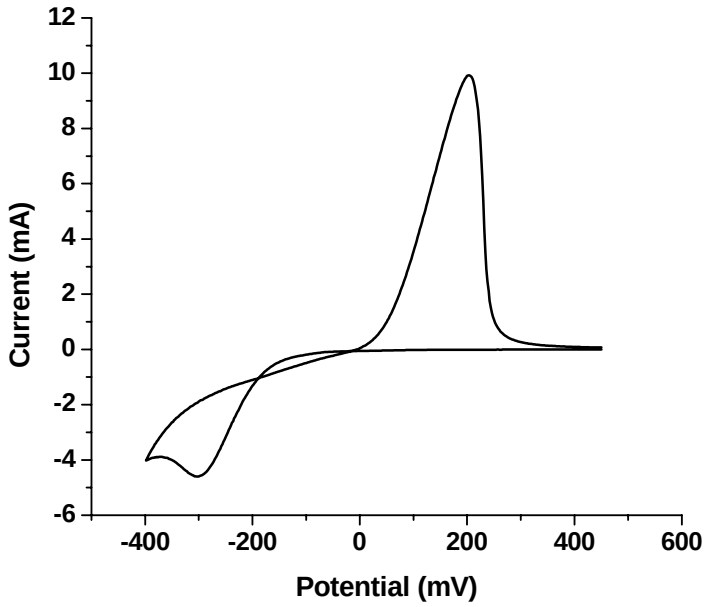

Figure 5.4: A cyclic voltammogram of Cu deposition and anodic stripping on sputter deposited Ru thin films, supported by Si wafer in a 50 mM $CuSO_4$/0.5 M H_2SO_4 solution. Scanning rate = 50 mV/sec.

Both visual inspection and OCP measurement (ca. +0.02 V) indicate that Cu plates well on the 20 nm Ru thin film. The Cu plating efficiency on Ru film is over 95% based on the anodic vs. cathodic charge integration ratio obtained from Figure 5.4. By progressively decreased the sputtering deposition time, a series of Ru ultra-thin films less than 20 nm were prepared. The Cu plating-stripping voltammograms from the thinner Ru films (< 20 nm) showed behavior that is very similar to Figure 5.4. However, the observed plating efficiency decreases slightly (< 6%) as the Ru barrier layer becomes thinner. Cu thin film deposition on Ru can be achieved by either linear sweep voltammetry or controlled potential chronoamperometry. The thickness of electroplated Cu overlayer on the Ru thin film can be precisely controlled. As the deposited Cu thickness increases, the observed OCP values decreases, similar to the previously reported trend based on a Ru metal disk electrode.[7] A freshly prepared 15 monolayer thick film of Cu on Ru

thin film already exhibits the same OCP as the bulk Cu metal. Thicker Cu layers can be plated on 20 nm Ru thin film by holding the potential at -0.3 V vs. Ag/AgCl for a pre-determined deposition time. These electroplated Cu films on Ru are shiny, smooth, and without any agglomeration as observed under SEM with 50K magnification.

5.3.4 Adhesion between Cu and Ru

Strong adhesion between Cu and the Ru barrier film is critical for the fabricated Cu interconnect microstructures to withstand the demanding chemical-mechanical planarization (CMP) process currently used in IC fabrication.[15] Both PVD and electroplated Cu thin films adhere very well to a 20 nm Ru thin film deposited onto Si substrate. Figures 5.5a and 5.5 b show the optical images of an electroplated-Cu/Ru/Si sample surface before and after a scribe-peel test.

The sample shown in Figure 5.5 consists of an ~100 nm thick film of Cu electroplated onto a Ru thin film. A sharp diamond scriber was used to gouge deep into the Si substrate, followed by a standard peeling test using a 3M Scotch packing tape. As shown in Figure 5.5a and 5.5b, the Cu/Ru film interface remains intact along the edges of deep gouges, clearly demonstrating the excellent adhesion between the plated Cu and Ru. The scribe-peel test result is consistent with the well-known high affinity of Cu adatoms to the Ru metal surface. It has been shown that Cu forms a bi-dimensional monolayer that follows the hexagonal symmetry of metallic Ru substrate surface before three-dimensional bulk deposition process begins.[16] Both thermal desorption spectroscopy and linear sweep voltammetry analysis reveal that the first Cu monolayer deposition is more stable ($\Delta G = 27$ kJ mol^{-1}) than subsequent multilayers of Cu on Ru.[17,18]

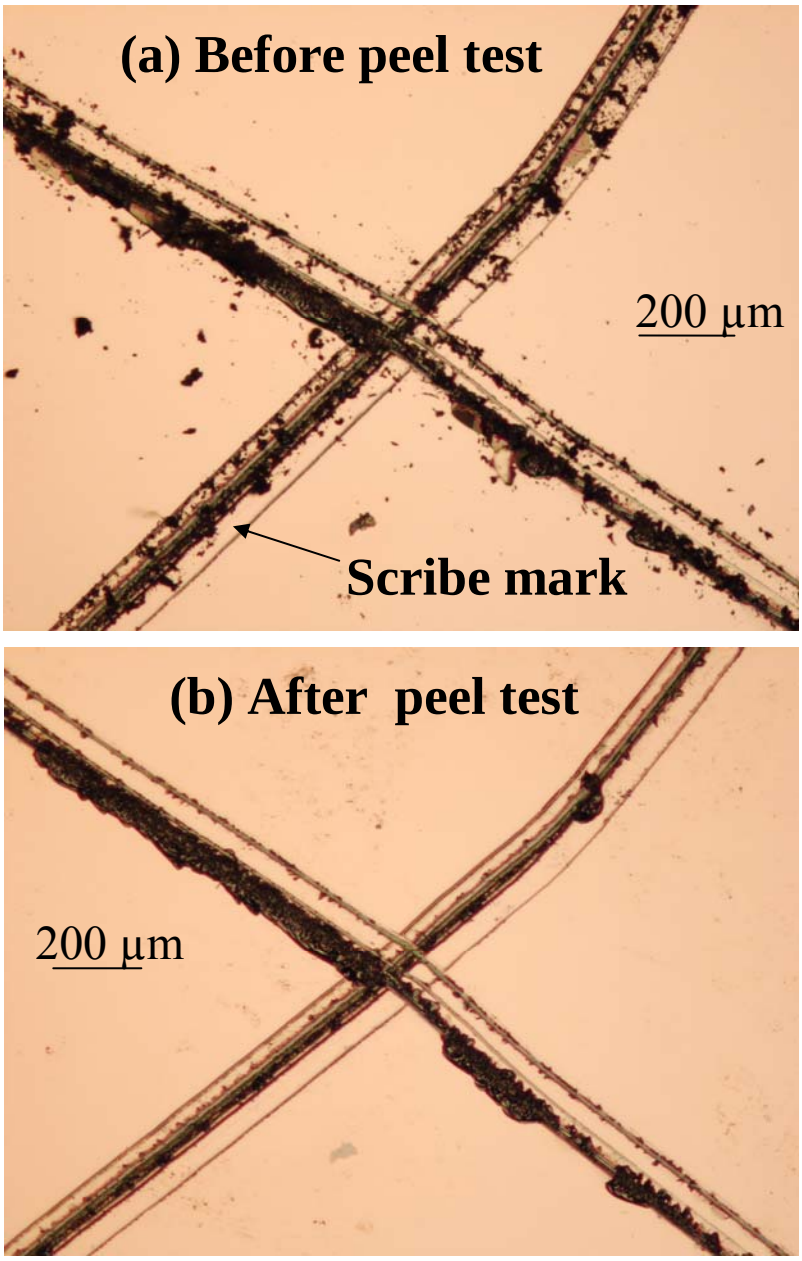

Figure 5.5: The optical images for an electroplated Cu film (ca. 100 nm) deposited on a 20 nm Ru/Si sample after scribed (left) and followed up with a peel test using 3M packing tape (left).

5.4 Conclusions

In summary, back-side SIMS depth profiling and TEM data confirm the interfacial stability of Cu/Ru(20 nm)/Si film stacks after annealing at 450 ^{o}C. In addition, Cu plates well

directly on a 20 nm Ru thin film sputter deposited on a Si substrate. The plating efficiencies observed for Cu plating on the Ru thin films (< 20 nm thick) is close to the Ru disk electrode. The electroplated Cu film on Ru is smooth without any agglomeration. The excellent adhesion, before and after vacuum annealing, between the electroplated Cu and Ru, is consistent with the well-known high affinity of Cu adatoms to the Ru metal surface. The new data demonstrate that Ru is a good candidate as a directly plate-able Cu diffusion barrier for the advanced integrated circuits application. Future work will need to address how thin Ru films can be and still allow practical ECD of Cu. It is desirable that the Ru films be as thin as 5 nm to be practical for semiconductor manufacturing applications at the 45 nm and 32 nm nodes. It will be critical for the interfacial properties of Cu on Ru as well as Ru on underlying dielectrics be well characterized and understood. This work should give confidence that such studies are worth undertaking.

5.5 References

(1) Kaloyeros, A.E.; Chen, X.; Stark, T.; Kumar, K.; Seo, S.C.; Peterson, G.G.; Frisch, H.L.; Arkles, B.; Sullivan, J. *J. Electrochem. Soc.*, **1999** *146* 170.

(2) Peters, L. *Semiconductor International*, **2003** *26* 50.

(3) International Technology Roadmap for Semiconductor -2002 Update, Semiconductor Industry Association (2002), pp. 74-75; see http://public.itrs.net/ (May 15, 2005).

(4) Radisic, J.G. Long, P.M. Hoffmann and P.C. Searson, *J. Electrochem. Soc.*, **2001** *148* C41.

(5) A. Radisic, Y. Cao, P. Taephaisitphongse, A.C. West and P.C. Searson, *J. Electrochem. Soc.*, **2003** *150* C362.

(6) Massalski, T.B. Editor, *Binary Phase Alloy Digrams*, *2nd ed*.; Materials Information Society: New York 1990; p. 1467.

(7) Chyan, O.; Arunagiri, T.N.; Ponuswamy, T. *J. Electrochem. Soc.*, **2003** *150* C347.

(8) Evans Analytical Group; see http://www.eaglabs.com/ (May 8, 2005).

(9) Yeo, K.L.; Wee, A.T.S.; See, A.; Liu, R.; Ng, C.M. *Appl. Surf. Sci.*, **2003** *335* 203.

(10) Xin, G.; Dong, G.; Xu, C.; Liangzhen, C.; Brox, O.; Benninghoven, A. *Appl. Surf. Sci.*, **2003** *441* 203.

(11) Quevedo-Lopez, M.A.; El-Bouanani, M.; Gnade, B.E.; Wallace, R.M.; Visokay, M.R.; Douglas, M.; Bevan, M.J.; Colombo, L. *J. Appl. Phys.*, **2002** *92* 3540.

(12) Quevedo-Lopez, M.A.; El-Bouanani, M.; Kim, M.J.; Gnade, B.E.; Wallace, R.M.; Visokay, M.R. *Appl. Phys. Lett.*, **2002** *81* 1609.

(13) Quevedo-Lopez, M.A.; El-Bouanani, M.; Kim, M.J. Gnade, B.E.; Wallace, R.M.; Visokay, M.R.; LiFatou, A.; Bevan, M.J.; Colombo, L. *Appl. Phys. Lett.*, **2002** *81* 1074.

(14) Bard, A.J.; Faulkner, L.R. *Electrochemical Methods: Fundamentals and Applications*, Chapter 6, 2nd ed.; John Wiley & Sons: New York 2001.

(15) Steigerwald, J.N.; Murarka, S.P.; Gutmann, R.J. *Chemical Mechanical Planarization of Microelectronic Materials*; Wiley Interscience: New York 1997.

(16) Christmann, K.; Ertl, G.; Shimizu, H. *J. Catal.* **1980** *61(2)* 397.

(17) Zavadil, K.R.; Ingersoll, D.; Rogers, J.W. Jr., *J. Electroanal. Chem.*, **1991** *318* 223.

(18) Stuve, E.M.; Rogers, J.W. Jr.; Ingersoll, D.; Goodman, D.W.; Thomas, M.L. *Chem. Phys. Letters*, **1988** *149* 557.

CHAPTER 6

ACHIEVEMENTS OF THIS WORK

In this chapter, the conclusions that have been drawn from Chapters 2 through 5 will be summarized and discussed from a broader perspective. Implications of these conclusions for future research work and applications will be addressed.

6.1 Conclusions from Chapter 2

It was demonstrated that the standard metals clean chemistry used by the semiconductor industry, SC2, a mixture of HCl, H_2O_2, and H_2O, could be significantly optimized, both for performance and for cost. As typically used, H_2O_2 decomposed rapidly in the highly acidic mixture, its concentration diminishing to nearly zero in as little as thirty minutes at 80 °C. Contrary to what has been reported in the basic SC1 mixture (NH_4OH, H_2O_2 and H_2O) Fe^{3+} contamination has a negligible impact on H_2O_2 decomposition in SC2 solutions at the levels that can reasonably be expected to be encountered in semiconductor grade chemicals. This is suggested to be due to the fact that an abundance of free H^+ interferes with one or more of the key steps in the metal catalyzed decomposition of H_2O_2. HCl concentration has an impact on the decomposition rate though and the lifetime of the H_2O_2 in an SC2 bath can be greatly extended by reduction of the HCl concentration.

As it turns out, the lifetime of the H_2O_2 is not of critical importance, as dilute HCl will remove metals from oxidized surfaces as effectively as an SC2 mixture containing H_2O_2. With the cost of ultrapure chemicals continuously increasing it is important to maximize the efficiency of their use. Removing H_2O_2 from the SC2 clean as well as increasing the dilution of the HCl both result in significant cost savings to the fab. Reducing the HCl concentration below the critical threshold of 0.01 M, and thereby pushing the pH above the point of zero charge for SiO_2

(making the wafer surface negatively charged) metals can be removed from wafers without depositing particles from solution.

While this work was performed in a bath type cleaning system, the results are equally applicable to other equipment technologies that use liquids to clean wafers, e.g. spray tools. While H_2O_2 decomposition is not an issue in a spray tool as the chemicals are mixed during use and are not in contact with the wafers for very long, significant cost savings can be realized by reducing the amount of HCl used and by eliminating the H_2O_2 from this processing step.

Based on optimizing metal removal and particle addition, an optimum processing temperature and concentration of 50 °C and 0.001 M was proposed. This allowed for one order of magnitude variation in concentration and 10 °C to 20 °C variation in temperature without serious degradation in the metal and particle performance. The proposed chemistry was then proven to be viable in a manufacturing environment. It resulted in slightly superior gate oxide integrity (GOI) as measured by E_{bd} while Q_{bd} was unchanged versus the baseline sequence, resulting in the process being implemented in multiple technology nodes at Texas Instruments.

Future studies in this area could be profitably focused on studying metals other than the ones that were tested on in this work (Fe, Zn, Ca, Cu) as there may very well be metals coming into use in the SC industry (Ba, W, Ta, Ti, Zr, etc) that may behave very differently both from the standpoint of metal removal as well as from the standpoint of H_2O_2 decomposition. The decomposition reaction pathways of all metals may not be inactivated in acidic environments. Further study into the kinetics and mechanism of H_2O_2 deomposition in SC2 solution is worth pursuing as additional insight into how to further optimize this cleaning solution could be gleaned from such a study. This is also an area of ongoing scientific endeavor as the exact mechanism of H_2O_2 decomposition in these type of solutions is still undetermined. Finally, the

potential for a dilute SC2 or dilute HCl mixture to be used not only as a particle neutral solution but also as a particle removal solution bears further exploration. If this could be achieved, then the need for SC1 mixtures and their attendant etching of wafers could possibly be eliminated.

6.2 Conclusions from Chapter 3

In this chapter, the proposal was put forth that the surface of an oxidized silicon wafer chemically behaves in the same manner as the surface of silica gel particles. It was further proposed that metal adsorption on oxidized silicon wafers could be therefore be understood in terms of the complexation of metals by the silanol functional groups on the wafer surface, as this has been demonstrated to be the case with silica gels. Arguing by analogy, multiple experiments were undertaken to demonstrate that the proposal was both reasonable and plausible.

It was shown with data and by literature survey that areal metal concentrations on the surface of oxidized silicon wafers never exceeds the theoretical maximum of 4.6-5.5 x 10^{14} at/cm^2 that would be predicted from the known surface silanol concentration on silica gel particles. In fact, it is difficult to find examples of oxidized wafer surface concentrations exceeding 10% of this theoretical maximum. It was also shown with Fe and Ca that the adsorption rate of metals on oxidized silicon wafers as pH increases is similar to what is reported in the literature with silica gel. Metal concentration and pH were seen to be the primary factors controlling metal adsorption on oxidized silicon wafers as would be expected if the proposed mechanism were correct.

Finally, a proportional relationship between metal hydrolysis constants and metal-silanol complexation constants was identified in the literature. This was used to show that for both acidic and basic solutions, metal adsorption on oxidized silicon wafer surfaces qualitatively trended as would be expected based on their hydrolysis constants. This was demonstrated both

for experimental data as well as for published data from other authors that was found in the literature.

The major limitation of this work was that it was all carried out under conditions that can best be described as "real world", meaning conditions that are encountered in a manufacturing environment. Because of this, it was not possible to correlate results quantitatively with what has been published for metal reactivity with silica gel. It is also believed that this limitation is primarily responsible for the non-conforming behavior of Pb, Bi, and Fe in HNO_3 solutions. The major sources of non-linearity in this work reside in the uncontrolled ionic strength of these solutions, the use of counterions (NO_3^-, Cl^-, NH_3, NH_4^+, O_2H^-) that have low but measurable interactions with the metals in solution, and in the abundance of metal ions relative to the available silanol reactive sites. All but the last of these constraints could be eliminated in future work.

This is an area that is deserving of additional future work. Ideally, additional study would be devoted to making the proposed model quantitative so that metal contamination from a solution could be accurately calculated provided the key variables were known (pH, metal concentration, counterions, ionic strength, etc.). Demonstrating conclusively that the proposed model for metal interactions with oxidized silicon surfaces is correct is important as it means that a wealth of prior knowledge generated in the field of silica gel research could now be profitably applied to solving the challenges that are encountered by the SC industry.

6.3 Conclusions from Chapter 4

The effects of trace metals on p-type and n-type silicon following thermal cycles were investigated using microwave photoconductance decay (μPCD) and surface photovoltage (SPV). It was observed that the amounts of metal incorporated into the substrate from surface

contamination is highly dependent not only on the metal, but also on the annealing ambient, with wet ambients and N_2 ambients driving in almost 100% of the metal while dry O_2 only drives in ~50% of a given metal. This behavior seen by bulk Fe concentration measurements with SPV was confirmed with TXRF surface analyses. It was also seen with TXRF analyses of Cu contaminated wafers as well.

The annealing ambient determines the sample surface passivation, which is a critical parameter for measuring lowly contaminated wafers with μPCD. Without annealing in an oxidizing ambient, it was demonstrated that treatment in HF solutions can be used to reduce the surface recombination velocity of the substrates. The μPCD and SPV techniques can be considered equivalent as shown for the determination of the effective capture cross-section of the Fe traps and the measurement of the effective MCLT.

Substrate doping type has a strong impact on the recombination activity of metallic impurities. Fe, as expected, degrades the minority carrier properties in p-type substrates but its impact on n-type substrates is at least one order of magnitude lower than on p-type. In contrast, Cu, Ru, and Co are highly detrimental to n-type material, but have no significant impact on the minority carrier properties of p-type silicon. Pt and Ir appear to degrade both doping types equally.

The experience gained working with Fe and Cu in detail was applied to a broad spectrum of metals. It was found that the behavior of these metals could largely be understood based on their diffusivity, solubility, and vapor pressure at the temperatures encountered during high temp anneal. It was further seen that deviations from this expected behavior could be explained in terms of reactions that could be expected to occur during processing. The major exceptions to this were the apparent evaporation of Ba from p-type wafers and the apparent evaporation of Ta

and Zr during wet oxidation. The behavior of each metal tested in the survey is shown in Table 6.1 (cf. Table 4.10).

Behavior during thermal process				
Metal	**Surface?**	**Evaporate?**	**Diffuse?**	**Comments**
Ba	√	√		Remains almost completely at the surface. Small amount of cross contamination detected. Majority of metal gone from p type wafers. Presumed evaporated.
Bi		√		None detected at surface and no impact to L. Evidence of significant evaporation. Presumed to have completely evaporated.
Co	√	√	√	Predominantly diffused in, causing degradation in L (n type > p type). Evidence of varying amounts of evaporative cross contamination. 10-15% at surface after oxidation. 20-30% at surface after N2 anneal.
Ir	√		√	10% remains at surface after oxidation. 50% at surface after N2 anneal. No evidence of evaporation. Diffuses in and degrades L.
Mo	√	√	√	2-40% remains on surface, with wet oxidation leaving least on surface. Evidence of significant amount of evaporation. No impact to L but some diffusion into Si expected.
Ni	√	√	√	40-60% remains on surface. Evidence of low level of evaporation. Remainder assumed to have diffused into the bulk. No impact on L.
Pb		√		None detected at surface and no impact to L. Evidence of evaporation. Presumed to have completely evaporated.
Pt	√		√	Very little remains on surface after oxidation but 10-20% remains following N2 anneal. No evidence of evaporation. Diffusion into silicon confirmed by degradation of L.
Ru	?	?	√	None detected after anneal but detection limit was very poor. No evidence of evaporation but same detection limit problem. Diffusion into silicon confirmed by degradation of L.
Sr	√			100% remained on the surface. No evidence of evaporation or diffusion into the bulk.
Ta	√	√		Almost quantitatively remained at the surface. Significant evaporation detected during wet oxidation only. No impact to L and no diffusion expected.
W	√	√		Almost quantitatively remained at the surface. Significant evaporation detected during wet oxidation only. No impact to L and no diffusion expected.
Zr	√	√		Almost quantitatively remained at the surface with low level of evaporation detected during wet oxidation. No impact to L and no diffusion expected.

Table 6.1: Summary of metal behavior during thermal processing observed in survey study.

6.4 Conclusions from Chapter 5

Back-side SIMS depth profiling and TEM data confirmed the interfacial stability of Cu/Ru(20 nm)/Si film stacks after annealing at 450 ^{o}C. Cu plates well directly onto a 20 nm Ru thin film sputter deposited on a Si substrate. The plating efficiencies observed for Cu plating on the Ru thin films (< 20nm thick) is close to what is seen with bulk Ru. Excellent adhesion, before and after vacuum annealing, was observed between the electroplated Cu and Ru, which is consistent with the well-known high affinity of Cu adatoms to the Ru metal surface. The new

data demonstrate that Ru is a good candidate as a directly plateable Cu diffusion barrier for application to advanced integrated circuit interconnects. Future work will need to address how thin Ru films can be and still allow practical ECD of Cu. It is desirable that the Ru films be as thin as 5 nm to be practical for semiconductor manufacturing applications at the 45nm and 32 nm nodes. It will be critical for the interfacial properties of Cu on Ru as well as Ru on underlying dielectrics, especially on porous low k dielectric films be well characterized and understood.

REFERENCE LIST

(1) Ahrland, S.; Grenthe, I.; Norén, B. *Acta Chem. Scand.* **1960** *14* 1059.

(2) Aiginger, H. *Spectrochemica Acta* **1991** *46B* 1313.

(3) Alcock, C.B.; Itkin, V.P.; Horrigan, M.K, *Canadian Metallurgical Quarterly*, **1984** *23* 309.

(4) Anttila, O.J.; Tilli, M.V.; Schaekers, M.; Claeys, C.L. *J. Electrochem. Soc.* **1992** *139* 1180.

(5) Aoki, M.; Itakura, T.; Sasaki, N. *Japn. J. Appl. Phys.* **1995** *34* 712.

(6) Arunagiri, T.N.; Zhang, Y.; Chyan, O.; El-Bounani, M.; Kim, M.J.; Chen, K.H.; Wu, C.T.; Chen, L.C. *Appl. Phys. Lett.* **2005** In Press.

(7) Baes, C.F.; Mesmer, R.E. *The Hydrolysis of Cations;* John Wiley and Sons: New York, 1976.

(8) Bai, P.; Yang, G.-R.; Lu, T.-M. *J. Appl. Phys.* **1990** *68 (7)* 3313.

(9) Barb, W.G.; Baxendale, J.H.; George,P.; Hargrave, K.R. *Trans. Faraday Soc.* **1951** *47* 591.

(10) Bard, A.J.; Faulkner, L.R. *Electrochemical Methods: Fundamentals and Applications*, Chapter 6, 2nd ed.; John Wiley & Sons: New York 2001.

(11) Bearda, T.; de Gendt, S.; Loewenstein, L. ; Knotter, M. ; Mertens, P. ; Heyns, M. *Fourth International Symposium on Ultra Clean Processing of Silicon Surfaces;* Scitec Pulbications, Ltd.: Zuerich-Uetikon, Switzerland 1999; p 11.

(12) Benninghoven, A. *Angew. Chem. Int. Engl.* **1994** *33* 1023.

(13) Bergholz, G.; Zoth, F.; Gelsdorf, F.; Kolbesen, B *Defects in Silicon II 91-9*; eds. Bullis, W.M.; Gosele, U.; Shimura, F; The Electrochemical Society: Pennington, NJ, 1991; p 21

(14) Boubekur, H.; Höpfner, J.; Mikolajick, T.; Dehm, C.; Ryssel, H. *J. Electrochem. Soc.* **2000** *147* 4297.

(15) Burgess, J. *Ions in Solution: Basic Principles of Chemical Interactions*; Ellis Horwood Limited: Chichester, U.K. 1988.

(16) Busta, H.H.; Waggener, H.A. *J. Electrochem. Soc.* **1977** *124* 1424.

(17) Busta, H.H.; Waggener, H.A.; *J. Electrochem. Soc.* **1977** *124* 1424.

(18) Christmann, K.; Ertl, G.; Shimizu, H. *J. Catal.* **1980** *61(2)* 397.

(19) Chyan, O.; Arunagiri, T.N.; Ponuswamy, T. *J. Electrochem. Soc.*, **2003** *150* C347.

(20) Chyan, O; Arunagiri, T.; Hurd, T. *Electrochem and Sol. State Lett.* **2004**, 7(8), G154.

(21) Dhanda, S.; Chiarello, R.P.; Helms, C.R.; Gupta, P. *Electrochemical Society Proceedings 97-35;* The Electrochemical Society: Pennington, NJ, 1997; 113.

(22) Douglas, M. *T.I. Technical Journal* **1995** *12(5)* 19.

(23) Douglas, M; Chen, P.J. *Surf. Interface Anal.* **1998** *26* 984.

(24) Dugger, D.L.; Stanton, J.H.; Irby, B.N.; McConnell, B.L.; Cummings, W.W.; Maatman, R.W. *J. Phys. Chem.* **1964** *68* 757.

(25) Emsley, J. *Nature's Building Blocks;* Oxford University Press: New York, 2001.

(26) Evans Analytical Group; see http://www.eaglabs.com/ (May 15, 2005)

(27) Falster, R. *Appl. Phys. Lett.* **1985** *46* 737.

(28) Gale, G.W.; Rath, D.L.; Cooper, E.I.; Estes, S.; Okorn-Schmidt, H.F.; Brigante, J.; Jagannathan, R.; Settembre, G. *J. Electrochem. Soc.* **2001** *148* G513.

(29) Gilbert, S.R.; Ritchey, D.; Tavassoli, M.; Amano, J.; Colombo, L.; Summerfelt, S.R. *J. Electrochem. Soc.* **2001** *148* 195.

(30) Goetzberger, A.; Shockley, W. *J. Appl. Phys.* **1960** *31* 1821.

(31) Goetzberger, A.; Shockley, W. *J. Appl. Phys.* **1960** *31* 1821.

(32) Graff, K. *Metal Impurities in Silicon-Device Fabrication*; Springer-Verlag: Berlin, 1995.

(33) Graff, K. *Metallic Impurities in Silicon Device Fabrication 2nd Ed*.; Springer-Verlag: Berlin 2000; p 145

(34) Graff, K.; Heim, P.; Pieper, H. *J. Electrochem. Soc.* **1994** *141* 2821.

(35) Graff, K.; Pieper, H. *J. Electrochem. Soc.* **1981** *128* 669.

(36) Grove, A. *Physics and Technology of Semiconductor Devices* John Wiley and Sons: New York, NY, 1967.

(37) Hall, L.; Sees, J.; Hurd, T.; Schmidt, B.; Bellay, L.; Loewenstein, L.; Mertens, P.W. *Proceedings of the Fourth International Symposium on Ultra Clean Processing of Silicon Surfaces;* Scitec Publications: Switzerland 1999; p 53.

(38) Hangleiter, A. *Physical Review B*, **1987** *35 (17)* 9149.

(39) Hayami, Y.; Okui, Y.; Ogawa, H.; Fujimura, S. *ECS Proceedings* 97-3; The Electrochemical Society: Pennington, NJ 1997; p 97.

(40) Hayashida, I.; Kakizawa, M.; Umekita, K.; Nawa, H.; Maraoka, H.; U.S. Patent 5290361, 1994.

(41) Helms, C.R.; Park, H. *ECS Proceedings **1994** 94-7* 26.

(42) Henley, W.; Jastrzebski, L; Haddad, N. *Proceedings of the 1993 IEEE International Reliability Physics Symposium*, 1993; p 22.

(43) Henley, W.B.; Jastrzebski, L.; Haddad, N.F. *Mat. Res. Soc. Symp. Proc.* **1993** *315* 299.

(44) Hiraiwa, A.; Itoga, T. *IEEE Trans. on Semicond. Manufact.* **1994** *7 (1)* 60.

(45) Honda, K.; Nakanishi, T.; Ohsawa, A.; Toyokura, N *J. Appl. Phys.* **1987** *62* 1960

(46) Hourai, M.; Murakami, K.; Shigematsu, T.; Fujino, N.; Shiraiwa, T. *Jpn. J. Appl. Phys.***1989** *28* 2413.

(47) Hourai, M.; Naridomi, T.; Oka, Y.; Murakami, K.; Sumita, S.; Fujino, N.; Shiraiwa, T. *Jpn. J. Appl. Phys.* **1988** *27* L2361.

(48) Hurd, T.Q. et al, *ECS Proceedings 95-20* 1995; p 277.

(49) Hurd, T.Q.; Rotondaro, A.L.P.; Sees, J.; Misra, A.; Appel, C.;*ECS Proceedings 97-35;* The Electrochemical Society: Pennington, NJ 1997; p 105.

(50) Iler, R.K. *The Chemistry of Silica*, John Wiley and Sons: New York 1979; p 633.

(51) Inczédy, J. *Analytical Applications of Complex Equilibria*; Ellis Horwood Limited: Chichester, U.K. **1976**; p 26.

(52) International Technology Roadmap for Semiconductor -2002 Update, Semiconductor Industry Association (2002), pp. 74-75; see http://public.itrs.net/ (May 8, 2005).

(53) *International Technology Roadmap for Semiconductors 2003 Edition*, **2003** http://public.itrs.net/Files/2003ITRS/Home2003.htm, International Sematech (May 1, 2005)

(54) James, R.O.; Healy, T.W. *J.Colloid Sci.* **1972** *40* 42.

(55) James, R.O.; Healy, T.W. *J.Colloid Sci.* **1972** *40* 53.

(56) James, R.O.; Healy, T.W. *J.Colloid Sci.* **1972** *40* 65.

(57) Jastrzebski, L.; Henley, W.; Nuese, C.J. *Solid State Technol*, **1992** *35* 27.

(58) Jastrzebski, L.; Lagowski, J.; Kontkiewicz, M.; Edelman, P. *J. Electrochem. Soc.* **1993** *140* 1152.

(59) Jones, R.E. *Integrated Ferroelectrics*, **1995** *6* 81.

(60) Kaloyeros, A.E.; Chen, X.; Stark, T.; Kumar, K.; Seo, S.C.; Peterson, G.G.; Frisch, H.L.; Arkles, B.; Sullivan, J. *J. Electrochem. Soc.,* **1999** *146* 170.

(61) Kaniava, A.; Menczigar, U.; Vanhellemont, J. ; Poortmans, J.; Rotondaro, A.L.P.; Gaubas, E.; Vaitkus, J.; Köster, L.; Gräf, D. *Mat. Res. Soc. Symp. Proc.* **1995** *386* 389.

(62) Katz, L.E. *J. Electrochem. Soc.* **1974** *121* 969.

(63) Kern, W.; Puotinen, D.A. *RCA Review* **1970** *31* 187.

(64) Kern, W. and Poutinen, D.A. *RCA Review* **1970** *31* 207.

(65) Kern, W. and Poutinen, D.A. *RCA Review* **1970** *31* 234.

(66) Kitagawara, Y.; Yoshida, T.; Hamaguchi, T.; Takenaka, T. *J. Electrochem. Soc.* **1995** *142 (10)* 3505.

(67) Knoth, J.; Schwenke, H.; Weisbrod, U. *Spectrochemica Acta* **1989** *44B* 477.

(68) Kola, R.R.; Rozgonyi, G.A.; Li, J.; Rogers, B; Yan, T. Y.; Bean, K.E.; Lindberg, K. *Appl. Phys. Lett.*, **1989** *55* 2108.

(69) Kragten, J. *Atlas of Metal-Ligand Equilibria in Aqueous Solution*; John Wiley and Sons: New York, 1978.

(70) Kregsamer, P. *Spectrochemica Acta* **1991** *46B* 1333.

(71) Kremer, M. *Int. J. Chem. Kin.* **1985** *17* 1299.

(72) Kremer, M. *Trans. Faraday Soc.* **1962** *58* 702; **1963** *59* 2535.

(73) Lagowski, J.; Edelman, P.; Kontkiewicz, A.M.; Milic, O.; Henley, W.; Dexter, M.; Jastrzebski, L.; Hoff, A.M. *Appl. Phys. Lett.* **1993** *63 (22)* 3043.

(74) Lagowski, J.; Kontkiewicz, A.M.; Jastrzebski, L.; Edelman, P. *Appl. Phys. Lett.*, **1993** *63 (21)* 2902.

(75) Lagowski, J.; Kontkiewicz, M.; Jastrzebski, L.; Edelman, P. *Semicond. Sci. Technol.* **1992** *7* 185.

(76) Laitinen, H.A. *Chemical Analysis;* McGraw Hill: NY, 1960; p 411.

(77) Lang, D.V. *J. Appl. Phys.* **1974** 45 3023

(78) Langmuir, I. *Physic Z.* **1913** *14* 1273

(79) Lee, J-K; Liu, B.Y.H.; Rubow, K.L. *IES 39th Annual Technical Meeting 1993 Proceedings Vol.1;* IES: Mount Prospect, Illinois, 1993; p 209.

(80) Lemke, H. *Phys. Status Solidi* **1990** *122* 617.

(81) Lemke, H. *Semiconductor Silicon 1994*; Electrochem. Society: Pennington, NJ 1994; p 695.

(82) Lewis, R.A. Sr. *Hawley's Condensed Chemical Dictionary 14th E.*; Wiley Interscience: New York 2001; p 759.

(83) Lide, D.R. Ed. *CRC Handbook of Chemistry and Physics, 77th Ed.* CRC Press: New York 1996**.**

(84) Lisiak, K.P.; Milnes, A.G. *Solid State Electron.* **1976** *19* 115.

(85) Liu, B.Y.H. *J. Electrochem. Soc* **1993** *140* 1403.

(86) Loewenstein, L.; Mertens, P.W. *J. Electrochem. Soc.* **1998** *145* 2841.

(87) Loewenstein, L.M.; Charpin, F.; Mertens, P.W.; *J. Electrochem. Soc.* **1999** *146* 719.

(88) Martin, A.R.; Baeyens, M.; Hub, W.; Mertens, P.W.; Kolbesen, B.O. *Microelectronic Engineering* **1999** *45* 197.

(89) Massalski, T.B. Editor, *Binary Phase Alloy Digrams, 2nd ed.*; Materials Information Society: New York 1990; p. 1467.

(90) Mertens, P.W.; Bearda, T.; Loewenstein, L.M.; Martin, A.R.; Hub, W.; Kolbesen, B.O. Teerlinck, I.; Vos, R.; Baeyens, M.; de Gendt, S.; Kenis, K.; Heyns, M.M. *Defects in Silicon III PV 99-1;* Electrochemical Society: Pennington, NJ 1999; p 401.

(91) Mertens, P.W.; Meuris, M.; Verhaverbeke, S. ; Heyns, M.M.; Schnegg, A.; Gräf, D.; Philipossian, A. *Proc. of the 38th Annual Tech. Meeting of the Institute of Environmental Sciences;* IES: Mount Prospect, IL 1992; p 475.

(92) Mertens, P.W.; Rotondaro, A.L.P.; Meuris, M.; Schmidt, H.F.; Heyns, M.M.; Gräf, D. *Proc. of the 40th Annual Techn. Meeting of the Institute of Environmental Sciences;* IES: Mount Prospect, IL 1994; p 325.

(93) Meuris, M.; Heyns, M.; Kuper, W.; Verhaverbeke, S.; Philipossian, A. *ECS Proceedings 91-11: ULSI Science and Technology 1991;* ECS: Pennington NJ, 1991.

(94) Meuris, M.; Heyns, M.; Kuper, W.; Verhaverbeke, S.; Philipossian, A.; *ULSI Science and Technology 1991*, ed. Andrews, J.M.; Celler, G.K.; Vol 91-11, The Electrochemical Society: Pennington, NJ, 1991.

(95) Meuris, M.; Heyns, M.; Verhaverbeke, S.; Mertens, P.; Philipossian, A.; *1991 Microcontamination Conference Proceedings* Canon Communities Inc.: Santa Monica, CA 1991; p 658.

(96) Miyazaki, M.; Sano, M.; Sumita, S.; Fujino, N. *Jpn. J. Appl. Phys.***1991** *30* L295.

(97) Miyazaki, M.; Miyazaki, S.; Kitamura, T.; Aoki, T.; Nakashima, Y.; Hourai, M.; Shigematsu, T. *Jpn. J. Appl. Phys.***1995** *34* 409.

(98) Mori, Y.; Uemura, K. ; Shimanoe, K. J. *Electrochem Soc* **1995** *14* 3104.

(99) Mouche, L.; Tardif, F.; Derrien, J.; *J. Electrochem. Soc.* **1995** *142* 2395.

(100) Naito, S.; Nakashizu, T. *Mat. Res. Soc. Symp. Proc.* **1992** *262* 641.

(101) Neumann, C.; Eichinger, P. *Spectroch. Acta* **1991** *46B (10)* 1369.

(102) Nicolet, M.-A.; Lau, S.S. V*LSI Electronics;* Academic Press: New York 1983; p 330.

(103) Norga, G.J.; Kimerling, L. *J. Electron. Mater*. **1995** *24* 397.

(104) O'Brien, S. *TI Technical Report Number 08-94-28*, 1994**.**

(105) Ohmi, T.; Imaoka, T.; Sugiyama, I.; Kezuka, T. *J. Electrochem. Soc.* **1992** *139 (11*) 3317.

(106) Parks, G. *Chem. Rev*. **1965** *65* 177.

(107) Peters, L. *Semiconductor International*, **2003** *26* 50.

(108) Prange, A. *Spectrochemica Acta* **1989** *44B* 437.

(109) Quevedo-Lopez, M.A.; El-Bouanani, M.; Gnade, B.E.; Wallace, R.M.; Visokay, M.R.; Douglas, M.; Bevan, M.J.; Colombo, L. *J. Appl. Phys.*, **2002** *92* 3540.

(110) Quevedo-Lopez, M.A.; El-Bouanani, M.; Kim, M.J. Gnade, B.E.; Wallace, R.M.; Visokay, M.R.; LiFatou, A.; Bevan, M.J.; Colombo, L. *Appl. Phys. Lett.*, **2002** *81* 1074.

(111) Quevedo-Lopez, M.A.; El-Bouanani, M.; Kim, M.J.; Gnade, B.E.; Wallace, R.M.; Visokay, M.R. *Appl. Phys. Lett.*, **2002** *81* 1609.

(112) Quirk, M.; Serda, J. *Semiconductor Manufacturing Technology* Prentice-Hall Inc.: Upper Saddle River, NJ, 2001; p 537.

(113) Radisic, A., Cao, Y., Taephaisitphongse, P., West, A.C., and Searson, P.C., *J. Electrochem. Soc.*, **2003** *150* C362.

(114) Radisic, J.G. Long, P.M. Hoffmann and P.C. Searson, *J. Electrochem. Soc.*, **2001** *148* C41.

(115) Riley, D.J. and Carbonell, R.G. *J. of Coll. and Interface Sci*. **1991** *158* 274.

(116) Riley, D.J. and Carbonell, R.G. *J. of Coll. and Interface Sci.***1991** *158* 259.

(117) Rotondaro, A.L.P.; Hurd, T.Q.; Kaniava, A.; Vanhellemont, J.; Simoen, E.; Heyns, M.M.; Claeys, C. *J. Electrochem. Soc.* **1996** *143 (9)* 3014.

(118) Ryuta, J.; Yoshimi, T.; Kondo, H.; Okuda, H.; Shimanuki, Y. *Jpn. J. Appl. Phys.* **1992** *31 (8)* 2338.

(119) Schindler, P.; Kamber, H.R. *Helvetica Chimica Acta* **1968** *51* 1781.

(120) Schindler, P.; Wälti, E.; Fürst, B. *Chimia* **1976** *30* 107

(121) Schindler, P.W. *Metal Ions in Biological Systems* **1984** *18* 105.

(122) Schindler, P.W.; Fürst, B.; Dick, R.; Wolf, P.U. *J.Colloid Sci.* **1976** *55* 469.

(123) Schmidt, H.F.; Mertens, P.W.; Meuris, M.; Verhaverbeke, S.; Heyns, M.; Dillenbeck, K.; *Proceedings of UCPSS 1992*; IMEC Press: Leuven Belgium.

(124) Schmidt, H.F.; Mertens, P.W.; Meuris, M.; Verhaverbeke, S.; Heyns, M.M.; Kubota, M.; Dillenbeck, K. *IES 39th Annual Technical Meeting 1993 Proceedings Vol. I;* IES: Mount Prospect Illinois, 1993; p 238.

(125) Schmidt, H.F.; Meuris, M.; Mertens, P.W.; Rotondaro, A.L.P.; Heyns, M.M.; Hurd, T.Q.; Hatcher, Z. *Jpn. J. Appl. Phys.* **1995** *34* 727.

(126) Sillen, L.G. et al, *Stability Constants of Metal Ion Complexes*.; The Chemical Society: London ,1964; *Supplement No. 1* 1971.

(127) Skood, D.A.; West, D.M.; Holler, F.J. *Fundamentals of Analytical Chemistry, 7th Ed.;* Saunders College Publishing: Philadelphia, PA, 1996; p 611.

(128) Skoog, D. *Principles of Instrumental Analysis, 3rd Ed.;* Saunders College Publishing: Philadelphia PA, 1985; p 523.

(129) Smith, G.W.; Jacobson, H.W. *J. Phys. Chem.* **1964** *68* 757.

(130) Steigerwald, J.N.; Murarka, S.P.; Gutmann, R.J. *Chemical Mechanical Planarization of Microelectronic Materials*; Wiley Interscience: New York 1997.

(131) Stephens, A.W.; Aberle, A.G.; Green, M.A. *J. Appl. Phys.* **1994** *76 (1)* 363.

(132) Streetman, B. *Solid State Electronic Devices, 4th Ed.* Prentice Hall: Upper Saddle River, NJ, 1995 ; p 300.

(133) Streusand, B. *Encyclopedia of Materials Characterization* eds. Brundle, C.R.; Evans, C.; Wilson, S.; Butterworth Heinman: Boston MA, 1992; p 624.

(134) Stumm, W.; Kummert, R.; Sigg, L. *Croat. Chem. Acta* **1980** *53 (2)* 291.

(135) Stuve, E.M.; Rogers, J.W. Jr.; Ingersoll, D.; Goodman, D.W.; Thomas, M.L. *Chem. Phys. Letters*, **1988** *149* 557.

(136) Sugihara, Y.; Tanaka, K.; Kawakami, M.; U.S. Patent 5302311, 1994.

(137) Takiyama, M.; Ohtsuka, S.; Hayashi, S.; Tachimori, M. *Semiconductor Silicon/1994 94-10* eds. Huff, H; Bergholz, W.; Sumino, K. The Electrochemical Society: Pennington, NJ, 1994; p 346.

(138) Visokay, M.R.; Chambers, J.J.; Rotondaro, A.L.P.R.; Colombo, L. *Appl. Phys. Lett.* **2002** *80* 1.

(139) Vogel, E.; Misra, V. *Handbook of Silicon Semiconductor Metrology* ed. Diebold, A. Marcel Dekker Inc: New York, NY 2001; p 85.

(140) Walling, C. and Cleary, M. *Int. J. Chem. Kin.* **1977** *IX* 595.

(141) Ward, P.J. *J. Electrochem. Soc.***1982** *129* 2573.

(142) Weber, E.R. *J. Appl. Phys.* **1983** *A30* 1.

(143) Wieckhardt, C; Moritz, F.; Grotemeyer, J. *Mass Spectrometry Reviews* **1996** *15* 139.

(144) Williams, C.K.; Hamaker, R.W.; Ganeson, S.G.; Kuehn, R.T.; Swartzel, K.R.; O'Sullivan, J. *J. Electrochem. Soc.* **1995** *142* 303.

(145) Wolf, S. Silicon *Processing for the VLSI Era, Vol 3: The Submicron MOSFET* Lattice Press: Sunset Beach, California, 1995; p 438.

(146) Xin, G.; Dong, G.; Xu, C.; Liangzhen, C.; Brox, O.; Benninghoven, A. *Appl. Surf. Sci.*, **2003** *441* 203.

(147) Yamamichi, S.; Muramatsu, Y.; Lesaicherre, P.-Y.; Ono, H. *Japn. J. Appl. Phys.***1995** *34* 5188.

(148) Yasaka, T.; Takakura, M.; Sawara, K.; Uenaga, S.; Yasutaka, H.; Miyazaki, S.; Hirose, M. *IECE Trans. Electron.*, **1992** *E75-C (7)* 764.

(149) Yeo, K.L.; Wee, A.T.S.; See, A.; Liu, R.; Ng, C.M. *Appl. Surf. Sci.*, **2003** *335* 203.

(150) Zavadil, K.R.; Ingersoll, D.; Rogers, J.W. Jr., *J. Electroanal. Chem.*, **1991** *318* 223.

(151) Zhong, L.; Shimura, F. *Appl. Phys. Lett.* **1992** *61 (9)* 1078.

(152) Zoth, G.; Bergholz, W. *Electrochem. Soc. Symp. Proc*.; Electrochem. Soc.: Pennington, NJ 1991; p 643

(153) Zoth, G; Bergholz, W. *J. Appl. Phys.* **1990** *67* 6764.